ALMA MATER STUDIORUM
UNIVERSITÀ DI BOLOGNA

DEPARTMENT OF PHYSICS AND ASTRONOMY "A. RIGHI"

SECOND CYCLE DEGREE

PHYSICS

# Cosmic-Ray Upscattered Dark Matter and its Searches with IceCube


**Supervisor**
**Prof. Filippo Sala**

**Co-supervisor**
**Prof. Gwenhaël De Wasseige**

**Defended by**
**Allegra Cavicchi**



July 2025

Academic Year 2024/2025

*Se guardo il tuo cielo, opera delle tue dita,*
*la luna e le stelle che tu hai fissate,*
*che cosa è l'uomo perché te ne ricordi*
*e il figlio dell'uomo perché te ne curi?*

(Salmo 8, 4-5)

# Abstract

Since its theoretical proposal by Fritz Zwicky in 1933, to account for unseen mass in the Coma cluster of galaxies, dark matter and its gravitational effects have been discovered in several independent astrophysical and cosmological observations. In the past decades, significant progress has been made in both the experimental search and in the theoretical modelling of this new kind of matter.
No evidence of non-gravitational interactions of dark matter has been observed so far, despite they are motivated to reproduce its observed abundance in the universe. For this reason, the search for such interactions has rapidly become a growing field of research, and therefore numerous dedicated experiments have been developed.
In this thesis, we investigate the use of IceCube and, more generally, of neutrino detectors, as direct detectors of sub-GeV dark matter. The dark matter candidate considered in this work is hadrophilic light dark matter, a new particle that interacts with Standard Model hadrons. Under this assumption, a high-speed component of the galactic dark matter flux arises from its upscattering by cosmic rays, peaking in the GeV energy range. Neutrino telescopes such as IceCube are sensitive to these energies and can therefore be used to place constraints on the parameters of the model, such as the dark matter mass and its coupling to ordinary matter. While similar studies have been conducted with other neutrino experiments, such as Super-Kamiokande, this work represents the first analysis of this type performed with IceCube data.
Although this is a first investigation based on public data, we show that competitive results can already be achieved in the relevant parameter space. This confirms the potential of IceCube and other neutrino telescopes in probing sub-GeV dark matter and paves the way for more dedicated analyses in the future.

# Contents

# List of Figures

# List of Tables

# List of Acronyms

DM: Dark Matter
SM: Standard Model
BSM: Beyond Standard Model
CRs: Cosmic Rays
AMANDA: Antarctic Muon and Neutrino Detector Array
DOM: Digital Optical Module
DOM-MB: DOM Mainboard
PMT: PhotoMultiplier Tube
HLC: Hard Local Coincidence
SLC: Soft Local Coincidence
SMT: Simple Majority Trigger
CORSIKA: COsmic Rays SImulations for KAscade
GENIE: Generates Events for Neutrino Interaction Experiments
STW: Static Time Window
DTW: Dynamic Time Window
SRT: SeededRT algorithm
ELOWEN: Extremely LOW-Energy interactions
GRECO: GeV Reconstructed Events with Containment for Oscillations
C2QR6: Cleaned Charge Ratio in $600$ ns
SPE: Single PhotoElectron

# CHAPTER 1

# Motivations of this study

In the past decades, astrophysical and cosmological observations have established the existence of a new form of matter, different from ordinary matter, which is not luminous and is therefore known as ”dark matter”.
Planck satellite observations [1] have revealed that dark matter is around $27\%$ of the energy density of the Universe, and is five times denser than the normal baryonic matter that fills only about $5\%$. Combined with dark energy ($\sim 68\%$), these three are the major constituents of the Universe today.

This new form of matter, unforeseen by the Standard Model, is an evident indicator of the need for new physics. Dark matter adds to a list of compelling open questions such as the origin of neutrino masses, the baryon asymmetry of the Universe, and the strong CP problem, which signal that the Standard Model, although successful, is not complete ([2], [3]).

The existence of Dark Matter is known only from its gravitational effects, while all other potential interactions of this mysterious element of the universe are beyond our current knowledge. Thus, the study of DM non-gravitational impacts is a growing field of research, leading to numerous specialized experiments.
Amongst these experiments, the Direct Detection ones attempt to observe the DM scattering on a Standard Model particle, observed through the target recoil energy reconstruction.
Astrophysical and cosmological data tell us that the galactic component of DM is non-relativistic ($v \sim 10^{-3}$ within the Milky Way halo); therefore, sub-GeV DM produces nuclear recoil energies below $O$ (keV). Current DD experiments, which are sensitive to keV-scale recoil energies, become insensitive to sub-GeV DM masses very rapidly.
By constructing new experimental techniques, these experiments could become sensitive to these very low recoil energies; moreover, different approaches can be used, as the Dark Matter Direct Detection using Neutrino Telescopes, as presented in this thesis.

This study starts from a general assumption of the scattering between Standard Model and Dark Matter particles, as for all Direct Detection experiments. With this simple hypothesis and as first pointed out in Refs. [4] and [5], a higher-speed component of

the DM halo flux arises, because of the upscattering of galactic Dark Matter by Cosmic Rays, peaking in the GeV energy range. This upscattered light Dark Matter might induce observable recoils in huge-volume detectors, overcoming the current Direct Detection experiments' sensitivity loss.
Neutrino telescopes like Super-Kamiokande are sensitive to such energies and have already been used as Dark Matter detectors, setting world-leading limits, as described in Refs. [4] and [6]. Higher-energy telescopes like, for instance, IceCube are sensitive to such energies as well and are perhaps even more promising, given their larger volume.

My thesis attempts to understand how IceCube and, more broadly, large neutrino telescopes can be exploited for sub-GeV Dark Matter detection. This is a first attempt at using IceCube as a sub-GeV Dark Matter Direct Detector. Note that instead it has already been used for Indirect Searches, which aim to detect neutrinos that arise from annihilations of heavier Dark Matter, that take place outside the detector.

This thesis is organized as follows. Chapter 2 describes the main evidence we have nowadays regarding Dark Matter, the properties inferred from its gravitational interactions, and the state of experiments looking for its non-gravitational interactions with the Standard Model particles. Chapter 3 provides an introduction to neutrino telescopes, such as neutrino phenomenology in the detectors, and a description of the Cherenkov effect by which we observe the neutrino signature in the detector. Finally, in Chapter 4, I provide a short overview of IceCube, looking in particular at the leading background sources and two selection criteria used to discriminate between signal and background. Then, in Chapter 5, the model employed for this analysis is described: a light hadrophilic Dark Matter particle that interacts with Standard Matter via a scalar or pseudoscalar mediator. This chapter also presents the analysis technique, which is based on a minus-log-likelihood test statistic. Finally, Chapter 6 includes the key findings of this analysis, as well as some hints that can be useful for a future, and more precise, study.

# CHAPTER 2

# What do we know about Dark Matter?

Significant progress has been made in the dark matter searches over the past decades. Thanks to observations of gravitational DM-SM interactions, some dark matter properties have been understood. However, a large portion of the dark matter generalities remains unexplored, particularly regarding possible non-gravitational DM–SM interactions.

In this Chapter, I present the key aspects of what we currently know about dark matter. In Section 2.1, I introduce the observational evidence for the Dark Matter existence; in Section 2.2, I describe its main properties. Continuing with Section 2.3, the main Dark Matter density distributions are shown. Then, in Section 2.4, I present the most promising Dark Matter candidates, and in Section 2.5, some of the most famous production mechanisms of sub-GeV Dark Matter. Finally, in Section 2.6, an overview about laboratory searches of sub-GeV Dark Matter is introduced.

## 2.1 Evidence for Dark Matter

All the proofs for the DM existence derive from its gravitational effects. In contrast, no evidence based on some other DM effects, not due to gravitational interaction, has been discovered up to now [7]. These gravitational observations come from a wide range of astronomical scales, from the typical size of a small galaxy (a few kiloparsecs) to the size of the observable Universe [8].
In the following, I categorize the observations according to the length-scale, starting from spiral galaxies, continuing with galaxy clusters, and concluding with cosmological scales.

### 2.1.1 Evidences from the Galactic scale

Starting from the smallest scale considered, the galactic scale, the most notable observations that come from these distances are the rotation curves of both spiral and dwarf galaxies.

**Rotation curves of Spiral Galaxies**

The circular velocity profile of the stars and gas in a galaxy, so-called *galaxy's rotation curve*, as a function of their distance from the galactic center, played a particularly important role in the DM discovery. Under some reasonable simplifying assumptions, it is possible to infer the mass distribution of galaxies from their rotation curves [9]. Historically, it was the observation of approximately flat rotation curves at very large galactocentric distances that convinced the scientific community that large amounts of a new kind of matter, different from the ordinary one, is present in the outer regions of galaxies [7].
The studies on these rotation curves started in the XX century and rapidly developed until the 1960s, when Kent Ford and Vera Rubin observed the M31 rotation curve, the first ever observed [10].

These rotation curves can be derived using several methods. One approach involves observing the absorption lines in the optical spectra of stars, which shift, due to the Doppler effect, when the stars move relative to the observer; by measuring these shifts, the circular velocity of the stars can be determined [11]. Alternatively, emission lines from ionized hydrogen and neutral hydrogen can be used. Stellar spectroscopy mainly probes the inner regions of galaxies, ionized hydrogen traces the detailed kinematics of the disk, and neutral hydrogen observations allow the rotation to be mapped out to large radii, where the DM effects become evident [8].

According to Newton's law $F = ma$, the relation between the circular velocity $v_{\text{circ}}$ of a test particle of mass $m$ and the mass $\mathcal{M}$ contained within a distance $r$ from the center is

$$m\frac{v_{\text{circ}}^2(r)}{r} = \frac{Gm\mathcal{M}(r)}{r^2} \qquad \Rightarrow \qquad v_{\text{circ}}(r) = \sqrt{\frac{G\mathcal{M}(r)}{r}}\,. \tag{2.1}$$

In spiral galaxies, the most of the visible mass is concentrated in a dense central bulge and in the arms of the disk, which typically extend to $\mathcal{O}(10)$ kpcs; therefore, at large $r$, all the visible mass is contained within the orbit and $\mathcal{M}(r)$ can be replaced by a constant $\mathcal{M}$. This implies that the velocity should follow a Keplerian decline such that $v_{\text{circ}}(r) \propto r^{-1/2}$ [7].

However, from the observations of a large sample of this kind of galaxy, we have found that the rotation curves have a flat behaviour in $r$ out to large distances from the galactic center, as represented in Figure 2.1. This implies that, assuming the exactness of Newton's law, additional invisible mass must be present to keep the galaxies compact [12]. Withoit this additional amount of matter, galaxies would not be gravitationally bound and they would disintegrate.
To obtain the observed constant velocity $v_{\text{circ}}(r)$, a ***dark matter halo*** is assumed, with a mass density that should behave as $\rho_\chi(r) \propto 1/r^2$ at large $r$; in this way $\mathcal{M}(r) = 4\pi \int dr' r'^2 \rho_\chi(r') = 4\pi r$ and therefore, from Equation (2.1), the dependence of $v_{\text{circ}}$ on $r$ vanishes [8].

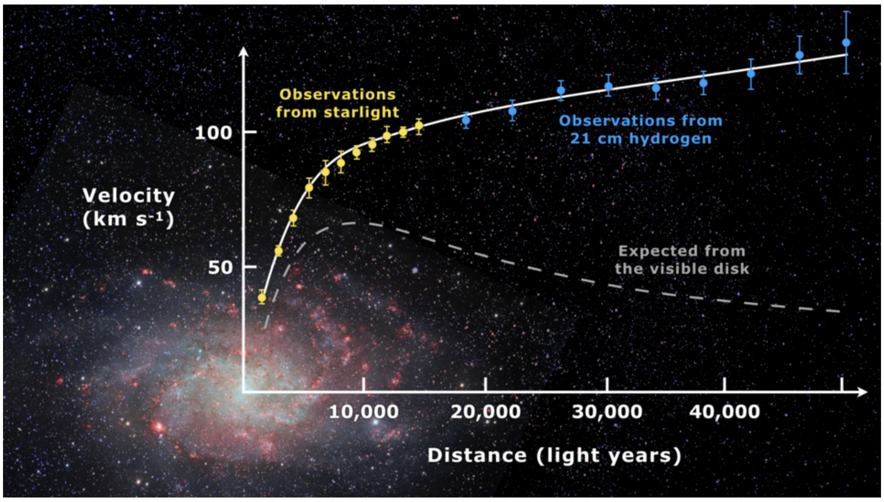


**Figure 2.1.** Rotation curve of spiral galaxy Messier 33 (yellow and blue points with error bars), and a predicted one from the distribution of the visible matter (gray line). Credits: Galaxy rotation curve.

#### Rotation curves of Dwarf Galaxies

The same kinematics measurement discussed for the spiral galaxies can also be applied to other kinds of galaxies, as the dwarf galaxies [13].
We know that the Milky Way (MW) is surrounded by satellite galaxies, systems tied to the main MW halo by gravitational attraction; among them, the large majority consists of dwarf spheroidal galaxies (dSph). The definition of the "dwarf" has not been universally accepted until now; in general, a dwarf galaxy has a DM-dominated mass of around $10^6 M_\odot$; the half-light radius $r_{\text{HL}}$, defined as the radius of the circle that contains half of the light emission from the galaxy, can be order of tents/hundreds of parsecs. Finally, the number of stars in a dwarf galaxy can be from a dozen to several thousand[14].
The experimental results show evidence for a larger content of DM in these systems with respect to spiral galaxies, with *mass-to-light* ratio $\mathcal{M}/\mathcal{L}$ of the order of 100 or more; this value is much greater than for spiral galaxies, where usually $\mathcal{M}/\mathcal{L} \sim 10$[8]. Furthermore, because dwarf galaxies contain only a few stars and are observed to be DM dominated, they are promising targets for DM searches, see e.g. Ref. [15].

### 2.1.2 Evidences from the Cluster of Galaxies scale

The clusters of galaxies are the largest gravitationally bound systems in the Universe; they contain hundreds to thousands of galaxies and extend to several Mpc in size [8]. Because of their size, they are good probes of the average Universe.
The DM presence in galaxy clusters is generally inferred by estimating its mass from their dynamics, governed by the gravitational effect of the system, and comparing it with the masses estimated from their luminosity [16].

At this length scale, the most notable DM evidences come from the internal dynamics of galaxy clusters and the gravitational lensing.

### Internal Dynamics of Galaxy Clusters

Fritz Zwicky was the first person to claim the DM evidence in 1933, by looking at the velocity dispersion in the ***Coma*** cluster of galaxies [17].
His intuition was based on the *virial theorem*, which enables us to estimate the dynamical mass of a galaxy cluster.

The ***viral theorem*** relates the time-averaged kinetic energy to the time-averaged potential energy $< K >= -\frac{1}{2} < V >$ of a bound system of interacting nonrelativistic particles in dynamical equilibrium [18].
In a toy system with $N \gg 1$ objects of mass $m$ at equal distance $r$ interacting through gravity, this theorem allows us to determine their total mass $mN$ from the velocity $v$ of the system and its size $R$:

$$N\frac{mv^2}{2} = \frac{1}{2}\frac{N^2}{2}\frac{Gm^2}{R} \qquad \Rightarrow \qquad mN = \frac{2Rv^2}{G}. \tag{2.2}$$

Measuring the motion of some galaxies in the Coma cluster, Zwicky estimated its gravitational mass, considering a regular shape of the cluster and the galaxies in it of the same mass. With the known luminosity from visible light of the cluster, the mass-to-luminosity ratio for the Coma cluster was computed to be of the order of 50 times larger than that of an individual galaxy [17].

Three years after this observation, Sinclair Smith achieved similar observations for the ***Virgo*** cluster, which contains more elliptical galaxies, resulting in an irregular shape and therefore in a more complicated object to study. The estimations of gravitational mass and luminosity of the Virgo cluster also confirm the presence of invisible DM in this cluster [19].

### Gravitational Lensing on Cluster Scales

Gravitational Lensing is a phenomenon in which light bends while passing through the vicinity of a gravitating mass gives rise to the lensing effect, a phenomenon known as gravitational lensing. This is a direct consequence of Einstein's general theory of relativity; light follows a curved space in the proximity of a gravitating body, giving rise to this effect [20]. The observance of such lensing effects, without an apparent detection of luminous mass that can cause it, could indicate therefore the presence of unseen matter.
The gravitational lensing effect can be characterized into three categories: *strong lensing*, where multiple images or Einstein's rings are produced for a distant object in the background, *weak lensing*, which causes distorted or deshaped images of a background object, and *microlensing*, where the brightness of the object in the background of the gravitational mass appears to have increased to the observer in the foreground[18].

Today, one of the strongest evidences for the presence of DM on the length scales of galaxy clusters comes from the observations of a pair of colliding clusters known as the ***bullet cluster*** (catalog name: 1E0657-56), first observed in 2006 [21].

This cluster has been created as a result of one of the most energetic events to have happened in our Universe after the Big Bang, by which two giant galaxy clusters collided at a distance of around 4 billion light years from the Earth. Most of the baryonic mass in the cluster is in the form of hot gas, whose distribution can be traced through its X-ray emission, while the distribution of the total mass, visible and dark, was independently measured through weak lensing [18].
The special feature of the bullet cluster system is that the visible matter and DM are spatially separated, as reported in Figure 2.2. This has been interpreted as a signature that, in the past, the two clusters were separated systems that then collided 150 million years ago. The analysis shows that, as a result of this collision, the smaller cluster passed through the core of the larger. Furthermore, visible matter interacts significantly with itself, while DM experiences negligible interactions with itself and with normal matter: the impact was so great that it caused the baryonic matter in each colliding cluster to displace from its respective DM halo, while the DM halos themselves passed through each other rather unperturbed and undistorted ([8],[18],[21],[22]).
This behavior is not unique to the Bullet Cluster: other observations of colliding galaxy clusters also support this picture, showing consistent separations between the baryonic and gravitational mass components [23].

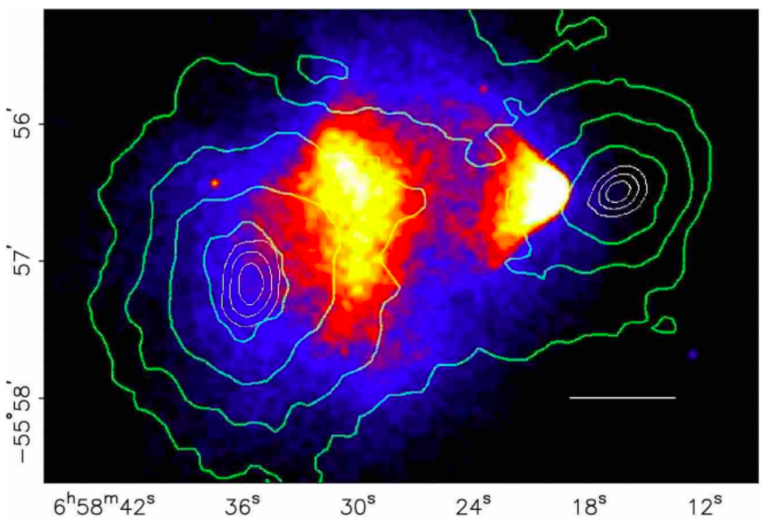


**Figure 2.2.** The distribution of baryonic mass is traced by the X-ray emission (color-coded from blue to red, in increasing order of intensity, which corresponds to the density of the hot plasma), while the green contours represent the total mass distribution reconstructed through weak gravitational lensing. Credits: [22].

Thus, the phenomenon of the bullet cluster not only gives observational evidence of the DM existence, but also indicates that DM is almost collisionless.

### 2.1.3 Evidences from the Cosmological scales

Finally, other convincing and precise evidence for DM existence comes from the entire observable Universe, the largest scales possible. This is simply given by the fact that the Universe would not appear as it is today if DM have not played any role[8].

In the following paragraphs, the most notable evidences for this scale are addressed, starting from the large scale structure formation, and concluding with the observation of Cosmic Microwave Background acoustic peaks.

### 2.1.4 Large Scale Structure Formation

Today, the Universe is highly inhomogeneous on scales smaller than its current horizon. In the standard cosmological model, these primordial inhomogeneities are generated by inflation and have small amplitudes ($\delta \sim 10^{-5}$) [8].
These small fluctuations would not have had enough time to grow into the large-scale structures we observe today, as galaxies and clusters, without an additional mechanism. Assuming that DM does not interact with radiation, it starts to collapse under gravity earlier than ordinary matter. This early collapse initiated the formation of cosmic structures. DM is therefore essential to explain how such large structures could have formed from initially tiny perturbations [24].
To study this process in more detail, N-body simulations are employed. These simulate the gravitational evolution of a large number $N$ of massive particles in an expanding Universe, starting from typical realizations of the primordial inhomogeneities. The inclusion of DM is crucial, as it dominates the matter content of the Universe and drives the growth of cosmic structures through its early gravitational collapse [25].

#### Cosmic Microwave Background Acoustic Peaks

Looking at the Cosmic Microwave Background (CMB) power spectrum, obtained from the coefficients, at different multiples $l$, of the expansion in spherical harmonics of the temperature fluctuations between points on the skymap at different angluar separations, the signature of DM presence is evident. More specifically, a phase shift in the CMB acoustic oscillations spectra is found, which is a characteristic signature for the presence of non-photon radiation propagating differently from photons, even when the radiation couples to the SM particles solely gravitationally [26]. An example of these spectra is shown in Figure 2.3.

The CMB peaks are due to acoustic oscillations of the baryon/photon fluid; their positions depend on the DM density, while their amplitude depends on the relative amount of DM with respect to ordinary matter [8]. From global fits it is clear that, without DM, the observed structure of the CMB spectrum cannot be accurately reproduced [26]. This provides the most accurate measurement of the DM density currently available. This density is expressed as $\Omega$, which is the ratio between the energy density of a given component and the critical density. In particular, $\Omega_{\mathrm{DM}}$ represents the fraction of the Universe's energy density made up of DM [27]:

$$\Omega_{\mathrm{DM}} h^2 = 0.1200 \pm 0.0012 \qquad \Rightarrow \qquad \Omega_{\mathrm{DM}} \sim 0.265. \tag{2.3}$$

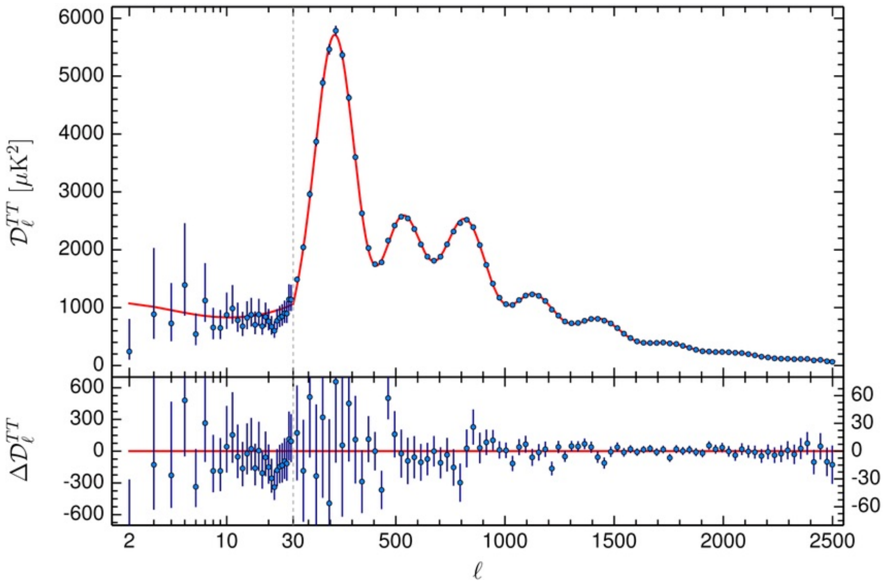


**Figure 2.3.** The angular Power spectrum of the CMB as a function of the angular scale measured by Planck 2015 with the residual errors. The solid line represents the theoretical prediction for the $\Lambda CDM$ model and the dots the observed data. Credits: [1].

## 2.2 Dark Matter Properties

The observational evidence discussed in the previous section can be consistently interpreted by postulating the DM existence with a set of basic properties.
This is particularly compelling, as DM currently represents the only framework capable of simultaneously explaining such a wide range of astrophysical and cosmological phenomena [28]. In the following, some of the DM properties that we can infer from these observations are presented:

- ***matter***: the term ”matter” refers to the fact that DM contributes to the energy density of the Universe in the same way as non-relativistic matter, with an energy density that scales inversely with the volume in the cosmological evolution[8];

- ***DM and SM interactions***: DM must be gravitational interacting, because all observational evidences discussed in Section 2.1 rely on its gravitational interactions, but since DM is not luminous in galaxies or clusters we expect that is not electromagnetically interacting. Additionally, we expect that DM interactions with SM particles are much weaker than known SM interactions [28].

- ***cold (non-relativistic)***: DM behaves as a non-relativistic fluid at the time of matter-radiation equality, when structure formation begins (if it were relativistic, clustering would not be effective and structures would not form) [8]. In addition, DM particles should travel through the Solar System and traverse the Earth with typical galactic velocities of $\sim 200$km/s $\Rightarrow v \sim 10^{-3}c$ [29];

- ***collision-less***: DM is expected to have negligible non-gravitational self-interactions. Observations of colliding galaxy clusters, such as the Bullet Cluster, show that the gravitational lensing signal is clearly separated from the hot baryonic gas. If DM had strong self-interactions, the lensing map would instead trace the baryonic matter more closely. This behavior suggests that dark matter passes through both itself and ordinary matter without significant scattering, placing strong constraints on the strength of any possible self-interactions[28];

- ***collision-less***: Dark matter is expected to have negligible non-gravitational self-interactions. Observations of colliding galaxy clusters, such as the Bullet Cluster, show that the gravitational lensing signal is clearly separated from the hot baryonic gas. If dark matter had strong self-interactions, the lensing map would instead trace the baryonic matter more closely. This behavior suggests that dark matter passes through both itself and ordinary matter without significant scattering, placing strong constraints on the strength of any possible self-interactions [28];

- ***stable (or with a very long lifetime)***: we know that DM is present since the early Universe and has not disappeared until now, therefore the lifetime of DM should be much greater than the age of the universe ([28], [8]);

- finally, it must preserve the successes from ***Big Bang Nucleosynthesis*** [18].

## 2.3 Dark Matter Distributions in the Galaxy

Even if the average DM density in the Universe is tiny, as shown in Equation (2.3), there is much more DM than just this average value clumped in structures much smaller than the entire universe, like galaxies. Because of structure formation, the distribution of DM in specific systems differs significantly from the average cosmological value. To interpret the results of Direct and Indirect DM detection searches, we have to introduce the DM density distribution $\rho_\chi(r)$ in the Milky Way ([8], [30], [31]).
First of all, we know that DM tends to be roughly spherically distributed in gravitationally bound systems, hence the density distribution $\rho_\chi(r)$ is expressed as a function of the radial coordinate $r$ measured from the Galactic Center; secondly, we known that DM is non-relativistic in most systems of interest. Furthermore, DM particles bound to our galaxy must have a velocity below the escape velocity, $v_{\text{esc}} \sim 500$ km/s[32].

Among several candidates, some of the most famous and experimentally supported galactic DM density profiles are:

- ***Navarro-Frenk-White (NFW) profile***: this is the most commong choice, motivated by the N-body simulations [33]. This profile is described by the following analytical formula:

$$\rho_{\rm NFW}(r) = \rho_\odot \cdot \frac{r_\odot (r_\odot + r_c)^2}{r(r + r_c)^2} \tag{2.4}$$

  where $\rho_\odot = 0.42 \pm 0.06$ GeV/cm$^3$ is the DM density at the sun position, $r_\odot = 8.5$ kpc and $r_c = 20$ kpc ([34], [6]);

- ***Einasto profile***: this profile seems to be a better fit to more recent numerical simulations. It is very similar to the NFW one, even if is a little bit less peaked [35]. It is described by the following analytical formula:

$$\rho_{\text{Einasto}}(r) = \rho_{-2} \exp\left\{-\frac{2}{\alpha_E}\left[\left(\frac{r}{r_{-2}}\right)^{\alpha_E} - 1\right]\right\} \tag{2.5}$$

  where $\rho_{-2} = \rho(r_{-2})$ is the density at which the slope parameter is -2 and $\alpha_E$ is a parameter to control the profile's curvature;

- ***Isothermal profile***: it features a constant central density, therefore, differently from the previous ones, has not a peak in the galactic center but a flat behavior [36]. This profile is described by the following analytical formula:

$$\rho_{\text{Iso}}(r) = \frac{\rho_0}{1 + \left(\frac{r}{r_c}\right)^2} \tag{2.6}$$

  where $\rho_0$ is the central density and $r_c$ is the core's radius;

- ***Burkert profile***: as the isothermal profile, has a constant central density, which is a little bit smaller than the isothermal one. This profile is given by a modification of the isothermal one:

$$\rho_{\text{Burkert}}(r) = \frac{\rho_0}{\left(1 + \frac{r}{r_c}\right)\left[1 + \left(\frac{r}{r_c}\right)^2\right]} \,. \tag{2.7}$$

All these DM profiles are shown in Figure 2.4.

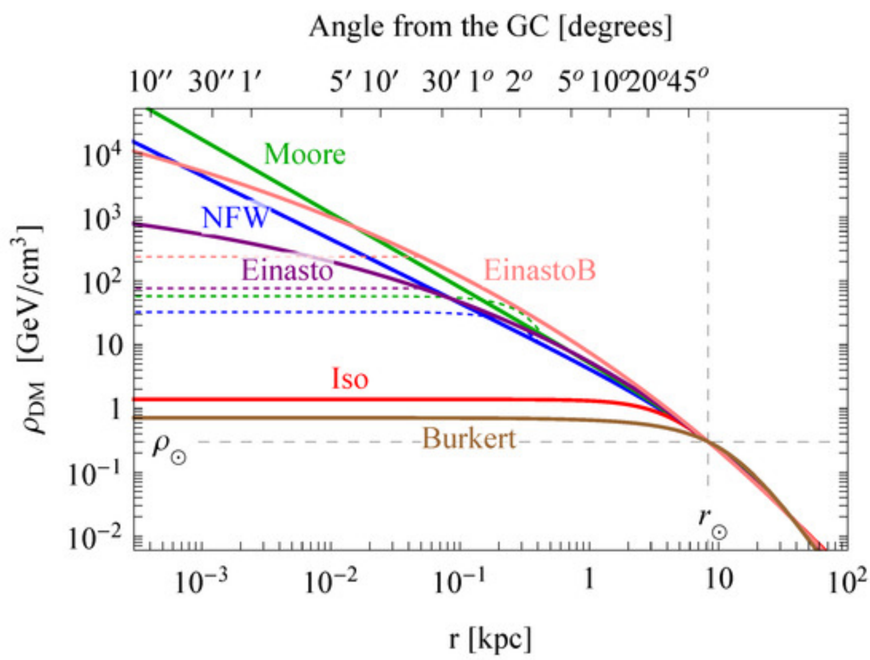


**Figure 2.4.** Commonly used Milky Way DM density profiles. Credits:[37].

## 2.4 Dark Matter Candidates

From the first evidence of DM existence, a lot of candidates have been proposed as possible DM particles. Empirically, requiring that the De Broglie wavelength of a DM particle fits within the dwarf galaxies, we know that these particles must be heavier than $10^{-21}$ eV [38]; regarding the upper limit, DM can be heavier than the Planck mass, if it takes the form of a composite object. In this case, the limit is obtained by the fact that the DM must be smaller than a small dwarf galaxy (which has a mass of the order of $10^5 M_\odot$) [8]. Therefore, the model-independent bounds on the DM mass are

$$\boxed{10^{-21}\text{eV} < M_\chi < 10^5 M_\odot} \tag{2.8}$$

where $M_\odot = 1.989 \times 10^{30}$ kg. This range of DM masses spans more than $90$ orders of magnitude, giving us the possibility to focus on several DM candidates.

In the following, the most well-known DM candidates are briefly introduced; a summary of their properties[1] is presented in Table 2.1.

**Primordial Black Holes (PBH)**
Among all the following DM candidates, Primordial Black holes are the only which are astrophysical objects and not particles. They are black holes formed from overdensities in the early Universe; the discovery of gravitational waves from mergers of tens of Solar mass black hole binaries by LIGO-Virgo has generated an increasing interest in PBH dark matter [39]. They fulfill all of the requirements to be a good DM candidate, since they are cold, stable, and can be formed in the right abundance to be the DM. As they form before nucleosynthesis, PBHs are non-baryonic and therefore they are non-baryonic DM candidates [40].

**Super-heavy Dark Matter (WIMPzillas)**
The Universe might also be made of superheavy *Weakly Interacting Massive Particles*, with mass larger than the weak scale. The conditions needed are that the particles must be cosmologically stable and that their interaction rate must be sufficiently weak such that thermal equilibrium with the primordial plasma was never obtained [41] or, if they were at equilibrium, some entropy injection should have taken place to avoid that they overclose the universe. Super- heavy DM may be created during the evolution of the Universe in several ways, an example is non-thermal processes, like freeze-in just after inflation [42].

**Weakly Interacting Massive Particles (WIMPs)**
Weakly-interacting massive particles (WIMPs) have been leading DM candidates for decades, and they remain a viable and highly motivated possibility.
Even if there is no precise definition of it, we refer to WIMPs as particles that interact through the SM weak interactions; therefore, they need to be charged under the electro-weak $SU(2)_L \times U(1)_Y$ group, have zero electromagnetic charge, be a color

[1]Regarding the interactions, we present here the ones other than gravity.

singlet, and be stable. More broadly, the term WIMP is used to denote a stable particle that couples to other weak-scale particles and interacts with a strength equal to or weaker than the SM one [43].
Since they arise from simple SM generalizations, they are among the most studied DM candidates; furthermore, they arise naturally in many particle physics theories, have the correct cosmological properties, and have an astonishing set of implications for observable phenomena. Finally, if WIMPs exist and are stable, they are naturally produced with a relic density consistent with the DM one [44].

**Sterile Neutrinos**
Sterile neutrinos with a mass in the keV range can play the role of DM. Indeed, these particles are neutral, massive, and, while unstable, can have their lifetime longer than the age of the Universe [45]. Such sterile neutrinos are produced in the early Universe at high temperatures; unlike other cosmic relic particles, as photons, neutrinos, or WIMPs, the feeble interaction strength of sterile neutrinos means that they were never in thermal equilibrium in the early Universe, and that their exact production mechanism is model-dependent [46].
Consequently, the viability of sterile neutrinos as DM candidates strongly depends on their production scenario and is subject to constraints from cosmological and astrophysical observations.

**Light Dark Matter**
This class of DM candidates is composed of sub-GeV particles. This mass range has traditionally received less attention because of the Lee-Weinberg bound, which states that, for sub-GeV DM particles, the known SM interactions are insufficient to reproduce the observed DM relic abundance through thermal freeze-out [47]. However, this limit is not valid anymore if we consider DM annihilations mediated by new interactions, or if DM is produced by non-standard cosmological mechanisms, like those that we present in Section 2.5. This makes sub-GeV DM an interesting DM candidate[48].

**Axion-Like-Particles (ALPs)**
Axion-like particles (ALPs) are a generic class of pseudoscalar bosons postulated in 1977 by Roberto Peccei and Helen Quinn to explain why the CP violation in strong interactions is very small; they are also predicted in many SM extensions, especially in string-inspired frameworks [49]. Depending on their mass and coupling, ALPs can play various roles in cosmology, including as DM candidates.
They can account for the observed DM abundance through mechanisms like vacuum misalignment; they typically span a wide mass range from about $10^{-28}$ eV (ultralight ALPs) to the eV scale, depending on their production and interaction scenarios [50]. However, masses below $10^{-21}$ eV are strongly constrained by structure formation, as they would suppress small-scale cosmic structures in conflict with observations [38].

**Fuzzy Dark Matter**
Another interesting DM candidate, alternative to cold DM, is Fuzzy Dark Matter (FDM); it is made of ultra-light bosons with masses at the order $m \sim 10^{-22}\,\mathrm{eV}$; such a candidate has the potential to avoid phenomenological problems of cold DM [51]. As

previously mentioned, observational bounds typically push the viable mass range to $m_\chi \geq 10^{-21}$ eV [38].
Due to their extremely small mass, such particles exhibit macroscopic quantum behavior at astrophysical scales, with de Broglie wavelengths of orders of kpc [52]. FDM is often explored in the domain of axion-like particles which arise in string-inspired frameworks, and is probed by a variety of astrophysical and cosmological tests from Lyman-$\alpha$ forests[2], galactic centers, and halo substructures [53].

| **Candidate** | **Typical Mass** | **Interaction(s)** |
|---|---|---|
| Primordial Black Holes (PBH) | $10^{-16}M_\odot \lesssim M_\chi \lesssim 3\times10^{-12}M_\odot$ | None |
| Super-heavy DM | $M_\chi \gtrsim 10^5\mathrm{GeV}$ | New forces |
| WIMP | $10\mathrm{GeV} \lesssim M_\chi \lesssim 10\mathrm{TeV}$ | Weak and/or new forces |
| Sterile Neutrino | $\mathrm{keV} \lesssim M_\chi \lesssim \mathrm{GeV}$ | Weak and/or new forces |
| Light Dark Matter (sub-GeV) | $\mathrm{MeV} \lesssim M_\chi \lesssim \mathrm{GeV}$ | New forces |
| Axion / ALP | $10^{-28}\mathrm{eV} \lesssim M_\chi \lesssim \mathrm{eV}$ | New forces |
| Fuzzy DM | $M_\chi \sim 10^{-22}$ eV | New forces |

**Table 2.1.** Dark matter candidates ordered by decreasing mass per object. Regarding the interactions, we present here the ones other than gravity.

## 2.5 Sub-GeV Dark Matter: production mechanisms

Among all possible DM candidates, this study focuses on DM particles with masses below the GeV scale. This candidate has traditionally received less attention than others because of the Lee-Weinberg bound.
This bound is a lower limit on the DM mass, originally derived in the context of thermal freeze-out for fermionic particles that interact weakly with the Standard Model. In 1977, Benjamin W. Lee and Steven Weinberg showed that if DM consists of particles interacting via the weak force (such as WIMPs), then their mass cannot be too low; otherwise, the annihilation would be inefficient, leading to an excessively large relic density that would overclose the Universe [54].

In recent years, however, many new DM models have been developed; these new models, in addition to the DM particle, feature a new interaction, mediated for instance by the gauge boson of a new $U(1)'$ gauge group. At the same time, while standard Direct Detection experiments quickly lose their sensitivity to sub-GeV DM because of the low nuclear recoils that it induces, several new ideas have arisen in

[2] Lyman-$\alpha$ forest observations trace the small-scale distribution of matter at high redshift and can constrain deviations from the standard cold DM scenario.

the past 15 years to overcome this limitation, see Section 2.6.2 for more details. In addition, accelerator experiments have performed various dedicated searches on new mediators' signals in visible and invisible final states. In combination, these developments make sub-GeV DM a particularly fascinating field of investigation [48].
Furthermore, as presented in the following, other DM production mechanisms can be considered, overcoming the Lee-Weinberg bound.

### 2.5.1 Dark Matter as a thermal relic: Freeze-Out mechanism

The freeze-out mechanism assumes that DM is a stable particle that, in the early Universe, had interactions with the SM particles that were faster than the Hubble rate, hence it interacted with Standard Model particles more often than the Universe was expanding. As a result, DM was in thermal equilibrium with the rest of the plasma, sharing the same temperature.
If there is no conserved DM number, any initial differences between the SM and DM components (for example, caused by inflation) are erased during this thermal phase. The entire Universe is then filled with a single, mixed fluid of SM and DM [55].
As long as the particles are in interaction with the plasma with a common temperature, particles are in thermal equilibrium, and the distributions are driven only by the temperature. However, since the Universe is expanding, the temperature decreases and the average distance between particles in the plasma increases, which limits the interaction rate. The equilibrium can therefore be broken, the unstable particles decay, and the stable ones undergo a "freeze-out". Since the stable particles do not decay and the interactions are heavily suppressed, their number is frozen and nearly constant [56].

Because the SM and DM sectors were in thermal contact early on, the freeze-out process naturally explains why both share the same adiabatic structure of inhomogeneities, in agreement with cosmological observations.
This means that fluctuations in the densities of dark matter and ordinary matter are correlated and evolve together, preserving a common pattern throughout cosmic history [8].

In addition, freeze-out from thermal equilibrium is a generic mechanism applicable to any interacting massive particle. In its simplest form, it predicts the DM relic abundance primarily based on the annihilation cross-section, with only a weak dependence on the DM mass. This remarkable feature has made freeze-out one of the most extensively studied scenarios in DM research, although, as will be discussed later, there exist alternative models that are less predictive but equally captivating [55].

Regarding sub-GeV DM candidates, one possibility is that thermal freeze-out proceeds with a suppressed annihilation cross-section (e.g., via small couplings or light mediators), allowing for lighter DM masses than the electroweak scale. In such cases, efficient annihilation into light SM states is required to avoid overproduction [57].

### 2.5.2 Dark Matter as a non-thermal relic: Freeze-In mechanism

Another simple mechanism to produce the DM relic density is the freeze-in mechanism. In this model, DM particles have a very weak coupling to SM particles, and are therefore initially decoupled from the primordial thermal bath. DM particles could have been produced in small quantities by the decay of primordial particles, since, even if the interactions with the bath are weak, they still lead to DM production and gradually increase its density. This process continues until the temperature of the plasma becomes too low for further DM production [58].

Unlike freeze-out, which does not require an initial condition for the DM abundance (as it is assumed to be thermalized), freeze-in scenarios require a detailed description of it. Therefore, freeze-in scenarios are predictive only when they derive from a high-energy theory that can determine the initial DM density.
Differently from the usual freeze-out scenario, the relic density may also receive a contribution from a primordial component, which is not erased by any process since DM creation occurs out of thermal equilibrium [8].

Regarding sub-GeV DM candidates, freeze-in is particularly well-suited to produce such kind of particles, since the production rate depends on very feeble interactions that never thermalize. As a result, the DM mass is not constrained to be heavy, and many viable freeze-in scenarios exist in the sub-GeV regime [59].

### 2.5.3 Asymmetric Dark Matter

Finally, asymmetric Dark Matter is an interesting alternative to the traditional freeze-out scenario. This model considers the DM relic abundance as originating from a primordial particle–antiparticle asymmetry, analogous to the baryon asymmetry observed in the visible sector. In this framework, the present DM density results from a small initial DM excess of particles over antiparticles in the early Universe: while the symmetric component annihilates away, the asymmetric excess survives and constitutes the relic abundance. This mechanism permits larger annihilation cross-sections than those required in freeze-out models and requires the DM particle to be extremely long-lived [48]. One of the most compelling features of asymmetric DM is its ability to naturally explain the observed similarity between DM and baryonic energy densities, $\Omega_\chi \sim 5\Omega_b$ [8].

Experimentally, this DM candidate is difficult to probe, as the lack of residual annihilations suppresses Indirect Detection signals. Direct Detection remains possible but strongly depends on the assumed DM–SM couplings, often requiring highly sensitive, low-threshold detectors and detailed theoretical modeling [60].

Regarding sub-GeV DM candidates, asymmetric DM models provide a natural framework, especially when the dark matter asymmetry is related to the baryon asymmetry. In scenarios where the two sectors communicate through higher-dimensional operators, sub-GeV masses are possible and even favored to reproduce the observed relic density [48].

## 2.6 Sub-GeV Dark Matter: Laboratory Searches

In this Section, after an introduction to the general strategies to look for non-gravitational DM signatures, we focus on laboratory searches.
For sub-GeV DM, the usual Direct Detection strategies have a much poorer sensitivity than for weak scale DM, since the momentum transfer is too small. On the other side, accelerator searches, particularly those involving high-intensity beams and sensitive measurements, represent a robust and complementary avenue. These experiments aim to discover signs such as a deficit of energy or momentum, or an unusual decay mode, that would suggest the presence of light DM particles [61].

### 2.6.1 Overview of Dark Matter Detection Methods

Currently, the existence of DM is based on observations that only probe its gravitational coupling with SM; these observations give us information about the total mass of DM in the Universe, as well as its density and speed distribution in some regions of the universe [56]. However, to understand deeply the DM nature, we also need to observe its other interactions with ordinary matter. We may employ three main avenues of investigation to detect DM particles and investigate their mass and interaction strength.
These methods are traditionally schematized as in Figure 2.5.

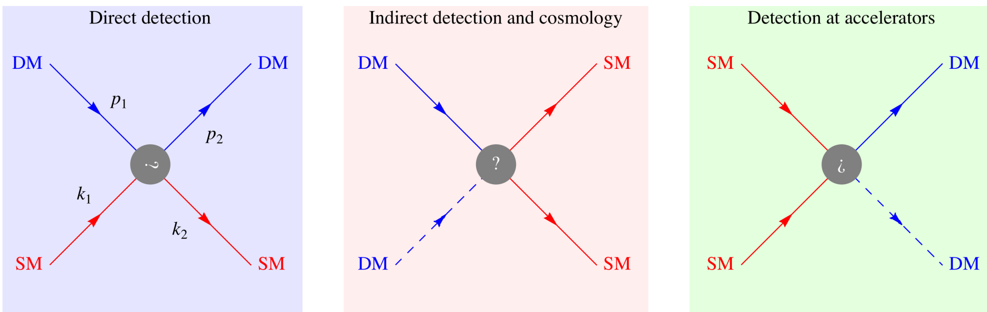


**Figure 2.5.** Three main DM search strategies, from left to right: direct detection, indirect detection (one of the DM lines is dashed, indicating that both DM decays and DM annihilation are relevant), and accelerator-based detection. Credits: [8]

#### Dark Matter Direct Detection

Dark Matter may be detected by its scattering off ordinary matter through processes $\chi\mathrm{SM} \to \chi\mathrm{SM}$. This detection method aims at detecting the recoil event produced by a passing DM particle hitting one of the nuclei or electrons in the detector. The field is extremely active, and can test different kinds of DM interactions. Two leading benchmarks are those where scatterings happen through spin-independent couplings or spin-dependent couplings, as presented in Chapter 5.
The main experimental challenges of this method are that the DM scattering rates are very low (can be below one event per ton of target material per year) and that the deposited energies are small, typically of the order of $\mathcal{O}$(keV) or $\mathcal{O}$(eV). Usually, to reduce the backgrounds, these experiments are situated deep underground and the detectors are made of ultra-pure materials [8].

Only to cite an example, for a typical DM mass of $m_\chi \sim 100$ GeV and a DM velocity $v_\chi \sim 10^{-3}$, the deposited recoil energy is at most $\sim 100$ keV: the detection of such low energy requires highly sensitive, low background detectors. Furthermore, such detectors are insensitive to very strongly interacting DM, which would be stopped in the atmosphere or Earth and would be undetectable underground [29].

**Dark Matter Indirect Detection**
This second detection method searches for DM-pair annihilation or decay, which results in SM particles that can be detected.
After freeze-out, DM pair annihilation becomes greatly suppressed, but it continues, with a negligible impact on DM relic density, and may be observable. DM may therefore be detected indirectly: if DM annihilates or decays somewhere, it can produce something that we can observe [29]. Therefore, this detection method aims to detect DM annihilations or decays in our Galaxy or other astrophysical environments by searching for signatures in cosmic rays.

**Dark Matter Laboratory-based Detection**
Finally, Laboratory-based methods aim at producing DM particles in a controlled environment, and then detecting the DM presence. For instance, colliders may have already produced DM particles, but this is not enough for a discovery. Indeed, once produced, the DM particle must also be detected. This is not completely straightforward [62], as we clarify below. Given that, realistically, DM must be a stable neutral particle, it cannot be singly produced at colliders but rather only in pairs such as $\chi\bar{\chi}$ or $\chi\chi$, possibly together with other SM particles; the collider energy, therefore, needs to be at least $\sqrt{s} > 2m_\chi$, where $m_\chi$ is the DM mass [63].
Consequently, once produced, DM particles result in a *missing transverse energy* signal $\not{E}_T$, as neutrinos do. Hence, $\not{E}_T$ is the DM signature that can be considered at colliders, since if DM interacts with SM particles, it interacts very feebly and therefore can escape the detector, carrying with it energy and momentum. Such a minimal signal of DM is detectable only if some other visible particle is also produced during the collision, otherwise, the event goes unnoticed. This is why the DM signal at colliders is an indirect and rather difficult signature, and our understanding of the backgrounds can limit its detection [64].

### 2.6.2 sub-GeV Dark Matter Searches at Direct Detectors

Traditional DM Direct Detection experiments, such as XENONnT, LUX-ZEPLIN, and PandaX, have been optimized for DM masses greater than 1 GeV [6]. This is a straightforward kinematic consequence, as these detectors rely on DM–nucleon elastic scattering: in such interactions, a fraction of the DM particle's kinetic energy is transferred to the nucleon. However, if the dark matter particle is light, as in the case of sub-GeV candidates, the transferred energy is very small, typically below 1 keV, and thus below the detection threshold of these experiments, which is often at the keV scale. As a result, for $m_\chi < 1$ GeV, these detectors completely lose sensitivity[65].

To access this parameter space, new low-threshold detection technologies have been developed. Since the loss of sensitivity is driven by the energy threshold, one solution is to reduce this threshold as much as possible. This has led to the emergence of a new class of experiments employing advanced technologies to explore this challenging regime. Among them are SENSEI, with a threshold of approximately 1.1 eV [66], and DAMIC-M, targeting thresholds of a few eV [67], enabling sensitivity to very small ionization signals. Similarly, CRESST-III has achieved nuclear recoil thresholds as low as 30.1 eV [68], while other experiments based on DM–electron elastic scattering, such as NEWS-G, aim to probe masses down to approximately 1 GeV [69]. The results of these experiments complement those from large neutrino detectors and collider searches, collectively contributing to a systematic exploration of the low-mass DM frontier.

### 2.6.3 sub-GeV Dark Matter Searches at Indirect Detectors

The sensitivity of DM detection through Indirect Detection methods, as presented briefly in the following, depends on the symmetry and velocity dependence of the DM-SM cross-sections. This implies that the strength of the indirect detection signal is strongly related to whether DM is asymmetric or symmetric, and whether it annihilates via s-wave or p-wave processes.

For the symmetric DM candidate, the annihilation rate is given by the thermally averaged cross-section $\langle \sigma_\chi \rangle$. If DM annihilates via an s-wave process, then the cross-section is approximately constant with velocity ($\langle \sigma \chi \rangle \sim$ const). Thus, annihilations remain efficient not only at thermal freeze-out, but at subsequent times and even today, when DM particles are non-relativistic. These residual annihilations inject energy into the early plasma, imprinting signatures in the anisotropies of the CMB. Consequently, s-wave annihilation scenarios are closely bound by CMB data, in particular by the Planck satellite [1], and by indirect detection of annihilation products in the astrophysical setting.

In contrast, when the most significant annihilation channel is p-wave, the cross-section is suppressed at low velocities, with behavior $\langle \sigma_\chi \rangle \propto v^2$. While annihilation remains effective at freeze-out (when velocities were comparatively large), the rate reduces sharply at subsequent times. This makes annihilations in the present Universe negligible, resulting in an extremely weak or unobservable indirect signal. Symmetric DM models dominated by p-waves are therefore much less constrained by current CMB observations and indirect detection experiments [70].

In asymmetric DM models, the abundance of relics is fixed by a primordial particle-antiparticle asymmetry. After freeze-out, nearly all antiparticles annihilate away and only the particle excess remains. As a result, annihilation is effectively cut off, and indirect detection signal is not expected [60].

In addition to annihilation, indirect detection experiments can also probe DM through its decay. If the DM has a cosmological timescale instability, its decay products, as photons, neutrinos, or charged particles, are accessible today [8]. In contrast to annihilation, which scales with the DM density squared, decay signals increase linearly with density, making them very attractive in diffuse settings like galaxy clusters or the cosmic background. The predicted signal is velocity-independent for the DM and indirect detection limits on decaying DM typically imply constraints on the lifetime of the DM, which must be greater than the age of the Universe by several orders of magnitude [71]. Decay is particularly significant in the case of asymmetric DM, where annihilation is not present but decay can produce observable signatures if there is a small soft breaking of the stabilizing symmetry [60].

### 2.6.4 sub-GeV Dark Matter Searches at Colliders

Dark matter searches at colliders are highly promising, as they could potentially allow for the production, and thus the detection, of DM particles in a controlled environment. Depending on the specific models considered, a wide range of possible signatures may arise at colliders. In general, the typical DM signal is missing transverse energy (MET): although DM may be produced in the collision, due to its extremely low interaction cross-section it escapes the detector without interacting, leaving behind only a missing energy signature, similar to that of neutrinos ([63], [72]).

In the following, I present two of the most interesting channels for DM searches at colliders, which also provide some of the most stringent constraints to date.

#### Monojet signatures at Colliders

Among the DM collider searches, the monojet channel is one of the most promising and well-known. As introduced before, DM could have already been produced at colliders, even if we have not observed it yet. Since the production of $\chi\bar{\chi}$ pairs is invisible, the best signatures are mono-jet signals from $\chi\bar{\chi}j$ production, where the jet comes from initial state radiation. In addition, other channels can be studied, such as the monophoton channel, the dijet channel, the DM pair production in association with the EW gauge bosons and also more complex signatures, which are usually model-dependent[72].

The monojet channel aims to investigate processes such as $pp \rightarrow \chi\bar{\chi}j$, which should be a common event at hadron colliders if DM interacts with hadrons. The experimental signature of this event is a large missing energy, given by the DM pair which is escaping the detector, and a jet. With *jet*, we refer to the narrow cone of particles produced by the hadronization of a single quark or gluon ([72], [63], [73]).
An example of such an event, recorded in 2017 by ATLAS, one of the four main experiments at the LHC, is shown in Figure 2.6.

In general, limits on the cross-section of this process as a function of the DM mass can be derived from both ATLAS and CMS data [64]. This channel is sensitive to a wide range of models, considering different types of mediators; in particular, scalar, pseudoscalar, vector, and axial-vector mediators can be probed in an s-channel process, while colored mediators (which can couple quarks to DM) can also be investigated through a t-channel process [62]. Examples of Feynman diagrams of these processes are shown in Figure 2.7.

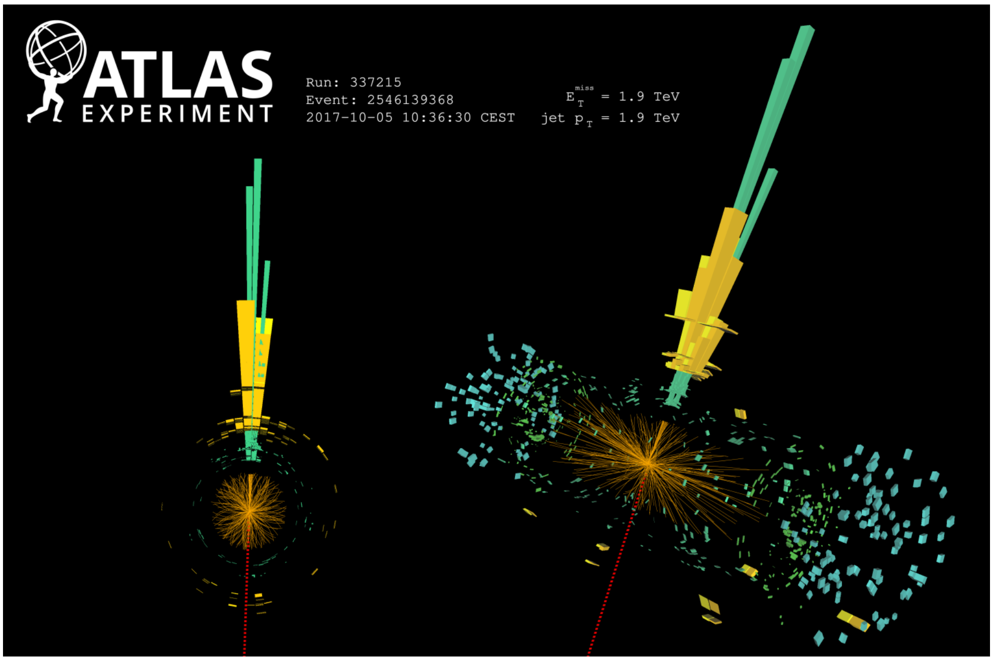


**Figure 2.6.** A monojet event recorded by the ATLAS experiment in 2017, with a single jet of 1.9 TeV transverse momentum recoiling against corresponding missing transverse momentum. The green and yellow bars show the energy deposits in the electromagnetic and hadronic calorimeters, respectively. The missing transverse energy (MET) is shown as the red dashed line on the opposite side of the detector. Credits: ATLAS Collaboration.

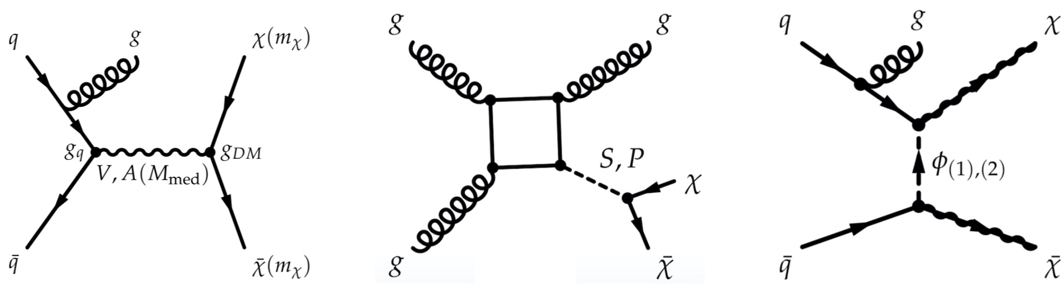


(a) (b) (c)

**Figure 2.7.** Feynman diagrams of (a) DM pair production in association with a parton via a vector or axial-vector mediator; (b) process exchanging a scalar or pseudoscalar mediator, leading to a monojet signature; (c) DM pair production through a colored mediator. Credits: [62].

These monojet events at colliders have been widely used to probe different DM models. The strongest constraints are typically obtained for mediator masses in the 100–1000 GeV range, with the best bounds above 200 GeV coming from ATLAS and from the Collider Detector at Fermilab (CDF). For mediator masses below 30 GeV, however, the monojet bounds are weaker than those in the contact interaction limit[3] [74].

#### Mesons decays at Colliders

Strong constraints on hadronically-interacting DM can also be given by hadron decays; in particular, rare meson decays to invisible final states, such as $B \to K + \not{E}_T$ [4], $B \to \pi + \not{E}_T$ and $K \to \pi + \not{E}_T$ can be interpreted as DM signatures like $B \to K + \bar{\chi}\chi$, $B \to \pi + \bar{\chi}\chi$ and $K \to \pi + \bar{\chi}\chi$ and therefore can be used to place stringent bounds on DM models with a light mediator [75].

A lot of experiments have been and are actively searching for signals of light DM through rare meson decays and missing energy signatures, offering complementary sensitivity to different couplings and mass ranges. The strongest constraints derive from the following experiments:

- ***Belle II***: is a B-factory experiment located at the SuperKEKB accelerator in Japan. It is an electron-positron collider and operates as a flavor factory at the intensity frontier, aiming to improve the precision of Standard Model measurements. Belle II studies rare decays of B mesons with high precision and large statistics. It is particularly sensitive to processes involving missing energy, making it an excellent probe for sub-GeV DM and light mediators [76];

- ***LHCb***: located at CERN, is a proton-proton collider designed to search for new physics by performing precise measurements in the heavy-flavor sector of the Standard Model. Therefore, it is designed to study the decays of b- and c-hadrons produced in proton-proton collisions. Its excellent vertex and particle identification capabilities make it ideal for investigating flavor physics and rare decays, including those with invisible final states such as $B \to K^*\bar{\chi}\chi$ [77];

- ***BaBar***: it was an electron-positron collider, born to be a B-factory at SLAC in the United States; its primary goal was the systematic study of CP asymmetries in the decays of neutral B mesons, therefore a large dataset of B meson decays has been collected. Although no longer running, its data are still used to set competitive limits on light DM through analyses of rare and invisible decays [78];

- ***NA62***: it is a fixed-target experiment at CERN, in which a proton beam is impinging on a beryllium target. The experiment focuses primarily on measuring the ultra-rare decay $K^+ \to \pi^+\bar{\nu}\nu$. Due to its precise control of backgrounds and missing energy signatures, NA62 also places strong constraints on models of light DM and invisible decays of kaons [79].

Only to cite an example, in the following, I present the bounds from K-meson decays from Ref. [80]. Analogous bounds could also be derived from B decays.

[3] This analysis was originally performed for non-standard neutrino–quark interactions, but the results also directly apply to light DM searches.

[4] This is a flavor-changing neutral current, predicted by the SM as a loop signature; furthermore, if we assume that the DM couples with a quark, this can be interpreted as DM signature.

The measurement of the Branching Ratio for the kaon SM decay into a pion and a neutrinos pair, $BR(K^+ \to \pi^+\bar{\nu}\nu) = (1.06 \pm 0.4)10^{-10}$ [81], places a strong upper bound on the branching ratio to other invisible final states, including DM. Making the simplifying approximation that the signal acceptance at NA62 is the same for the decays $K^+ \to \pi^+\bar{\nu}\nu$ and $K^+ \to \pi^+\bar{\chi}\chi$ and requiring consistency with the measurement at $2\sigma$, this leads to the bound $BR(K^+ \to \pi^+\bar{\chi}\chi) < 10^{-10}$; this upper limit can also be translated into a bound on the DM–nucleon cross-section. The exclusion region obtained in this way is presented in Figure 2.8.

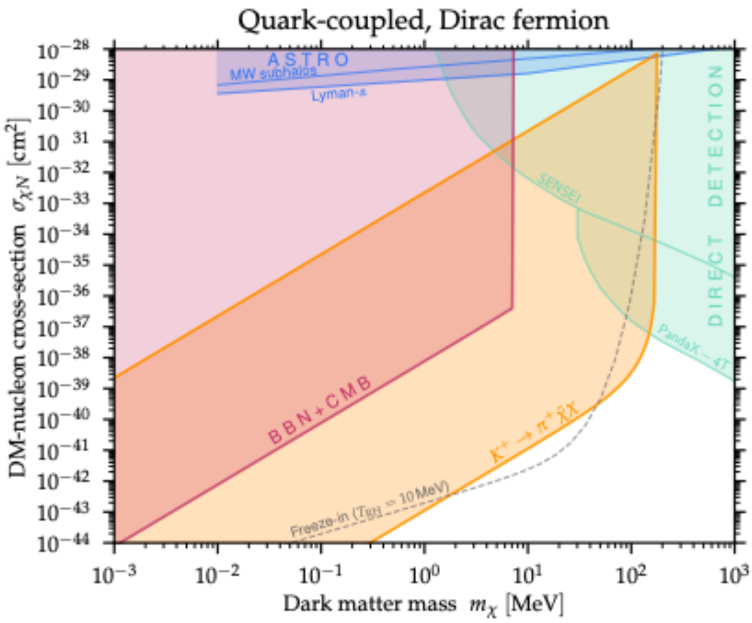


**Figure 2.8.** Constraints on the DM–nucleon cross-section. The red shaded regions are excluded by BBN+CMB. The orange region is excluded by $K^+ \to \pi^+\bar{\chi}\chi$. The gray lines denote where the freeze-in process $\gamma\gamma \to \bar{\chi}\chi$ yields the observed relic abundance. The blue and green regions are excluded by existing bounds from structure formation and direct detection experiments, respectively. Credits: [80].

# CHAPTER 3

# Neutrino Telescopes as Dark Matter Detectors

Over the past few decades, many experiments have been built and entirely dedicated to the search for dark matter. In addition, the results of already existing experiments, originally designed for other purposes, have been studied to derive sensitivity limits for the numerous dark matter models proposed to date.
In particular, neutrino telescopes such as IceCube at the South Pole [82], KM3NeT in the Mediterranean Sea [83], and Baikal-GVD in Lake Baikal [84] have already been used in indirect dark matter searches (see Refs. [85], [86] and [87]).

The aim of this thesis is to explore the use of large neutrino detectors, and in particular IceCube, as *direct* DM detectors, relying on the high-energy DM populations that are necessarily induced by DM-CR scatterings in the galaxy. As the detection method of these experiments is crucial for this endeavour, this Chapter provides a general overview about it. First, Section 3.1 provides an introduction to neutrino phenomenology, followed by an overview of cosmic ray phenomenology in Section 3.2 and Cherenkov radiation in Section 3.3. In Section 3.4, the main neutrino signatures in this type of detector are presented, and finally, Section 3.5 discusses the advantages of using IceCube for direct dark matter searches.

## 3.1 Overview of Neutrinos' Phenomenology

Since Wolfgang Pauli proposed the existence of the neutrino in 1930, and it was later discovered in 1956 by Frederick Reines and Clyde L. Cowan [88], the neutrino has played an essential role in our understanding of nuclear and particle physics.
The investigation into its basic properties has been a particularly active area of research in the past years. Research conducted over the latter half of the $20^{\text{th}}$ century has revealed, for example, that neutrinos can no longer be considered massless particles as in the Standard Model, representing the first significant alteration to the theory. Furthermore, in recent years, neutrino experiments have been crucial in understanding the properties of ordinary matter in a deeper way [89].

### 3.1.1 Neutrinos' Properties

In the SM, neutrinos are considered as neutral massless particles that can interact only weakly with other particles. Even if SM is based on the gauge group $SU(3)_C \times SU(2)_L \times U(1)_Y$, as far as neutrinos are concerned, we can disregard the color group $SU(3)_C$ and focus only on the electroweak subgroup $SU(2)_L \times U(1)_Y$ [90].
As discovered in 1998 by the Super-Kamiokande experiment and in 2001 by the Sudbury Neutrino Observatory, neutrinos oscillate and therefore possess mass [91]. Hence, it is necessary to extend the Standard Model to incorporate neutrino masses.

Thanks to the work of many physicists, who have developed both Beyond Standard Model theories and experimental techniques, we now have a deep understanding of neutrinos. The main properties of these particles [90] are:

- ***elementary particles***: they are subatomic fundamental particles, belonging to the family of leptons. They're fermions with spin equal to $1/2$;

- ***gravitationally and weakly interacting***: they interact with ordinary matter only through gravity and weak interaction. Since the interaction strength is really weak, neutrinos are optimal probes of dense and far environments;

- ***electrically neutral***: they are chargeless regarding the electromagnetic interaction, therefore they do not interact electromagnetically;

- ***three flavors***: there exist three neutrino flavors, relative to the three charged leptons. They are electron neutrino $\nu_e$, muon neutrino $\nu_\mu$, tau neutrino $\nu_\tau$ and the respective three anti-neutrinos;

- ***oscillations***: as discovered from both Super-Kamiokande and Sudbury Neutrino Observatory, neutrinos can change flavor while they are travelling in space. This is a quantum process and is known as neutrino oscillations;

- ***massive***: the fact that neutrinos oscillate implies also that at least two of the three neutrinos have mass. Even if their mass is very small and not measured yet, we have derived upper limits from experiments. Up to now, the absolute values of neutrino masses have not been measured, but increasingly stringent upper limits have been established. For instance, regarding laboratory searches, the KATRIN experiment, which performs high-precision spectroscopy of tritium $\beta$-decay near its endpoint, has set an upper limit on the effective electron antineutrino mass of $m_{\bar{\nu}_e} < 0.45$ eV ($90\%$ C.L.) [92]. Cosmological observations provide even stronger constraints, under certain assumptions. In particular, combining CMB data with baryon acoustic oscillations and gravitational lensing, and assuming the $\Lambda$CDM model, the current upper limit on the sum of the three neutrino masses is $\sum m_\nu < 0.07$–$0.12 eV$ ($95\%$ C.L.) [93].

### 3.1.2 Neutrinos Interactions with Ordinary Matter

Neutrinos interact with ordinary matter primarily through weak interactions, mediated by either charged $W^\pm$ or neutral $Z^0$ bosons [90]. These interactions all fall within the general gauge theory of $SU(2)_L \times U(1)_Y$; therefore, we can classify the neutrino interactions first according to the interaction type and then according to the interaction regime [89].

### Interaction Type

Depending on the mediator exchanged during the interaction [94], we can have:

- ***Neutral Current interactions* (NC)**: they are mediated by the exchange of a neutral $Z$ boson;
- ***Charged Current interactions* (CC)**: they are mediated by the exchange of a charged $W^{\pm}$ boson.

In Figure 3.1, the Feynman diagrams for these two kinds of interaction are shown.

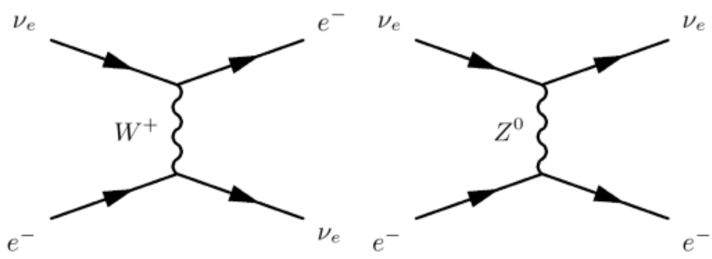


**Figure 3.1.** Feynman tree-level diagram for charged and neutral current components of $\nu_e + e \to \nu_e + e$ scattering. Credits: [89].

### Interaction Regimes

Then, according to the initial neutrino energy $E_\nu$ and the final state, neutrino interactions with nucleons can be classified [89] as:

- **Inverse Beta Decay (IBD), *low energy*** ($E_\nu \sim 1 - 100$ MeV): relevant for reactor and solar electron anti-neutrino $\bar{\nu}_e$. The reaction that occurs is a Charged Current interaction, such that

$$\bar{\nu}_e + p \to n + e^+ \, ; \tag{3.1}$$

- **Quasi-Elastic Scattering (QE), *intermediate energy*** ($E_\nu \sim 0.1 - 20$ GeV): for neutrino energies less than $\sim 2$ GeV, this is the predominant neutrino-hadron interaction. In a QE interaction, the neutrino scatters off an entire nucleon rather than its constituent partons. In a charged current neutrino QE interaction, the target neutron is converted to a proton. In the case of an anti-neutrino scattering, the target proton is converted into a neutron:

$$\nu_\ell + n \to \ell^- + p \qquad \text{and} \qquad \bar{\nu}_\ell + p \to \ell^+ + n \, , \tag{3.2}$$

where $\ell$ is a charged lepton;

- **NC elastic scattering, *intermediate energy*** ($E_\nu \sim 0.1 - 20$ GeV): neutrinos can also elastically scatter from nucleons via Neutral Current interactions, such as

$$\begin{aligned} \nu + p \to \nu + p\,, \quad & \bar{\nu} + p \to \bar{\nu} + p\,, \\ \nu + n \to \nu + n\,, \quad & \bar{\nu} + n \to \bar{\nu} + n\,. \end{aligned} \tag{3.3}$$

- **Resonant Production, *intermediate energy***, ($E_\nu \sim 0.1 - 20$ GeV): this is an inelastic interaction where neutrinos, if they have enough energy, can excite the nucleon to an excited state. In this case, the neutrino interaction produces a baryonic resonance, which quickly decays. For example, one of the most common final states is the *single pion production*:

$$\begin{aligned} \nu_\ell + N \to \ell^- + & N^* \\ & N^* \to \pi N'\,, \end{aligned} \tag{3.4}$$

where $N, N' = n, p$ and $N^*$ is the baryon resonance.

- **Deep Inelastic Scattering (DIS), *high energy*** ($E_\nu \gtrsim$ few GeV): neutrino scatters off a quark in the nucleon via the exchange of a virtual $W^\pm$ or $Z$ boson, producing a lepton and a hadronic system in the final state. Both Charged Current and Neutral Current processes are possible:

$$\begin{aligned} \nu_\ell + N \to \ell^- + X\,, \quad & \bar{\nu}_\ell + N \to \ell^+ + X\,, \\ \nu_\ell + N \to \nu_\ell + X\,, \quad & \bar{\nu}_\ell + N \to \bar{\nu}_\ell + X\,, \end{aligned} \tag{3.5}$$

where $X$ is the hadronic resonance and $N = n, p$.

In Figure 3.2, the cross-sections as a function of the neutrino energy are shown; in this plot, it is noticeable that the dominant interaction channel depends on the initial neutrino energy.

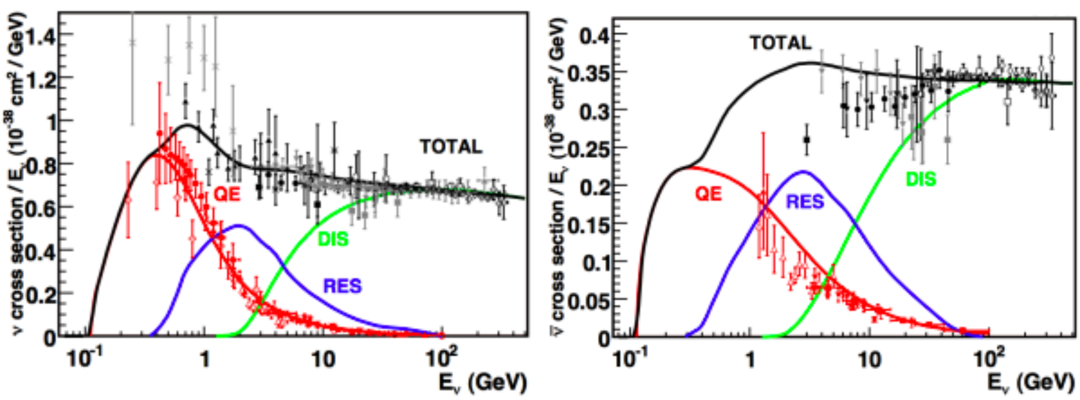


**Figure 3.2.** Muon neutrino (left) and anti-neutrino (right) charged-current cross-section as a function of neutrino energy. The contributing processes in this energy region include quasi-elastic (QE) scattering, resonance production (RES), and deep inelastic scattering (DIS). Credits: [95].

## 3.2 Overview of Cosmic Rays' Phenomenology

Cosmic rays (CRs) are high-energy charged particles that are generated outside our atmosphere, in astrophysical environments; they were discovered in 1912 by Victor Hess while he was conducting some experiments on radioactivity [96].
Since then, a lot of progress has been made towards revealing their composition and their origin: although the sources of cosmic rays are still uncertain, their composition is determined to consist mostly of free protons ($79\%$) and helium nuclei ($15\%$) [97].
In Figure 3.3, the Primary Cosmic Rays' Spectrum, as a function of kinetic energy per primary particle, is shown.

Among the most plausible astrophysical sources of primary cosmic rays are supernova remnants, active galactic nuclei (AGNs), and gamma-ray bursts (GRBs), although no single class of sources can yet account for the full observed spectrum [98].

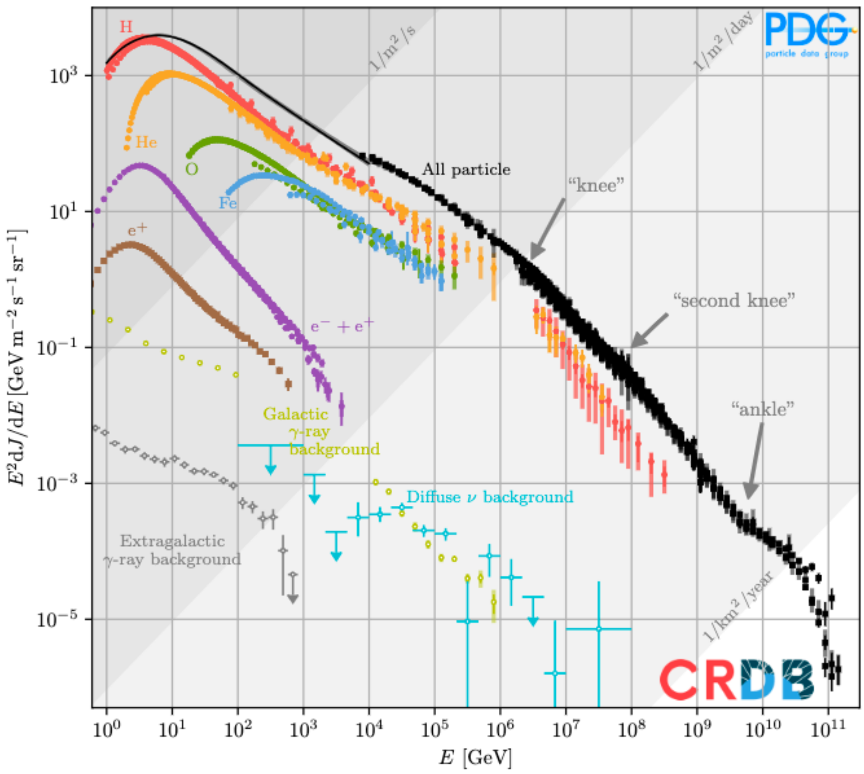


**Figure 3.3.** Spectrum of primary Cosmic Rays: the measurements of the intensity of charged and neutral CRs, multiplied by kinetic energy squared, are shown. Credits:[99].

This spectrum extends over several orders of magnitude in energy and shows characteristic features such as the steepening around $3 \times 10^{15}$ eV, called the *knee*, and the flattening starting at $10^{19}$ eV, called the *ankle* of the spectrum. These are the cosmic rays originating from astrophysical sources and so-called primary cosmic rays; then, whenever a primary cosmic ray hits the Earth's atmosphere, it produces a cascade of secondary particles which forms air showers [96].
These showers include a variety of particles such as pions, muons, electrons, neu-

trinos, and photons, which can be detected at ground level or by underground and underwater detectors. In Figure 3.4, a possible evolution of the air shower is shown; as illustrated in this figure, the shower is made up of three main components: muonic, hadronic, and electromagnetic. Additionally, so-called *atmospheric neutrinos* are produced by the interaction between CRs and nuclei in the atmosphere.

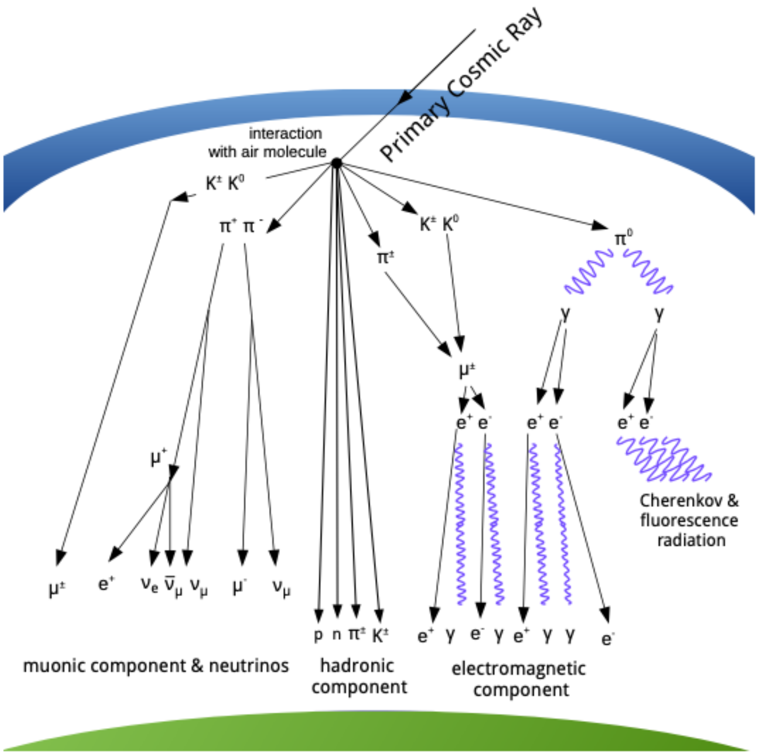


**Figure 3.4.** Diagram of the possible evolutions of a cosmic ray air shower. Credits: [100].

## 3.3 Cherenkov Radiation

All the possible neutrino interactions described in Section 3.1.2 can be detected through the charged particles produced in their interactions, thanks, for instance, to the Cherenkov effect. It is therefore necessary to explain what the Cherenkov effect is.

The basic idea is to detect Cherenkov radiation emitted by a dielectric medium, such as water or ice, when a charged particle propagates at a sufficient speed through it[101]. If the particle's speed is greater than the speed of light in that medium, the dielectric molecules polarized by the charged particle emit an electromagnetic radiation at a certain angle, called Cherenkov angle, given by

$$\cos\theta_C = \frac{1}{n\beta}, \tag{3.6}$$

where $n$ is the refracting index of the medium and $\beta$ is the ratio between the particle's speed and the speed of light $\beta = v/c$ [102].

The propagation of this electromagnetic shock wave through the medium is illustrated in Figure 3.5. This non-isotropic emission looks like a cone aligned with the direction of the charged particle, allowing the reconstruction of the direction of its propagation. It is then possible, using kinematics and conservation laws, to identify the direction of the incoming neutrino if the charged particle is the corresponding lepton produced in a charged current interaction.

As previously mentioned, the charged particle must travel faster than the light speed in the medium to have such radiation; from this condition, one can obtain the energy threshold for the Cherenkov effect:

$$E_{\text{th}} = \frac{mc^2}{\sqrt{1-n^{-2}}}\,; \tag{3.7}$$

this threshold value depends on the refractive index of the medium. As an example, considering ice as dielectric material and a refractive index equals to $1.33$, the energy threshold for the kinetic energy is about $0.3$ MeV for electrons, $54.6$ MeV for muons and $914.7$ MeV for taus [103].

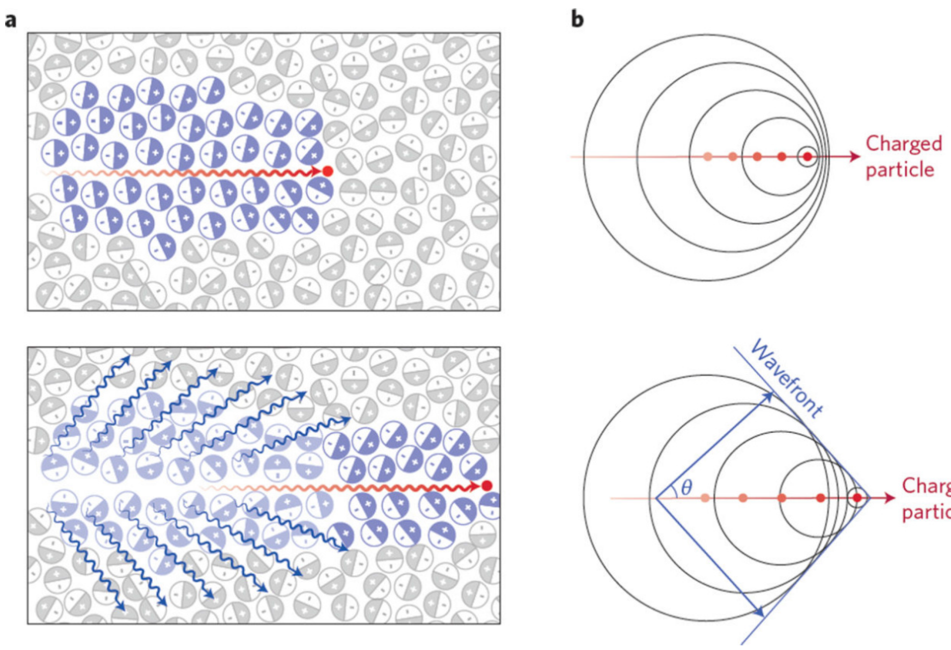


**Figure 3.5.** The generation of Cherenkov light (CL). (a) Top: A charged particle (red dot) travelling faster than light in a medium polarizes the medium. Bottom: As the medium returns to the ground state, CL (blue wavy lines) is emitted in a forward direction. (b) Top: Analogous to a sonic boom, coherent waves are produced through the Cherenkov mechanism. Bottom: As the particle travels forward, the wavefront propagates at a forward angle $\theta_C$ with light being emitted in the direction of travel. Credits: [104].

Finally, one can also derive the photon yield expected in the detector; as the energy threshold, it also depends on the refractive index of the medium [102]. The Frank-Tamm formula allows for the estimation of the number of Cherenkov photons with a wavelength $\lambda$ emitted per unit length x:

$$\frac{d^2N}{dxd\lambda} = \frac{2\pi\alpha}{\lambda^2}\left(1 - \frac{1}{\beta^2 n^2 \lambda}\right), \tag{3.8}$$

with $\alpha$ being the fine structure constant [105].
Integrating this expression over the range $300 - 600$ nm, which corresponds to the sensitivity window of the IceCube sensors, and using the refractive index of ice, yields an emission of approximately $330$ photons per centimeter along the track of a relativistic charged particle [103].

## 3.4 Neutrinos detection in Water and Ice

Because of their low interaction cross-section with matter, neutrinos are considered elusive particles, which is why massive and expensive detectors are required to achieve appreciable event rates. For instance, an electron anti-neutrino with energy $E_{\bar{\nu}_e} \sim 1$ MeV, has a cross-section of $\sim 10^{-44}$ cm$^2$, therefore only one neutrino out of $10^{11}$ interacts when travelling along the Earth's diameter [96].
Moreover, the interesting feature of neutrinos, in which they differ from protons and photons, is that they can travel through the Universe without being deflected and absorbed, and therefore carry precious information about their source [106].

In this Section, the main characteristics of neutrino detection through Cherenkov radiation produced by the secondary charged particles are presented.
This detection method has its origins in an idea of Mosey Markov that, in the 1960s, proposed to install detectors deep in a lake or the sea and to determine the direction of charged particles with the help of Cherenkov radiation [101].

### 3.4.1 Neutrino Detection Principle

The basic principle of a **Neutrino Telescope** is a grid of light detectors inside an instrumented volume in a transparent medium [106]. This transparent material, as water or ice at great depths, performs several functions [96]:

- in its large volume, it provides numerous free target nucleons for neutrino interactions;
- it is also a shield against secondary particles produced by CR interactions;
- it is the medium in which the Cherenkov photons, produced by relativistic particles, propagate.

In these experiments, neutrinos are detected through charged particles produced by neutrino-nucleon interactions, both Neutral and Charged current (as presented in Section 3.1.2); these charged particles, if relativistic, emit Cherenkov Radiation in the dielectric medium [102], which can be detected.

The charged particles travel through the medium until they decay or interact; the path length travelled by particles in the medium depends on their initial energy and the energy loss [107]. Depending on the kind of event recorded by the telescope, one can obtain information about the primary neutrino, since, depending on the particle's type, the signature is different; these signatures are presented in Figure 3.6. Moreover, no separation between neutrinos and anti-neutrinos is possible, since neutrinos and anti-neutrinos signatures are indistinguishable.
The two main classes of events are *tracks* and *showers*, as briefly described in the following.

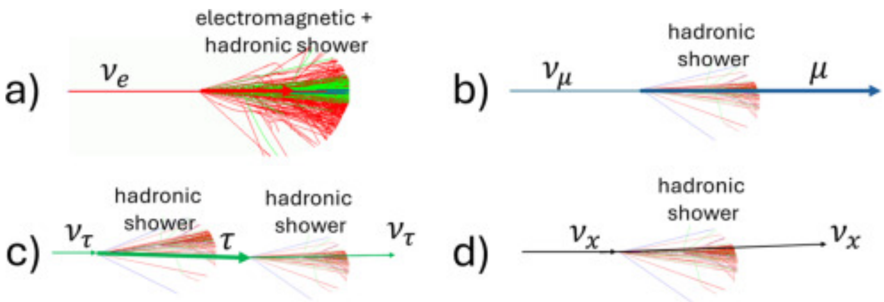


**Figure 3.6.** Main event signature topologies for different neutrino flavors and interactions: a) CC interaction of $\nu_e$ that produces both an electromagnetic and a hadronic shower; b) CC interaction of a $\nu_\mu$ that produces a muon and a hadronic shower; c) CC interaction of a $\nu_\tau$ that produces a $\tau$ that subsequently decays; d) a NC interaction produces a hadronic shower. Particles and antiparticles cannot be distinguished in neutrino telescopes. Credits: [108].

**Neutrino-Induced Tracks**

As shown in diagram b) of Figure 3.6, the muon neutrino that crosses the detector can undergo a CC interaction, producing a muon. Since the muon is a minimum ionizing particle, that is a particle with a tiny energy loss, the typical signature that leaves in the detector is a *track* [109]; the signature that this kind of event leaves in the detector is presented in Figure 3.7. This allows for an accurate reconstruction of muon direction, and therefore also of the neutrino direction [107].

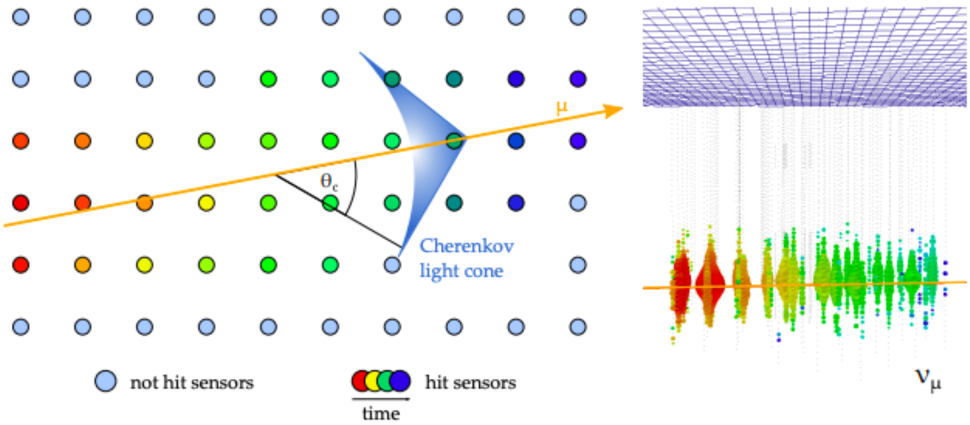


**Figure 3.7.** Track event: illustration of a muon traveling through a regular lattice of photo sensors (left) and a corresponding IceCube event view (right). Credits: [110].

**Neutrino-Induced Showers**

In addition to track-like events, shower-like events can be induced in the detector, which have a more complex signature, given by a multitude of particles. Showers can be *electromagnetic*, if induced by an electron neutrino and composed of photons, electrons and positrons, or *hadronic*, if they are composed of hadrons [108]. Therefore, while track events can arise only by a CC muon (anti)neutrino interaction, showering events can arise from several channels [96]:

- electron (anti)neutrino CC interactions: a high-energy electron resulting from a CC $\nu_e$ interaction, can radiate a photon via the Bremsstrahlung effect[1]. This induces the development of an electromagnetic shower with a lateral extension negligible with respect to the transversal one. Therefore, in good approximation, this shower represents a point source of Cherenkov light, emitted almost isotropically along the shower axis. This is shown in diagram a) of Figure 3.6;

- tau (anti)neutrino CC interactions: here the final-state lepton is a tau, which travels some distance[2], then it decays and produces a second shower; strictly speaking it produces a second cascade only if it doesn't decay to muon which happens in approximately $17.39\%$ of cases [99]. Because of the presence of two showers, this signature is called *double-bang* and can be detected if both the $\nu_\tau$ and $\tau$ interactions happen inside the detector. This is shown in diagram c) of Figure 3.6;

- all flavor (anti)neutrino NC interactions: the signature in this channel is the same for all neutrino flavors. Such an event is characterized by the non-observation of a fraction of the initial energy of the incoming neutrino, which is carried away by the secondary neutrino. This is shown in diagram a) of Figure 3.6.

The signatures of shower-like and double-bang events induced in the detector are shown, respectively, in Figures 3.8 and 3.9.

[1] The radiation of a photon typically happens after few tents of cm of water or ice, since the radiation length in water is $\sim 36$ cm [96].

[2] The distance travelled by the tau inside the detector depends on its initial energy; for the range of interest of neutrino telescopes, this path is usually from a few meters up to a few kilometers [96].

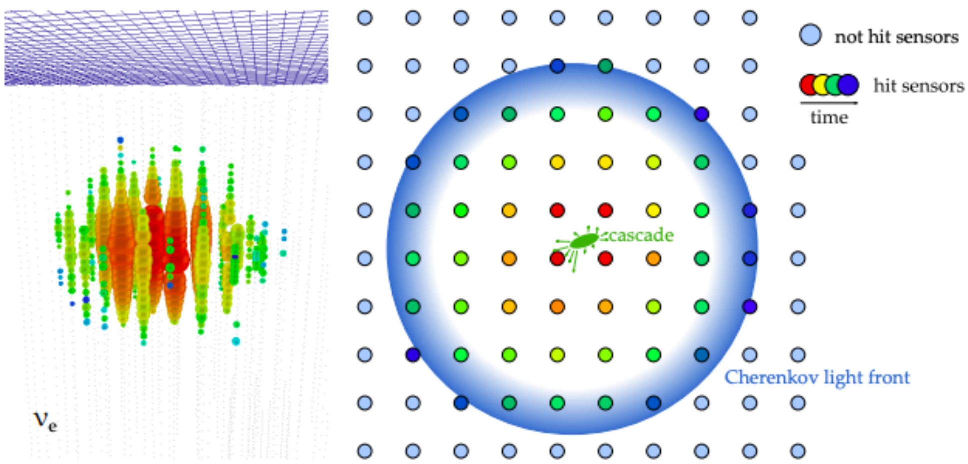


**Figure 3.8.** Shower event: illustration of a cascade in a regular lattice of photo sensors (right) and a corresponding IceCube event view (left). Credits: [110].

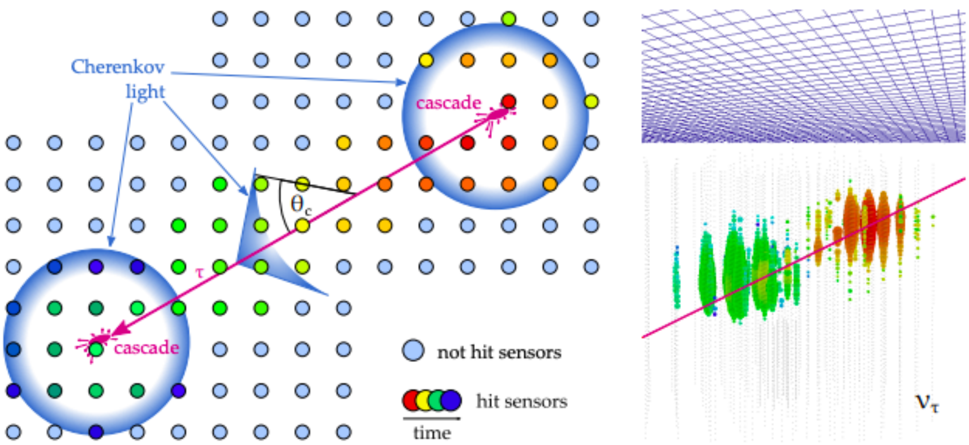


**Figure 3.9.** Double-bang event: illustration of a high-energy tau event in a regular lattice of photo sensors (left) and a corresponding IceCube event view of a simulated event (right). Credits: [110].

## 3.5 Why IceCube for Dark Matter Searches?

IceCube is the first gigaton-scale, cubic-kilometer neutrino detector ever built. Although it was primarily designed to observe neutrinos from the most violent astrophysical sources in our universe, it can be also a powerful tool for DM searches, given the extremely weak interaction strength of DM, comparable to that of neutrinos. It is also the largest neutrino telescope built to date, providing a very large effective area, which is particularly advantageous when searching for rare processes such as DM-induced interactions, as it enables the study of signals with very low cross-sections.

Furthermore, being located underground and embedded in the Antarctic ice, IceCube benefits from a significant reduction in background, primarily from atmospheric muons and neutrinos.

Moreover, thanks to DeepCore (see Section 4.1.1 for details) and innovative selection criteria, IceCube is sensitive to neutrinos with energies $E_\nu \sim 1-100$ GeV, precisely the energy range where our expected DM flux, induced by CR-DM scatterings, is peaked.

Finally, we can use data corresponding to a 13-year livetime and a target volume of hundreds of Megatons. This, combined with the large detection volume and the long exposure time, has the potential to significantly improve the sensitivities with respect to analogous existing searches, which reached at most tens of kilotons at Super-Kamiokande ([111], [6]).

To conclude, this is a case study that opens the way for the use of next-generation neutrino telescopes as dark matter direct detectors, since the general approach adopted in this work is applicable to a broad class of experiments.

# CHAPTER 4

# The IceCube Neutrino Observatory

The analysis presented in this work starts from the IceCube neutrino effective areas, which are then converted into dark matter effective areas, as described in Chapter 5. IceCube is a neutrino telescope located at the geographic South Pole, designed to record the Cherenkov emission produced by high-energy charged particles traversing the detector volume, via the detection method described in Section 3.3.

In this chapter, the principal features of this telescope are introduced. First, in Section 4.1, a general description of the detector is provided. Then, in Section 4.2, the main features of noise and backgrounds in IceCube are presented. Lastly, in Section 4.3, the two principal event selections employed in this analysis, *ELOWEN* and *GRECO*, are introduced.

## 4.1 IceCube Overview

Developments in neutrino astronomy have been driven by the search for the CRs sources, leading, at an early stage, to the concept of a cubic-kilometer neutrino detector. Cosmic rays are the highest energy particles ever observed, with energies over a million times those reached by today's particle accelerators on Earth [IceCube Collaboration site].
To prove that the extremely clear Antarctic ice was suitable for detecting energetic neutrinos, in the mid-1990s, the Antarctic Muon and Neutrino Detector Array (AMANDA) was built [112]. Starting from the results of AMANDA, the IceCube detector was gradually developed in several years; the deployment started in 2005, when the first string was lowered in the ice, and the detector was completed on December 18, 2010. There have been many analyses for each detector configuration, as the detector started taking data once the first string was deployed, allowing numerous analyses to be conducted as more strings were added.

### 4.1.1 Detector Layout

IceCube is a cubic-kilometer neutrino observatory made of Antarctic ice and located near the Amundsen-Scott South Pole Station. The detector is placed deeply in the ice

for two reasons: first, because the upper ice sheet provides a natural filter against low-energy cosmic rays, and secondly, because the ice at this depth has a high transparency for visible light.
In addition to the main *In-Ice* array, IceCube includes a surface detector (*IceTop*) and a more densely instrumented core (*DeepCore*). The detector configuration is presented in Figure 4.1.

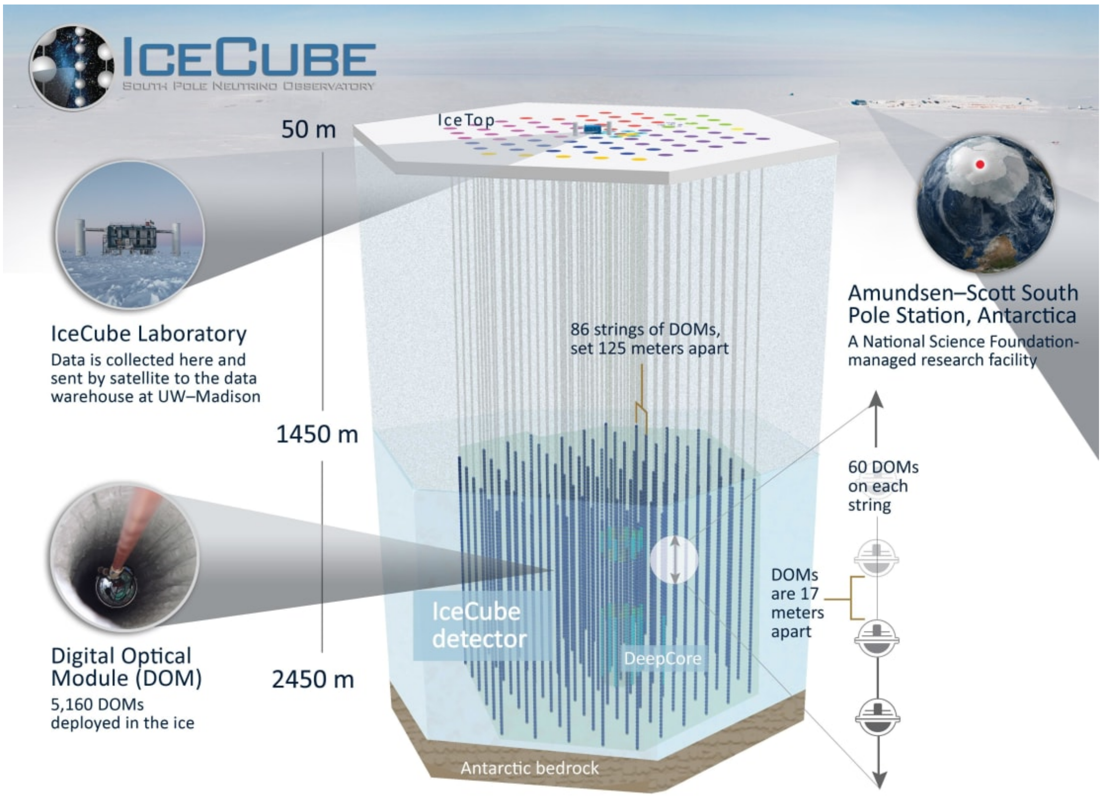


**Figure 4.1.** A schematic view of the IceCube detector with its components DeepCore and IceTop. Credits: [IceCube Collaboration site].

This layout significantly enhances the capabilities of the observatory, making it a multipurpose facility [107]. These three main components differ in both their layout and scientific goals; a brief overview of each is provided below:

- **IceTop Array**: this is an air shower array; it consists of 81 stations, located on top of the same number of IceCube strings, each hosting two frozen water tanks instrumented with two DOMs each, for a total of 324 DOMs. IceTop, built as a veto and calibration detector for IceCube, also detects air showers from primary cosmic rays in the range of about 300 TeV to 1 EeV and reveals their composition and characteristics [113];

- **Main In-Ice Component**: it consists of 5,160 digital optical modules (DOMs), arranged in 86 strings (including 8 DeepCore strings), arrayed over a cubic kilometer from 1,450 meters to 2,450 meters depth. The strings are deployed on a hexagonal grid with 125-meter spacing and hold 60 DOMs each. The vertical separation of the DOMs is 17 meters. The In-Ice Component can detect neutrinos with energies $E_\nu \geq 100$ GeV. The strings and DOM spacings have been optimized for the primary scientific goal of IceCube, namely the detection of High-Energy Extraterrestrial Neutrinos [114];

- **Deep-Core Subdetector**: it is formed by 7 standard IceCube strings plus 6 additional special strings. Thanks to this configuration, the spacing between each DOM is smaller with respect to the In-Ice Component, with a horizontal separation of about 70 meters and a vertical DOM spacing of 7 meters. This subdetector lowers the neutrino energy threshold to about $E_\nu \geq 10$ GeV, creating, among many other things, the opportunity to study neutrino oscillations[115].

### 4.1.2 The Digital Optical Module

As previously introduced in Section 3.3, neutrinos are not observed directly, but when they interact with the ice they produce electrically charged secondary particles that in turn emit Cherenkov light. These Cherenkov photons are recorded by Digital Optical Modules (DOMs), making these DOMs the centerpieces of the IceCube detector. Therefore, DOMs are the fundamental light sensor and data acquisition units for IceCube; a picture and a schematic view of a DOM are reported in Figure 4.2.

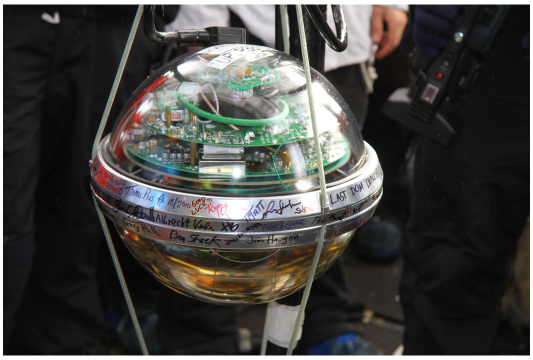

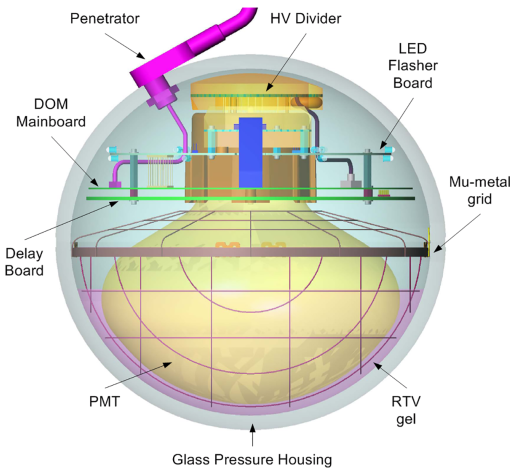


**Figure 4.2.** Left: Picture of the last Digital Optical Module, installed inside the detector in December 2010. Right: Schematic view of the DOM's major components.
Credits: [IceCube Collaboration site].

Each DOM contains a downwards oriented 10-inch Photomultiplier Tube (PMT) to record the photons, along with a DOM Mainboard (DOM MB) to further process and digitize the signal. The PMT, which is in contact with the glass via a transparent silicone gel, and the DOM MB are powered by a $2$ kV high voltage power supply and is housed in a 13 mm thick glass sphere, capable of withstanding pressures to $70$ MPa [82].

A photon, to be detected, first it has to reach the DOM and to cross the glass sphere and the silicon gel to arrive at the PMT, where it can then be absorbed by the photocathode. After absorption, a photo-electron is emitted, which is amplified by a factor $10^7$ as it passes $10$ dynodes. This amplified signal is read out as a change in voltage of the anode in the PMT and is passed to the DOM MB for further processing[116].
Finally, the IceCube Laboratory on the surface converts the messages from individual DOMs into light patterns that reveal the direction and energy of muons and neutrinos.

### 4.1.3 Triggering and Filtering

Once the various expected signatures have been described, it becomes essential to distinguish signal from background. To achieve this, several aspects are taken into account. First, we examine whether hits from neighboring DOMs occur within a short time window. If two or more neighboring or next-to-neighboring DOMs register hits within a $\pm 1\mu\mathrm{s}$ window, these hits are tagged as *Hard Local Coincidence* (HLC). In contrast, if no such coincidence is found, the isolated hit is classified as a *Soft Local Coincidence* (SLC) [82].

At this stage, the resulting data sample is still largely dominated by noise. To reduce this noise, IceCube applies trigger conditions based on time coincidences. The main trigger is the *Simple Majority Trigger*, or SMT-8, which requires at least 8 DOMs with HLC pulses to occur within a $5\mu\mathrm{s}$ window. To lower the energy threshold and improve sensitivity to low-energy events in the DeepCore, a softer trigger condition can be used, as the SMT-3. The SMT-3 trigger works similarly to the SMT-8, but requires only 3 DOMs with HLC pulses within a $2.5\mu\mathrm{s}$ window [82].

Once an event satisfies the trigger conditions, it is passed through a series of filters designed to select events of particular physical interest. For example, the *Cascade Filter* identifies cascade-like events, while the *Extremely High Energy Filter* targets events associated with extremely high-energy neutrino interactions. Another important filter is the *DeepCore Filter*, which acts as a veto against certain atmospheric muons [103].

## 4.2 Noise and Backgrounds in IceCube

In typical data-taking conditions, most of the hits recorded in the detector are due to detector noise, while only a small fraction corresponds to real neutrino interactions [103]. Therefore, before discussing the event selection, a brief introduction to the backgrounds in IceCube and about how noise hits are removed is presented.
Before any filtering, detector dark noise is the dominant source [100]. However, after the application of filters such as *NoiseEngine* [103], its contribution becomes subdominant compared to atmospheric muons and neutrinos.

### 4.2.1 Atmospheric Muons and Neutrinos

Atmospheric muons and neutrinos are produced by CRs interactions with Earth's atmosphere. Up to energies of about $E \sim 100$ TeV, they are primarily generated from

the decay of charged pions and kaons in the resulting air shower cascades. Additionally, low-energy neutrinos are also produced from the decay of muons [96].
Atmospheric muons are approximately five orders of magnitude more abundant than muons produced by cosmic neutrino interactions inside IceCube. As a result, identifying and rejecting this background is crucial for neutrino analyses [103]. These muons can penetrate several kilometers into ice or water, constituting the majority of reconstructed events in large-volume neutrino detectors.
In IceCube, the atmospheric muon event rate is typically between 2.6kHz and 3.0kHz. Although many muons do not trigger the detector, they may still leave detectable signals. In particular, the number of HLC hits is a good indicator for the rate of triggered atmospheric muons per DOM, since HLC hits are unlikely to be caused by the DOMs' intrinsic dark noise [117]. Finally, to estimate the number of atmospheric muons that trigger the detector, CORSIKA (COsmic Rays SImulations for KAscade) simulations can be used.

A major challenge for neutrino telescopes is also the separation of astrophysical neutrinos from the background of atmospheric neutrinos produced in CR-induced air showers. Here again, CORSIKA and GENIE (Generates Events for Neutrino Interaction Experiments) simulations are useful to model and quantify this background contribution ([96], [117]).

### 4.2.2 DOM noise

Triggered and non-triggered atmospheric muons produce only a small fraction of the total amount of background hits in the detector. Most of the background in IceCube is given by the electron emission from the PMT's cathode in absence of a Cherenkov photon, which are pulses that are not directly caused by Cherenkov photons emitted from an ice-traversing charged particle; this is called *dark noise*.
The following discussion is based on and adapted from the comprehensive treatment found in Ref. [103] and in Ref. [100].

Several components contribute to the total amount of dark noise in a DOM; in the following, we illustrate the major ones:

- **Prepulses and Afterpulses**: these are PMT-induced effects, responsible for approximately $30$ Hz of DOM noise. In general, the PMT signal can be accompanied by *prepulses* when a photon bypasses the photocathode and hits one of the early dynodes directly to eject photoelectron; similarly, an *afterpulses* is attributed to ionization of residual gases by electrons that were accelerated in between the dynodes. These resulting ions are attracted to the photocathode and cause the liberation of electrons which follow the same amplification process of the original photoelectron. Laboratory measurements show that afterpulses arise most likely at $6\mu$s after the main peak, following a Gaussian distribution;

- **Uncorrelated Noise**: noise in the electronics of the DOMs as well as decay of radioactive elements in the PMTs and the pressure sphere glass, such as Potassium and Uranium, cause noise pulses of Poissonian nature. These noise components are temperature-dependent and follow Richardson's law for thermal emission;

- **Correlated Noise**: the origin of this contribution is not fully understood yet. Short-time interval hits happen with an increased rate compared to what expected from afterpulses; it follows that a non-thermal noise component dominates over thermal emission at temperatures below $200$K, with a rate that follows an exponential temperature dependence. This is a non-Poissonian noise component, with events that do not occur randomly but in sequences of shorts intervals, called noise bursts.

All these contributions add together and give a rate of $560$Hz for IceCube DOMs and $780$Hz for the DeepCore DOMs; moreover, cosmic-ray muons are expected to create a rate from $25$Hz to $5$Hz, decreasing with depth.

### 4.2.3 HitSpooling Data Stream

To better understand the various pure noise contributions, the IceCube collaboration has utilized the data stream known as HitSpool data [100], which is a raw data buffer[1] primarily designed to improve data acquisition for supernova neutrino analysis. This data-taking method records all hits within the detector in a continuous stream, in contrast to the typical triggered data approach.
This data stream allows us to save every neutrino interaction happening in the neighborhood of the detector, both triggering and sub-threshold interactions; this increases the effective volume for low-energy neutrinos.

Figure 4.3 compares the detector noise, with fits of the different contributions briefly described above, with the histogram of time differences between successive hits from HitSpool data.

### 4.2.4 The Vuvuzela Noise Model

This noise event generator is based on an empirical model consisting of three components inherent to IceCube DOMs: uncorrelated thermal noise, uncorrelated radioactive noise and correlated scintillation noise. The study of the behavior of these pure noise events allowed to development of an algorithm able to identify them [118].

As previously introduced in Section 4.2.2, the uncorrelated noise is given by two components: thermal and radiactive noise; the latter is due to radioactive decays within the glass of the DOM and PMT. For both components, the number of hits is treated as a Poissonian distribution and the hit times are sampled from a uniform distribution. In the thermal component, the number of hits is simulated with a rate dependent on the temperature of the DOM, while for the radioactive component the rate is independent of the temperature.

[1] A data buffer is a temporary memory storage used to hold data while it is being transferred between components, ensuring smooth and efficient data processing.

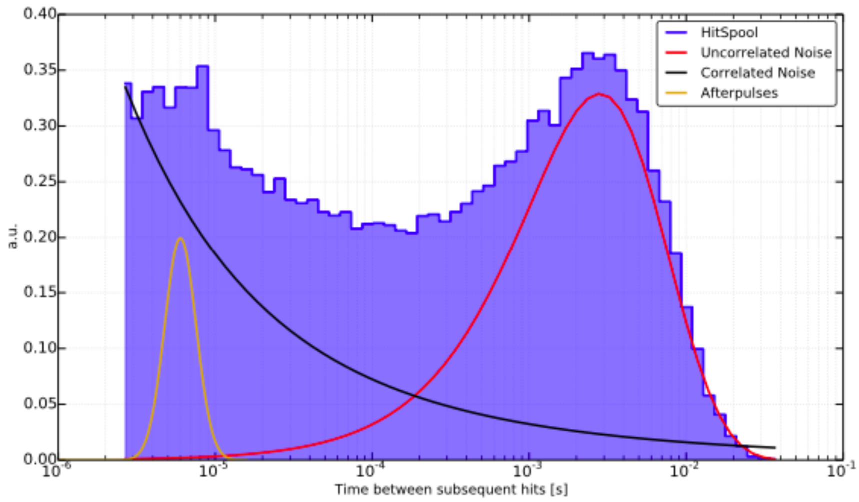


**Figure 4.3.** Histogram of time differences between successive hits from HitSpool data of DOM 15-27 (blue) on a logarithmic scale in order to visualize the different noise components (without prepulses which are comparatively insignificant). Credits: [100].

A part of the correlated noise originates from the radioactive decays, since daughter particles from each radioactive decay can interact within the glass, producing scintillation light. This scintillation light is produced in fast bursts and enters the PMT, hitting the photocathode to form a photoelectron signal. The number of hits in a burst is determined from a Poisson distribution with a constant mean determined for each DOM, and the time between subsequent hits is drawn from an empirically characterized log-normal distribution.

The Vuvuzela Noise Generator Module implements this model (see Ref. [118] for further details) and, for each DOM simulated, both the uncorrelated and correlated noise hits are produced.
The uncorrelated noise is simulated as a Poisson process with the number of hits $x$ which follows a Poissonian distribution

$$f_{\text{Uncorrelated}}(x) = \frac{(\lambda \Delta t)^x}{x!} \mathrm{e}^{(-\lambda \Delta t)}, \tag{4.1}$$

where $\lambda$ is the rate parameter associated with the process and $\Delta t$ is the duration of the simulated time window.
For thermal noise, the typical rate is on the order of $20$ Hz and varies with depth, while radioactivity occurs with a significantly higher rate of about $250$ Hz, which is constant.

Regarding the correlated noise, the number of scintillation photoelectrons $y$ is simulated again as a Poissonian distribution, but independent of the time window being simulated:

$$f_{\text{Correlated}}(y) = \frac{\eta^y}{y!} \mathrm{e}^{-\eta}, \tag{4.2}$$

where $\eta$ is an empirically fit constant value for each DOM.

Then, for each correlated hit, a standard normal distribution is sampled for a value $z$:

$$f_{\text{Correlated}}(z_i) = \frac{1}{\sqrt{2\pi}} \mathrm{e}^{-z_i^2}; \tag{4.3}$$

then the $z_i$ value is converted to a time $\delta t_i$ by translating to a log-normal distribution.

This noise model, which encodes the noise sources explained in Section 4.2.2, is used to elaborate the *ELOWEN* event selection.

### 4.2.5 Hit Cleaning

With *Hit Cleaning*, we refer to the use of several algorithms to remove noise hits and therefore increase the purity of the sample. Multiple strategies exist to identify pulses likely originating from detector noise; a brief overview of these methods, based on the discussion in Ref. [100], is presented below.

**HLC Cleaning**
Taking into account the local coincidence information, we can obtain very strict cleaning results; this type of cleaning is referred to as *HLC cleaning*.
In general, when a specific DOM records a light signal, it notifies the nearby DOMs. By selecting only pulses that result from DOMs satisfying the HLC criteria, the series can be cleaned of nearly all detector noise, although this implies a potentially significant amount of information loss about the event, since all SLC hits are removed.

**SeededRT Cleaning**
Instead of using only HLC hits, considering also SLC pulses enables us to identify potentially interesting pulses that fails the HLC condition.
To do this, the *SeededRT* algorithm can be used; it requires a seed, radius, and time to search for additional information in the event. Starting from selecting interesting pulses, such as a selection of the HLC ones, as a seed, then a sphere is drawn around each seeded DOM, and any nearby DOMs observing pulses within the sphere and time window are added to the output pulse series. The typical parameters used for DeepCore are a radius of $75$ m and a time window of $500$ ns.

**Dynamic Time Window Cleaning**
This is a specific kind of time window cleaning, used in *GRECO* selection; it is an algorithm that uses the maximum pulses density in time to find a likely interaction time for a physical event. Then the timing window, often consisting of a few hundred of ns, is placed around this time. In the following, we refer to is as DTW.

## 4.3 Event Selections in IceCube

To obtain the number of Dark Matter expected events in the detector, we need to define an Effective Area for this kind of events, which can be derived from the neutrino one; this computation is worked out in Chapter 5. Hence, it is useful to describe how the neutrino effective area is defined and then extract the DM one; we use two different effective areas, derived from two different event selections, according to the neutrinos' initial energy. To obtain these effective areas, some criteria must be used to select signals with respect to the high background rate.

In general, the effective area $A_{\text{eff}}$ is defined as [103]

$$A_{\text{eff}} = \frac{\text{Observed event rate}}{\text{Incoming flux}}, \tag{4.4}$$

reflecting the area of the detector, scaled down by the fraction of events triggering the detector over the total number of events incident on the detector. This effective area can only be obtained by means of simulation studies.

In the following, we briefly describe the selection criteria used to define the two neutrino effective areas of interest; in Section 4.3.1 we introduce *ELOWEN* effective area, a selection criterion optimized for GeV signals; then, in Section 4.3.2, we consider the *GRECO* effective area, optimized for higher energies, up to thousands of GeV.

### 4.3.1 Searches for GeV signals and *ELOWEN* effective area

The IceCube Neutrino Observatory was originally designed to observe TeV neutrinos; despite that, using DeepCore, we are able to extend the sensitivity to a larger energy range, down to the single GeV energy scale.
Below, we outline the main strategies used to select events in the few-GeV energy range. The content of this section is largely derived from Refs. [103] and [119], which constitute the main sources of the material presented.

Before these analyses, neutrino searches in IceCube were feasible in the MeV range using the Supernova Data Acquisition system[2] and above approximately 10 GeV for neutrino oscillation and atmospheric studies in DeepCore (for more details, see [82]). However, thanks to these studies, it is now possible to bridge the gap between these two energy ranges.

The main idea of *ELOWEN*, which stands for *Extremely LOW-ENergy interactions*, is to search for an increase in the rate of GeV-like events in IceCube during an astrophysical transient, such as a solar flare.

Furthermore, to understand the behavior of the selection to the different types of events, different simulation data sets have been used.
First, CORSIKA has been used to simulate extensive air shower events; this data set is used to study atmospheric muons traveling in the neighborhood of IceCube.
Similarly, to study the interactions of atmospheric and astrophysical neutrinos between $100$ MeV and a few hundreds GeV, the GENIE Neutrino Monte Carlo Generator

[2] IceCube can identify transient MeV neutrino sources, like supernovae, trhough a collective increase in the PMT trigger rates [120]. However it cannot resolve individual MeV neutrino signal, making it effective for transient signals like supernovae, it is not optimal for dark matter searches. Therefore, to reach our goal, it is better to consider event selection as a strategy to achieve a higher sensitivity

has been used. In addition, a Pure Noise events are produced by a noise event generator (see Section 4.2.4 for more details).
Finally, signal-like events are created using GENIE; several neutrino interaction processes are included in the simulation, as deep inelastic scattering, quasi-elastic scattering, resonant production, coherent scattering. Two different simulations sets have been used: *ELOWEN* for neutrinos between $500$ MeV and $1$ GeV and *lowen* for neutrinos between $1$ GeV and $5$ GeV.

These simulation sets have been used to model different signals occurring in the detector, to understand their main features and filter out uninteresting ones.
Among all possible signals, the physically relevant events for our purpose are cosmic neutrinos; these events are selected through three main steps, as described below.

### Removing High-Energy events

The first part of *ELOWEN* event selection is to reduce the amount of *high-energy* events[3] from the data sample.
The main difference between an event with arbitrarily high energy and a GeV neutrino interaction is the amount of light emitted in ice; therefore, to eliminate neutrinos with energy exceeding $5$ GeV, it is sufficient to impose strong constraints on the number of DOMs that provide a signal due to the interaction. Using available data streams, developed to tag specific kinds of events, we can extract the low-energy events.
Since, as mentioned before, the low-energy events activate a small number of DOMs and thus are not expected to pass any of the filters designed to tag high-energy interactions. Therefore, for an event to be included in the low-energy data sample, it must pass the *DeepCore filter* and fail all other filter conditions.
Considering a specific combination of filters, a substantial reduction in the number of atmospheric muons is possible. After applying this filter selection, the data rate decreases to approximately 15 Hz, compared to the original rate of around 1400 Hz. More than $98\%$ of simulated neutrino events, in both the lowen and *ELOWEN* simulations, pass this filter selection.
Moreover, to further decrease the data rate, the number of HLC hits in IceCube and DeepCore strings can be considered; this number is strongly limited for simulated low-energy signal events. On the contrary, background events from atmospheric muons and neutrinos are showing a large amount of HLC hits in the detector. This implies that, constraining the maximum amount of HLC hits allowed, it is possible to remove high-energy events from the sample. For this purpose, the request is to keep events that are fully contained in the DeepCore, selecting only events that have $0$ HLC hits in IceCube-without-DeepCore.
Finally, the number of causally connected hits within an event can also serve as an indicator of the amount of light produced in the detector due to a neutrino interaction. By applying the *SRTInIce* algorithm[4] and selecting hits that have at least one neighboring hit within a sphere of radius $R = 150$ m and a time window of $1\mu$s, the data rate

[3]With *high-energy* events we refer to neutrinos with an energy $> 5$ GeV; this is motivated by the expected energy range for the solar flare neutrinos, for which this event selection has been performed.

[4]This is an algorithm designed to select sets of hits most likely connected to the same physical interaction, and therefore unrelated with dark noise.

is reduced to 5.5 Hz while retaining $99\%$ of *ELOWEN* simulation events and more than $93\%$ of lowen simulation events.

### Minimizing the contribution of Pure Noise

The next step of the event selection is to differentiate low-energy neutrino interactions from detector noise.
As presented in Section 4.2.2, DOMs' noise can arise from numerous sources; all the contributions add together, resulting in a rate of $560$ Hz for IceCube DOMs and $780$ Hz for the DeepCore DOMs.
The algorithm to identify and eliminate this kind of noise has been developed based on triggers with few hits and no preferred direction, since DOMs' noise triggers occur with these characteristics.
In this frame, an event is classified as *physics* if it contains, during a certain time window, a minimum of pairs of hits with an effective speed contained in a defined interval, pointing in excess towards a certain direction; otherwise the event is classified as *noise*.
This algorithm was originally optimized to differentiate noise from $10-100$ GeV neutrino interactions, and then it has been re-optimized to be effective for lower-energy events.
Using this noise filter, called *NoiseEngine*, the data rate is about $0.2$Hz, while the noise rate is of the order of $0.12$Hz; therefore, more than $55\%$ of *ELOWEN* simulation events survive these cuts.

### Increasing the Purity

Up to now, most of the pure noise events have been removed, but to increase the purity of the sample, the remaining high-energy events need to be removed. To achieve this goal, the following selection criteria are applied:

- ***Charge distribution***: it is focused on the removal of the remaining muons. Since the energy loss of a muon can be detected as soon as it enters the detector, while a neutrino interaction deposits most of its energy close to the interaction point, we can use this property to discriminate between the two different particles. We consider the first $600$ ns after the first HLC hit in DeepCore and integrate the charge in DeepCore DOMs; this time window has been optimized to maximize the signal-to-background ratio. Then we define the Q-ratio as the fraction of this integrated charge and the total charge in the event. Selecting only events with Q-ratio higher than $0.26$, the data rate is reduced down to $0.08$ Hz, while keeping at this stage more than $50\%$ of *ELOWEN*;

- ***Depth of the interaction***: this step aims to reduce the contamination of low-energy down-going muons. Low-energy atmospheric muons leave more energy in the top of the detector rather than in deeper DOMs, while we expect that most of neutrinos signal events start in the dense core of the detector. Limiting the depth of the first HLC hit in DeepCore, by selecting events with a first DeepCore HLC hit between $[-2453, -2158]$m, reduces the data rate to $0.055$ Hz

(2012), while preserving more than $40\%$ of the *ELOWEN* events compared to the initial number;

- ***Centroid of the event***: another aspect that can be considered is the causality between hits within the same event. *ELOWEN* events must be of low energy, this implies that the DOMs have to record events that are close to each other, both in distance and time. Hence, we can cut on the distance and time delay between the first and the second HLC hits in the DeepCore; asking for a distance between these two hits smaller than $70$m and for a time delay not more than $50$ns, we can reach a data rate of $0.030$Hz and about $40\%$ of *ELOWEN* events pass the selection so far;

- ***Total Charge***: considering the deposited charge, we can remove the remaining events which have a too high deposited charge to be created by low-energy neutrino interactions. Selecting events with a charge inferior to $60$ photoelectrons, the data rate is reduced to $0.022$Hz, and more than $35\%$ of the *ELOWEN* events survive at this point;

- ***HLC Hits***: Finally, we have to remove the events with a relatively high number of HLC hits in DeepCore, compared to the expectations for GeV neutrino interactions. Keeping the events that have less than $10$ HLC hits in the DeepCore, the data rate becomes $0.018$ Hz.

Applying all these criteria, more than $35\%$ of the *ELOWEN* events survive this selection.

### Event Characteristics at the Final Level

Once defined all the selections applied to IceCube data to constitute a GeV-like sample, we can now describe the event characteristics at the final level.
In Figure 4.4 a summary table of the rate of different sets at the final level is presented.

| **Sets** | | **Rate** |
|---|---|---|
| Data | 2011 | $0.025 \pm 0.003$ Hz |
| | 2012 | $0.021 \pm 0.003$ Hz |
| | 2013 | $0.020 \pm 0.003$ Hz |
| | 2014 | $0.022 \pm 0.003$ Hz |
| | 2015 | $0.021 \pm 0.003$ Hz |
| | 2017 | $0.019 \pm 0.003$ Hz |
| Pure noise | | 0.018 Hz |
| Corsika | | $< 0.005$ Hz (Hoerandel) |
| GENIE | $\nu_e$ | 0.0003 Hz |
| | $\nu_\mu$ | 0.0008 Hz |

**Figure 4.4.** Rate of different simulation and data sets at final level of *ELOWEN* event selection. Credits: [103]

Performing a qualitative estimation of the data composition at the final level, we see that there are potentially two dominant components: atmospheric muons and events due to pure noise trigger.

Then, defining the passing fraction ($\mathcal{P}$) as the number of events at the final level over the number of events after triggering, we get, for the simulated electrons-, muon-, tau- neutrinos, the following passing fractions [103]:

$$\mathcal{P}(\nu_e) \sim 46\%\,, \qquad \mathcal{P}(\nu_\mu) \sim 44\%\,, \qquad \mathcal{P}(\nu_\tau) \sim 40\%. \tag{4.5}$$

In general this passing fraction depends by neutrinos initial energy; these values have been computed for a neutrino energy $E_\nu \in [1, 5]$ GeV, for which values this event selection is optimized.

### 4.3.2 Searches for hundreds-GeV signals and *GRECO* effective area

The GeV Reconstructed Events with Containment for Oscillations (*GRECO*) event selection was originally developed for tau appearance oscillation analysis; this data sample contains events in the energy range $\sim 10$GeV $- 1000$GeV, detected mainly by DeepCore.

In the following, the cut levels of *GRECO* selection are shown; these cuts are designed to remove atmospheric muons and accidental triggers maintaining neutrino events. The content of this section is largely derived from Refs. [121], [122], and [123], which constitute the main sources of the presented material.
As *ELOWEN*, *GRECO* is an event selection that results from applying cuts at seven different levels.
The starting point is that muons dominate the events passing the SMT3 trigger in the DeepCore, with a rate of $280$ Hz compared to a neutrino rate of about $4$ mHz. Thanks to the *GRECO* event selection, the muon rate is reduced to around $0.07$ mHz, preserving around $0.7$ mHz of atmospheric neutrino events.

#### Level 1: The DeepCoreFilter

The first step in any selection process is to design a trigger that maximizes the acceptance of the expected physical signal.
After triggering, a filter can be applied with the purpose of removing the collected background; in the case of *GRECO* selection the filter considered is the *DeepCoreFilter*. This filter analyzes the first pulses detected on each DOM, identified through SeededRT cleaning, and categorizes them as either 'veto' or 'fiducial' pulses. To further reduce noise contributions, it calculates the mean time of the first pulses across all DOMs and removes any hit DOM whose first pulse occurs more than one standard deviation away from this mean.
This algorithm reduces the atmospheric muon background from $280$ Hz to approximately $17$ Hz while retaining $99.4\%$ of neutrino events which begin in the DeepCore.

### Level 2: Hit Cleaning algorithms

After the application of the *DeepCoreFilter*, other *Hit Cleaning* algorithms are used. As explained in Section 4.2.5, these are algorithms developed to remove the noise hits and increase the sample's purity.
This processing stage does not remove events from the selection, therefore is not interesting for our discussion.

### Level 3: Low-Energy Cuts in the DeepCore

These cuts are standardized and used in all DeepCore oscillation analyses.
After Level 1 cuts, approximately half of the remaining rate consists of muons; also accidental triggers due to random detector noise are an important contribution, due to the low trigger threshold used in DeepCore; hence, the Level 3 cuts are introduced to remove these two contributions.

To **reject accidental hits**, events are required to have at least 3 pulses and a total charge of at least 3 photoelectrons in a $250$ ns DTW cleaned pulse series in the DeepCoreFiducial region. In addition, *NoiseEnigine* algorithm is used to identify accidental triggers, using the relative direction between each pair of hits to search for the directionality of the event. Rejecting events with fewer than three hit pairs pointing in the same direction, more than $96\%$ of accidental triggers are removed from the analysis.

Now we have to look at the **rejection of Atmospheric Muon Events**; at this level, muons are generally bright enough to be identified by hits in the veto region (the outer part of the detector). Since neutrino candidates of interest in *GRECO* sample have energies smaller than $50$ GeV, no light emission is expected in the veto region due to these neutrinos. Hence, to identify muons, the following cuts are used:

- ***First Hit Z Position***: most muons will leave hits in the upper part of the detector since their tracks are primarily steeply inclined, while neutrinos of interest will primarily emit light within the DeepCore fiducial volume, leading to little or missing light emission in the top half of the detector. Considering this difference, events with a first hit above $Z = -120$ m are removed;

- ***NAbove200***: this variable measures the integrated charge occurring before the SMT3 trigger, above a depth of $-200$ m; the event is removed from the sample if more than 12 DOMs are hit above this depth;

- ***RTVeto***: this step aims to remove clusters of hits due to muons. Using, as before, the SeededRT algorithm, we can identify the largest cluster of pulses in the veto region, and therefore considering the number of hits in this cluster we can recognize atmospheric muon events. For this step we consider a RTVeto algorithm with a radius of $250$ m and a time window of $1000$ ns for both DeepCore and InIce DOMs. This cut is used in combination with the total amount observed in the DeepCore fiducial region, removing each event with a cluster of $4$ or more hit DOMs in the InIce detector;

- ***C2QR6***: another aspect to be considered is that atmospheric muons tend to leave long tracks and take $\mathcal{O}(3\mu\mathrm{s})$ to cross the detector, while neutrino events produce small light patterns due to the low energies involved, with a quick deposition of light; therefore, to reject muon events, the difference in the light emission profile can be considered. Defining the *charge ratio in 600 ns* (QR6) as the ratio of charge observed in the first $600$ ns and the total amount of observed charge, we can discriminate between muons (with QR6$\rightarrow 0$ since they deposit light over a longer timescale) and neutrinos (with a quicker deposition of light, hence QR6$\rightarrow 0$). Finally, in order to reduce the possibility of an erroneous definition of the time window, the first two hits can be neglected, determining the *cleaned charge ratio in 600 ns* (C2QR6).

After the application of the Level 3 cuts, the atmospheric muons are reduced of about one order of magnitude, and the accidental trigger events decrease by more than $96\%$.

#### Level 4: Low-Energy Cuts in *GRECO*

This Level is very similar to the previous one, and it also is divided into two kinds of cuts.
To **reject Accidental Events**, a static time window cleaning is applied with a range of $-3500ns \leq t \leq 4000ns$ for hits in the DeepCore fiducial volume; then a dynamic time window cleaning, with a window of $200$ ns, is applied and finally any events with less than three hits are removed.

At this level, to **reject atmospheric muon events**, a stricter hit cleaning algorithm is used to identify the ones missed at Level 3; to do this, thee following cuts are applied:

- ***First Hit Z Position***, ***NAbove200***, ***C2QR6***: applied as at Level 3;

- ***Tensor of Inertia***: many neutrinos with energies in the range $1-100$ GeV have a compact hit pattern in the DeepCore, while muons have a more elongated pattern. This hit topologies' difference can be measured with the *Tensor of Inertia eigenvalue ratio*, defined as the tensor of inertia from mechanics, with the mass replaced by the measured charge, $I_X = \sum_{i=0}^{\text{nhits}}(y_i^2 + z_i^2)q_i$ and similarly for $I_Y$ and $I_Z$. The eigenvalue ratio is defined as

$$e = \frac{max(I_j)}{I_X + I_Y + I_Z}. \tag{4.6}$$

  Muon-like events, with very track-like signal, have $e \sim 0$, while cascade-like events have $e \sim \frac{1}{3}$;

- ***Linefit Speed***: this cut takes into account the average velocity of the event ($\bar{v}$) to reject muon events. This is related to the fact that in cascade-like events photons have no average preferred direction, hence $\bar{v} \sim 0$, while relativistic atmospheric muons have a preferred direction and therefore they travel through the detector with a speed $c_{\text{ice}} = 0.3$ m/ns.

After these cuts, the atmospheric muon rate is reduced to $50$ Hz; nevertheless the number of accidental triggers, even if it is reduced in this level, is still larger than the number of neutrinos expected; therefore further cuts are necessary.

**Level 5**

At this level, to **reject accidental events** the STW+SRT pulse series is used to fit several parameters, as the interactions' position and time and the direction of a muon track; therefore, an implicit requirement on the number of hit DOMs arises, requiring at least 6 hit DOMs in the hit series.

Then, several cuts are included to **reject atmospheric muon events**:

- ***Time to*** $75\%$ ***Charge***: this variable is designed to look at the hit distribution in time and is defined as the amount of time required to record $75\%$ of the total charge, measured from the start of the event. To discriminate between muons and neutrinos we have to consider that neutrino events deposit energy quickly, due to the low energies of the sample of interest, while muon events take more time due to the long travel time through the detector;

- ***Veto Identified Causal Hits***: this is an algorithm developed to search for hits that are causally connected to the trigger; the ones no causally connected are removed, and also hits which occur too far away from DeepCore;

- ***First Hit*** $\rho$: defining the radial distance from the center of the DeepCore $\rho$, is possible to discriminate between atmospheric muons entering DeepCore, which are more likely to be found at larger values of $\rho$, while neutrinos are more likely to be found within the DeepCore, therefore at $\rho \leq 125$ m;

- ***Quartiles CoG***: since for atmospheric muon events the apparent distance traveled is expected to be larger than for low energy neutrino events, also this variable can be used to discriminate between different types of particles;

- ***Z-travel***: because atmospheric muons cannot penetrate the Earth, no background muon events are upgoing; therefore the distance and direction of travel can be a useful variable to identify atmospheric muon events. Considering the charge weighted average distance in the Z direction of pulses, atmospheric downgoing muons have a negative z-traveled distance, while for neutrinos this may be positive or negative;

- ***SPE Zenith***: this is the first likelihood reconstruction used in *GRECO* event selection; it includes a model of the effect of scattering in the ice based on the time of first observed pulse in each DOM. The likelihood is maximized to obtain the best-fit values for the position, time, and direction of the track. This is referred to as *Single PhotoElectron* (SPE) fit, because this construction assumes that only one photon is received per DOM. The zenith angle returned by this fit is considered to separate between muons and neutrinos since muons are primarily down-going events.

After the application of these cuts, the event rates for the atmospheric muons are a factor of $3\times$ larger than the neutrino flux and the accidental triggers rate is comparable to the muons one.

### Level 6

At this level, two cuts are applied both for the removal of the remaining accidental triggers and for the reduction the muon background rate.
To **reject accidental events**, the following cuts are applied:

- ***Fill-Ratio***: this variable is typically used in the search for high-energy cascades, by quantifying the compactness of hits within an event. Defining a reconstructed vertex as the first hit position in DeepCore within a STW+SRT cleaned series and a radius ($r$), computed using the mean distance from the vertex, one can build an algorithm which identifies all DOMs contained in the sphere centred in the vertex and with radius $r$. Finally, the fill-ratio value $f$ is defined as the ratio of contained DOMs observing a pulse to the total number of contained DOMs. In a cascade, we expect the resulting hit distribution to be approximately spherically symmetric, with $f \sim 1.0$, while in a track-like event we get a smaller value od $f$. This variable provides a good separation between neutrino events and accidental triggers, while it has no significant separating power between neutrinos and atmospheric muons;

- ***Number of Hit DOMs***: events with fewer than $8$ hit DOMs in the STW+SRT cleaned DeepCore pulse series are removed. This is performed in order to prepare the sample for the following level, but it also removes a significant number of accidental triggers from the selection.

Then, to **reject atmospheric muon events**, the following two cuts are performed:

- ***CorridorCut***: since, in the past, muons were discovered to be leaking into the DeepCore fiducial volume along corridors[5], a cut was developed to look along pre-defined corridors. A cut limiting the number of discovered corridor hits to zero would result in a significant loss of signal events, due to the effects of random detector noise, therefore one hit is allowed;

- ***FiniteReco Starting Containment***: using the SPE reconstruction from Level 5, we can obtain the starting position of the resulting reconstructed particle and therefore its interaction point. If an event begins outside of the DeepCore fiducial volume, it is likely to contain a muon and hence is removed from the sample.

After the application of these cuts, the sample is dominated by neutrino events, the expected muon rate from CORSIKA simulation makes up $22\%$ of the total sample and the rate of random detector noise events is $5\%$ of the total.

[5]With *corridors* we refer to lines connecting the inner part of the detector to the outer edge without crossing any strings

### Level 7: the Final Level

This is the most computationally expensive stage of the selection; it employs the *Pegleg* reconstruction to further reduce the atmospheric muon rates, based on the position of events in the detector. This reconstruction uses a hybrid cascade+muon hypotesis in order to consider additional constraints on the containment of the starting vertices. Similarly to the previous stage, events at the top and near the edge of DeepCore are more likely to be muons; an additional cut is applied at the bottom of the detector in order to limit the effect of observed discrepancies between data and simulation.
At this level, cuts are also applied to the average reconstructed energy per hit DOM and the scatter in the timing distribution of hits: a cut removing events with more than $3$ GeV/DOM is applied only to events with fewer than $14$ hits, limiting the impact on the neutrino signal events.
Finally, the scatter in hit times is used to identify accidental events, which are not expected to produce hits correlated across DOMs; this cut removes events where the standard deviation of the hit times is larger than $800$ ns and is also applied for events with fewer than $14$ hits.

### Properties of *GRECO* Event Selection

In Figure 4.5, the event rates for each simulation sample are shown. Although atmospheric muons dominate the initial sample, their contribution is significantly reduced after applying the seven levels of the *GRECO* selection. At the same time, the neutrino components are largely preserved.

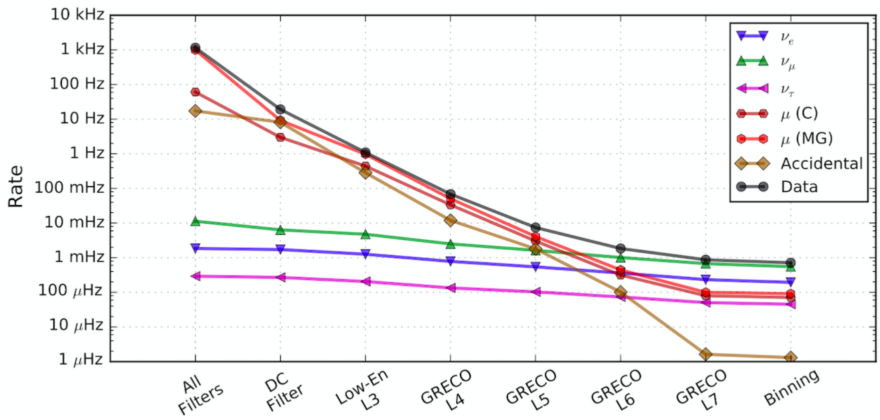


**Figure 4.5.** Rates at each cut level in the GRECO event selection algorithm. The muon and accidental trigger rates decrease, after the DeepCoreFilter, from approximately 18 Hz to less than 1 mHz at the Final Level. All values are obtained from simulations. Credits: [121].

# CHAPTER 5

# New IceCube Sensitivities to sub-GeV Dark Matter

In the previous sections, I presented an overview of the evidence and properties of Dark Matter, as well as the methods for neutrino detection in neutrino telescopes.
Subsequently, the *ELOWEN* and *GRECO* selection criteria, those used in my study, were introduced and discussed.
All these elements converge in my analysis, which leads to the derivation of sensitivities to sub-GeV Dark Matter via Direct Detection, for the first time at the IceCube Neutrino Telescope.

This Chapter is organized as follows: Section 5.1 presents the theoretical framework, including the derivation of the differential cross-sections for interactions between Standard Model particles and Dark Matter particles. In Section 5.2, I compute the expected signal at IceCube, first by evaluating the Dark Matter flux at Earth and then the resulting number of Dark Matter events expected at IceCube. Section 5.3 introduces the Test Statistic used in my analysis to discriminate between the background-only hypothesis and the background-plus-signal hypothesis. Finally, Section 5.4 presents the results of the analysis.

## 5.1 Theoretical Framework: Hadrophilic Dark Matter

We define the Dark Matter particle as a Dirac fermion, $\chi$, which is a singlet under the SM gauge group $SU(3)_C \times SU(2)_L \times U(1)_Y$, and has mass $m_\chi$.
In addition to the SM matter content, we introduce the DM particle and a new mediator responsible for the interaction between DM and SM particles.
Two scenarios are considered: a scalar-mediated interaction, involving a new scalar field $\phi$ with mass $m_\phi$, and a pseudoscalar-mediated interaction, involving a new pseudoscalar field $a$ with mass $m_a$.
In this framework, we focus on Hadrophilic Dark Matter, DM particles that couple primarily to hadrons. This property makes it particularly suitable for detection in Direct Detection experiments, where the target materials are composed mainly of nucleons.

At a first stage, the interaction between DM and SM quarks is described by the following Lagrangians [6]:

$$\begin{aligned}\mathcal{L}_\phi &= g_{\chi\phi}\bar{\chi}\chi\phi + g_{q\phi}\bar{q}q\phi\,,\\ \mathcal{L}_a &= g_{\chi a}\bar{\chi}i\gamma_5\chi a + g_{qa}\bar{q}i\gamma_5 qa\,,\end{aligned} \tag{5.1}$$

where $q$ runs over the quarks; this is the Relativistic Lagrangian, valid at energies larger than about a GeV (but smaller than the electroweak scale).

### 5.1.1 Dark Matter Effective Coupling with Nucleons

Since the energies involved in DM scattering with ordinary matter are very low, the relevant degrees of freedom are nucleons and nuclei rather than quarks ([8], [124]). As a consequence, in our study, DM–nucleon interactions are described using a non-relativistic effective Lagrangian.
This framework is broadly used in the literature, including in Ref. [6], where a similar analysis was performed in the context of the Super-Kamiokande experiment; in this work, we adapt and extend that approach to the IceCube detector.

To derive these non-relativistic interaction terms, we follow the methodology presented in Refs. [8] and [124].

#### Scalar Mediator case

In this paragraph, we derive the Non Relativistic Lagrangian (NR) for the scalar mediator case. To achieve this goal, we consider the matching from quark level to nucleon level at the lowest order, without including Next-to-Leading Orders, as previously done in Ref. [125]. The Lagrangian at the quark level is given by $\mathcal{L}_\phi$, expressed in Equation (5.1), while the scalar-nucleon interaction can be written as

$$\begin{aligned}\mathcal{L}_{\mathcal{N}\phi} &= \langle\chi N|\,\mathcal{L}_\phi\,|\chi N\rangle\,\bar{\chi}\chi\bar{N}N\\ &= \langle\chi N|\,g_{\chi\phi}\bar{\chi}\chi\phi + g_{q\phi}\bar{q}q\phi\,|\chi N\rangle\,\bar{\chi}\chi\bar{N}N\\ &= \langle\chi N|\,g_{\chi\phi}\bar{\chi}\chi + g_{q\phi}\bar{q}q\,|\chi N\rangle\,\phi\bar{\chi}\chi\bar{N}N\,,\end{aligned} \tag{5.2}$$

where we have used the fact that $\phi$ is a scalar and is independent of the states $|N\rangle$ and $|\chi\rangle$.
Considering the direct product between the nucleon and DM states $|\chi N\rangle = |\chi\rangle\otimes|N\rangle$, we have that

- the operator $g_{\chi\phi}\bar{\chi}\chi$ acts only on $|\chi\rangle$ states,
- the operator $g_{q\phi}\bar{q}q$ acts only on $|N\rangle$ states;

this implies that in the computation of the matrix element, we have a factorization.
Evaluating the matrix element, we obtain

$$\begin{aligned}\mathcal{M} &= \langle\chi|\,g_{\chi\phi}\bar{\chi}\chi\,|\chi\rangle\,\langle N|\,g_{q\phi}\bar{q}q\,|N\rangle\\ &= g_{\chi\phi}g_{q\phi}\,\langle\chi|\,\bar{\chi}\chi\,|\chi\rangle\,\langle N|\,\bar{q}q\,|N\rangle\ ,\end{aligned} \tag{5.3}$$

where $N$ is the nucleon spinor wave-function, $m_N$ and $m_q$ are, respectively, the nucleon's and quark's masses.

Finally, we define the ***form factor at zero momentum transferred*** $f_q^N$, which is constant, and the ***scalar nucleon form factor*** $G$, which incorporates the finite size of the nucleon [6], as

$$f_q^{(N)} \equiv \frac{\langle N| \, m_q \bar{q} q \, |N\rangle}{2m_N^2}, \qquad G(q^2) = \frac{1}{(1+\frac{q^2}{\Lambda^2})^2}\,; \tag{5.4}$$

these parameters are taken from Ref. [6], where they are given as $2m_N \cdot f_u^N = 1.99 \times 10^{-2}$, $2m_N \cdot f_d^N = 4.31 \times 10^{-2}$, $\Lambda_{\mathrm{H}} = 770$MeV and $\Lambda_{\mathrm{He}} = 410$MeV.

In this way, the matrix element in Equation (5.3) becomes

$$\mathcal{M} = g_{\chi\phi} g_{q\phi} \frac{m_N}{m_q} f_q^N G(-t) 2m_\chi 2m_N\,; \tag{5.5}$$

where $t = (p_f - p_i)^2$ is the Mandelstam variable. In the derivation, we have considered that $\langle\chi| \, \bar{\chi}\chi \, |\chi\rangle \sim 2m_\chi$ in the non-relativistic limit, as derived in Appendix B.

By substituting these results in Equation (5.2), we can rewrite the NR Lagrangian for the scalar-mediated interaction as

$$\mathcal{L}_{N\phi} = \; g_{\chi\phi} g_{q\phi} \frac{m_N}{m_q} f_q^N G(-t) 2m_\chi 2m_N \phi \bar{\chi}\chi \bar{N} N \tag{5.6}$$

As presented in Ref. [6], we can consider the following assumptions:

- the nuclei form factor is given by $n_A F_A(q^2)$, with $F_A(q^2) = G_A(q^2)$. We $n_A$ as the number of nucleons inside the nuclei $A$ and $G_A$ as the nucleon form factor. In this study, for DM-CRs interactions considered in the computation of the flux, we consider only the scattering with protons and Helium, assuming that all the DM components upscattered by other CRs elements are negligible. Furthermore, regarding the DM interaction with the particles of the detector, we consider as relevant degrees of freedom the target nucleons rather than nuclei, since the energy transferred in the interaction is large enough that the DM particles resolve the constituents of the nuclei;
- we assume an isoscalar coupling for up and down quarks $g_{u\phi} = g_{d\phi}$;
- we assume the coupling to all other quarks vanishes.

In conclusion, we can obtain the final formulation of the NR Lagrangian as

$$\boxed{\mathcal{L}_{N\phi} = \; g_{\chi\phi} g_{N\phi} n_A F_A(-t) 2m_\chi 2m_N \phi \bar{\chi}\chi \bar{N} N} \tag{5.7}$$

where the nucleon-scalar coupling, considering the isoscalar coupling $g_{u\phi} = g_{d\phi} = g_\phi$ and all the other couplings vanishing, is given by

$$g_{N\phi} = g_{u\phi}\left(\frac{m_N}{m_u} f_u^N + \frac{m_N}{m_d} f_d^N\right). \tag{5.8}$$

At tree level, the leading non-relativistic operator in momentum space, induced by $\mathcal{L}_\phi$ is the identity $\mathbb{1}$, so detection techniques which search for scalar-mediated DM-SM interactions give **spin-independent searches**.

## Pseudoscalar Mediator case

As in the scalar case, we get the NR limit of the pseudoscalar Lagrangian at the quark level, expressed in Equation (5.1), considering

$$\begin{aligned}\mathcal{L}_{Na} &= \langle\chi N|\,\mathcal{L}_a\,|\chi N\rangle\,\bar{\chi}\chi\bar{N}N \\ &= \langle\chi N|\,g_{\chi a}\bar{\chi}i\gamma_5\chi a + g_{qa}\bar{q}i\gamma_5 q a\,|\chi N\rangle\,\bar{\chi}\chi\bar{N}N \\ &= \langle\chi|\,g_{\chi a}\bar{\chi}i\gamma_5\chi\,|\chi\rangle\,\langle N|\,g_{qa}\bar{q}i\gamma_5 q\,|N\rangle\,a\bar{\chi}\chi\bar{N}N\,;\end{aligned} \tag{5.9}$$

the latter derivation is obtained considering that the pseudoscalar mediator $a$ does not depend on the nucleon state.
Evaluating the matrix element, we obtain

$$\begin{aligned}\mathcal{M} &= \langle\chi|\,g_{\chi a}\bar{\chi}i\gamma_5\chi\,|\chi\rangle\,\langle N|\,g_{qa}\bar{q}i\gamma_5 q\,|N\rangle \\ &= g_{\chi a}g_{qa}\,\langle\chi|\,\bar{\chi}i\gamma_5\chi\,|\chi\rangle\,\langle N|\,\bar{q}i\gamma_5 q\,|N\rangle\;.\end{aligned} \tag{5.10}$$

In this case, the ***form factor at zero momentum transferred*** $h_q$ is defined as

$$h_q = \frac{\langle N|\,m_q\bar{q}i\gamma_5 q\,|N\rangle}{2m_N^2}\,. \tag{5.11}$$

The ***nucleon form factor*** $G_a^q$ is given by the partially conserved axial current relation [6] as

$$G_a^q(-t) = G_A(-t) + \frac{t}{4m_N^2}G_p^q(-t) - 2\epsilon_q G_G(-t), \tag{5.12}$$

where the axial vector form factor $G_A$, and the pseudoscalar form factor $G_P^q$ are given by

$$G_A(q^2) = \frac{1}{(1+\frac{q^2}{\Lambda_a^2})^2} \qquad \text{and} \qquad G_P^q(q^2) = G_A(q^2)\frac{C_q}{q^2+M_q^2}\,. \tag{5.13}$$

Finally, we neglect the anomaly form factor $G_G$, since it has little significance on the final result.
As for the scalar case, the form factor at zero momentum transfer and the parameters needed to define the nucleon form factor are obtained from Ref. [6]; their values are: $2m_N \cdot h_{u+d} = 0.45$, $\Lambda_a = 1.32$ GeV, $C_{u+d} = 0.90$ GeV$^2$ and $M_{u+d} = 0.33$ GeV.

Therefore the matrix element in Equation (5.10) becomes

$$\mathcal{M} = g_{\chi a}g_{qa}\frac{2m_N^2}{m_q}h_q G_a^q(-t)\frac{(\vec{s}_\chi\cdot\vec{p})}{2m_\chi}\frac{(\vec{s}_N\cdot\vec{p})}{2m_N}\,; \tag{5.14}$$

in this derivation, we have considered that $\langle N|\,\frac{\vec{\sigma}\cdot\vec{p}}{2m}\,|N\rangle \sim \frac{\vec{s}\cdot\vec{p}}{2m}$ in the non-relativistic limit, as derived in Appendix B.

Then our NR Lagrangian becomes

$$\mathcal{L}_{Na} = g_{\chi a}g_{qa}\frac{2m_N^2}{m_q}h_q G_a^q(-t)\frac{(\vec{s}_\chi\cdot\vec{p})}{2m_\chi}\frac{(\vec{s}_N\cdot\vec{p})}{2m_N}a\bar{\chi}\chi\bar{N}N\,. \tag{5.15}$$

In this study, we consider, as in the scalar mediator case, the isoscalar coupling $g_{ua} = g_{da} = g_a$ and all the other couplings vanishing; defying the nucleon form factor as $F_a(q^2) = G_a^{u+d}(q^2)$[1] we get that the nucleon-pseudoscalar coupling is given by

$$g_{Na} = g_a \frac{2m_N}{m_u + m_d} h_{u+d}. \tag{5.16}$$

Finally, the Non-Relativistic Lagrangian for the pseudoscalar mediator case becomes

$$\boxed{\mathcal{L}_{Na} = g_{\chi a} g_{Na} F_a(-t) \frac{(\vec{s}_\chi \cdot \vec{p})}{2m_\chi} \frac{(\vec{s}_N \cdot \vec{p})}{2m_N} 2m_N a \bar{\chi}\chi \bar{N} N} \tag{5.17}$$

At tree level, the leading non-relativistic operator in momentum space, induced by $\mathcal{L}_a$ is $(\vec{s}_\chi \cdot \vec{p})(\vec{s}_N \cdot \vec{p})$. This implies that detection techniques which search for pseudoscalar-mediated DM-SM interactions give **spin-dependent searches**. Notice that, since Helium does not have a net spin, only the scattering with CRs Hydrogen is considered for the DM upscattered flux given by a pseudoscalar mediated DM-CRs interaction.

### 5.1.2 Determination of the Differential cross-section

To obtain the expected signal at the detector, we need to compute the differential cross section for DM–SM interactions. The full derivation is presented in Appendix C; here, we summarize the key results.

The DM–SM interactions considered are two-to-two scattering processes, where particle 1 (mass $m_1$) is initially at rest, and particle 2 (mass $m_2$) is incoming. This configuration is illustrated in Figure 5.1. The four-momenta of the two particles are, respectively,

$$\begin{aligned} p_1 &= (m_1, \vec{0}) \,, \\ p_2 &= (E_2, \vec{p}_2), \quad m_2^2 = E_2^2 - |\vec{p}_2|^2 \,. \end{aligned} \tag{5.18}$$

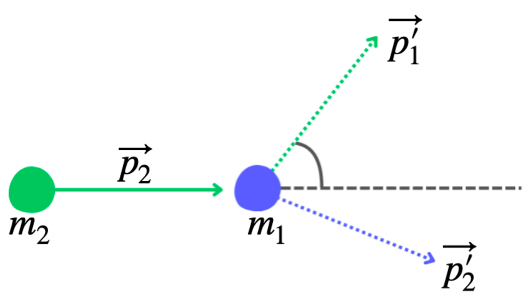


**Figure 5.1.** Diagram of a two-to-two scattering process involving a particle initially at rest and an incoming particle.

[1] In the pseudoscalar mediator case, $n_A = 1$ because we consider only DM scattering on Hydrogen, due to the spin configuration of Helium.

For the DM-SM interaction mediated by a scalar particle, the final form for the differential cross-section in terms of the kinetic energy is

$$\frac{d\sigma_\phi}{dK_f} = \frac{1}{K_{\text{max}}} \frac{g_{\chi\phi}^2 g_{N\phi}^2}{16\pi s} \frac{(4m_\chi^2 - t)(4m_A^2 - t)}{(t - m_\phi^2)^2} n_A^2 F_A^2(-t)\Theta(K_{\text{max}} - K_f) \tag{5.19}$$

Similarly, for a pseudoscalar mediator, the expression becomes:

$$\frac{d\sigma_a}{dK_f} = \frac{1}{K_{max}} \frac{g_{\chi a}^2 g_{Na}^2}{16\pi s} \frac{t^2}{(m_a^2 - t)^2} F_a^2(-t)\Theta(K_{\text{max}} - K_f) \tag{5.20}$$

## 5.2 Expected Signal at the Detector

The goal of this Section is to determine the expected number of DM events at IceCube. This quantity can be derived from the interaction cross-sections obtained in the previous section.
In particular, this study focuses on hadrophilic light DM that is upscattered by Cosmic Rays. Therefore, the events detected at IceCube result from a two-step interaction process.

First, DM particles from the Galactic halo, which are non-relativistic and initially considered at rest due to their much lower velocity compared to CRs, are assumed to interact with incoming CRs. A portion of the CRs' kinetic energy is transferred to the DM, producing an upscattered component of the DM flux. This upscattered flux is computed in Section 5.2.1.
This flux, which peaks in the GeV energy range, can then reach IceCube, interact with protons in the detector, and be detected. The number of events induced at IceCube by this interaction is derived from the DM interaction cross-section and the detector's effective area, as described in Section 5.2.2.
Additionally, for a more precise analysis, one can also consider that the upscattered DM flux may traverse different path lengths through the Earth's rock or Antarctic ice depending on the arrival direction. How the flux is attenuated as a function of its arrival direction is discussed in Section 5.2.3.

The DM candidate considered in this analysis is the same as the one introduced in Ref. [6]. While the upscattered DM flux is computed following a similar approach, the expected number of events is evaluated here differently, using the IceCube detector's effective area.

### 5.2.1 Dark Matter Upscattered Flux

High-energy Cosmic Rays, as already introduced in Section 3.2, are known to be present in our Galaxy. As input for our analysis, we adopt the CRs fluxes derived in Ref. [97], from which we extract the contributions from Hydrogen and Helium. These CRs fluxes are reported in Figure 5.2.

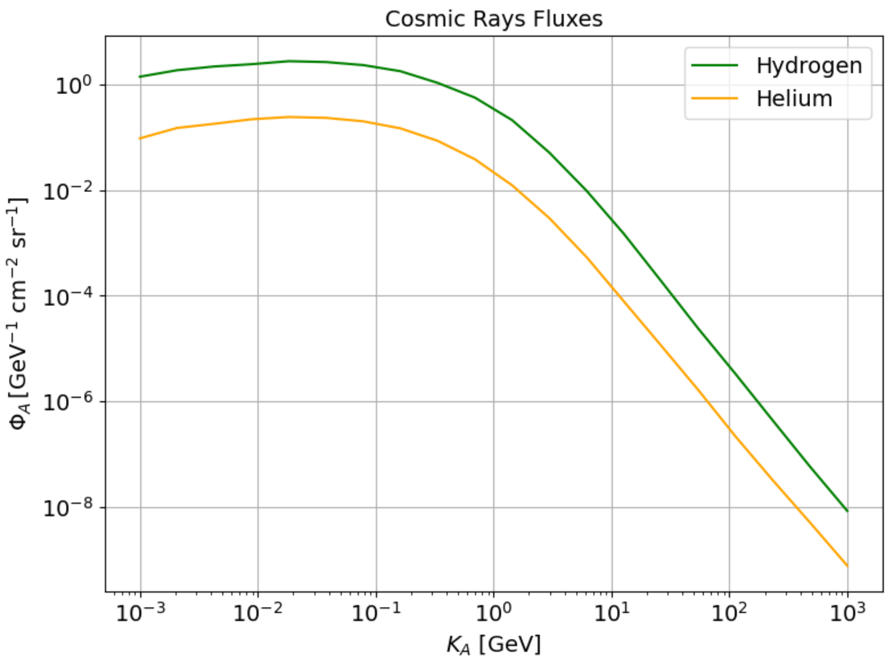


**Figure 5.2.** Cosmic Rays fluxes used as input of this analysis; in green we present the Hydrogen flux, while in orange the Helium one. The fluxes shown in this plot were reproduced from [97].

Furthermore, since we consider interactions between CRs and Galactic DM, it is necessary to introduce the standard halo DM flux. As mentioned previously, the derivation of the upscattered DM flux follows the approach outlined in Ref. [6].
The Galactic DM Halo is given by

$$\phi_\chi^{\text{halo}} = \frac{\rho_\odot}{m_\chi^2} c^2 f(v(K_\chi)), \tag{5.21}$$

where $c$ is the speed of light and $v(K_\chi) = \sqrt{\frac{2K_\chi}{m_\chi}}$; the speed distribution and the normalization factor are rispectively

$$\begin{aligned} f(v) &= \frac{1}{N}\sqrt{\frac{2}{\pi}}\frac{v^2}{\sigma^3}\exp\left(-\frac{v^2}{2\sigma^2}\right)\Theta(v_{\text{esc}} - v), \\ N &= \text{Erf}\left(\frac{v_{\text{esc}}}{\sqrt{2}\sigma}\right) - \sqrt{\frac{2}{\pi}}\frac{v_{\text{esc}}}{\sigma}\exp\left(-\frac{v^2}{2\sigma^2}\right), \end{aligned} \tag{5.22}$$

where $\Theta$ and Erf are, respectively, the Heaviside Theta Function and the Error Function. We consider a peak velocity of $v_{\text{peak}} = 230$ km/sec, corresponding to $\sigma = 163$ km/sec and $v_{\text{esc}} = 600$ km/sec [6].

As in all Direct Detection scenarios, we assume that DM interacts with SM particles, and thus it can also interact with CRs. In such DM–CR interactions, DM particles, initially at rest due to their non-relativistic nature in the cold DM paradigm, can gain kinetic energy from the relativistic CRs. This process leads to an upscattering of DM, resulting in a population with kinetic energies significantly higher than those typical of the Standard Halo.

Furthermore, to embed the DM- and CR-distributions in the galaxy, the $J$-factor is considered. This factor is an astrophysical quantity, which depends on $l$ and $b$, respectively the galactic longitude and latitude. This factor is defined as:

$$J(b,l) = \int_{l.o.s} dL \rho_\chi(r) = \int_{l.o.s} dL \rho_\odot \frac{r_\odot (r_\odot + r_c)^2}{r(r+r_c)^2}, \tag{5.23}$$

since we consider the Navarro–Frenk–White (NFW) profile as DM density profile $\rho_\chi(r) = \rho_{\text{NFW}}(r)$. This profile was introduced in Section 2.3 and is shown in Figure 5.3.
Since we expect a DM distribution peaked in the Galactic Center, we bound the integration in a leaky cylinder; we choose the radius and the half width as $R = 10$ kpc and $h = 1$ kpc. Finally, considering the NFW profile, we have that $r$ is the distance from the galactic center, and we take $r_\odot = 8.5$ kpc, $r_c = 20$ kpc, $\rho_\odot = 0.42$ GeV/cm$^3$.

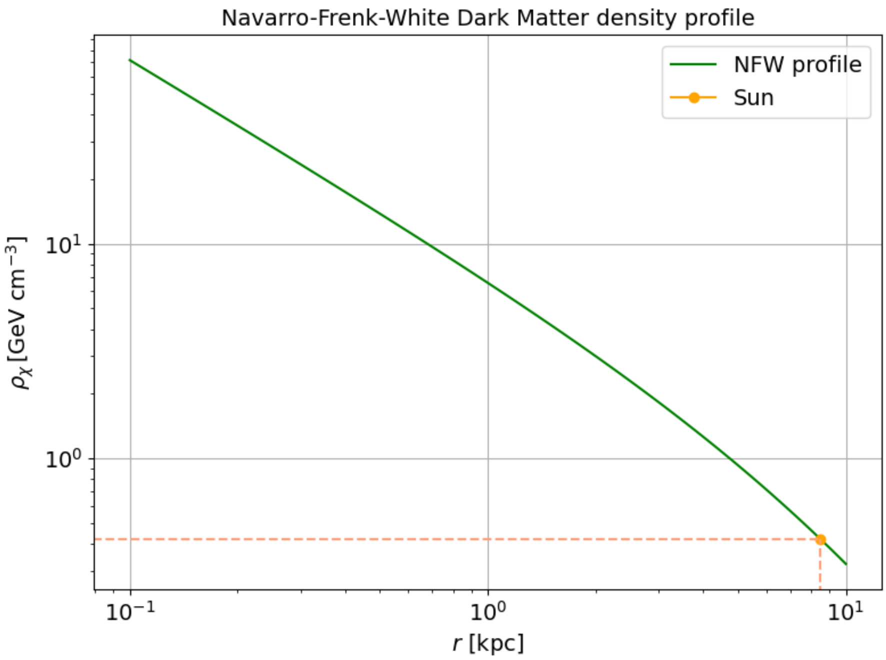


**Figure 5.3.** Navarro-Frenk-White profile, used to parametrize the Galactic DM Halo density profile.

In our model, we assume a CRs flux homogeneous in a leaky cylinder centered on the galactic center, and vanishing outside, therefore the DM flux upscattered by the CRs is given by

$$\frac{d\Phi_\chi}{d\Omega} = \frac{J(l,b)}{m_\chi} \sum_A \int dK_A \frac{d\Phi_A}{d\Omega} \frac{d\sigma}{dK_\chi}, \tag{5.24}$$

where $J(b,l)$ is the $J$-factor, $d\phi_A/d\Omega$ is the differential CRs flux, $K_A$ is the CRs kinetic energy, and $d\sigma/dK_\chi$ is the cross-section computed previously.

Since we are considering hadrophilic DM, the leading source of the high-energy component of the DM flux comes from collisions with two CRs components: Hydrogen and Helium nuclei.
For a scalar mediator, the SM quarks interact with the DM via the scalar operator $\bar{q}q$. This scattering, as shown in Appendix B, is spin-independent in the non-relativistic regime and its strength is proportional to the nucleon mass. As a result, Hydrogen and Helium nuclei can contribute to the scattering process both in the relativistic and in the non-relativistic regime, as the total cross-section is provided by the sum over all nucleons of the target nucleus. Therefore, for scalar-mediated interactions, we include both Hydrogen and Helium in our scattering targets, and this implies that $A =$ p, He.
On the other hand, in the case of a pseudoscalar mediator, the DM interacts via the spin-dependent pseudoscalar operator $\bar{q}\gamma_5 q$. Appendix B discusses limits derived in the non-relativistic regime. In that regime, the pseudoscalar interaction couples to the net spin of the target nucleus, and Helium-4, having zero nuclear spin, does not contribute at leading order. However, in the relativistic regime, Helium nuclei can contribute to the scattering process despite their zero net spin. Therefore, also in the case of pseudoscalar-mediated interactions, both Hydrogen and Helium should be included as scattering targets $A =$ p, He.

The differential DM flux defined in Equation (5.24) is not homogeneous across the Galactic sky; due to the dependence of the J-factor on $l$ and $b$, and the choice of the NFW profile, it is strongly peaked toward the Galactic Center, as can be seen in Figure 5.4.

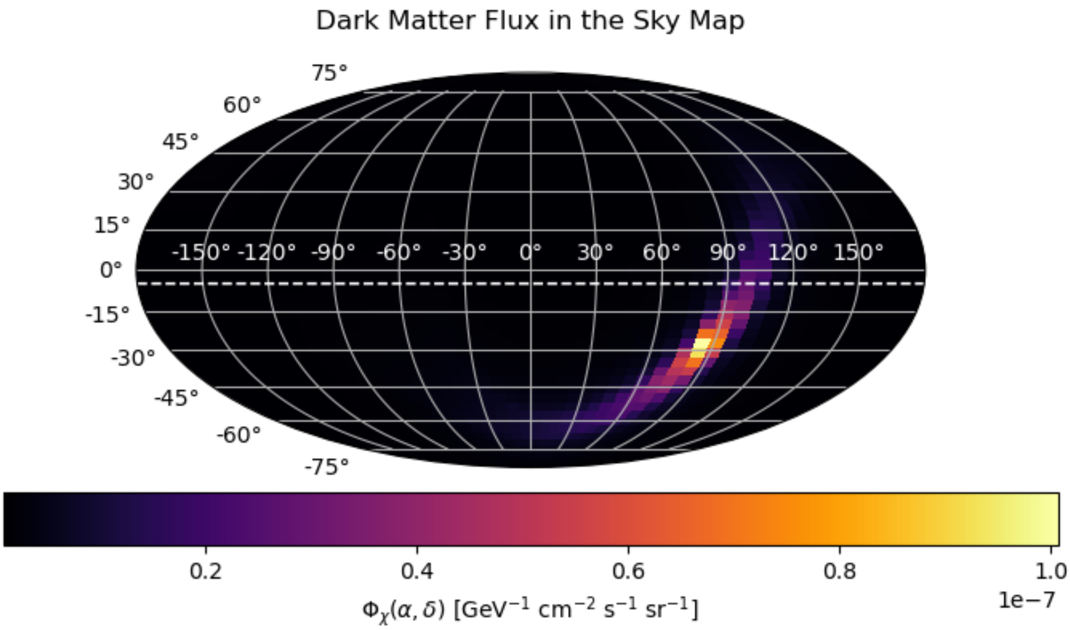


**Figure 5.4.** Map of the Galactic sky where we show only our DM flux for the following parameters: $K_\chi = 1\text{GeV}\,, m_\chi = 0.01\,\text{GeV}\,, m_\phi = 1\text{GeV}\,, g_{u\phi} = 0.1\,, g_{\chi\phi} = 1$. As can be seen, it is peaked at the Galactic Center, $(l, b) = (0°, 0°)$, or in equatorial coordinates, $(\alpha_0, \delta_0) = (266.4°, -28.9°) = (86.4°, -28.9°)$.

After defining all the relevant quantities involved in its derivation, in Figure 5.5 we present the upscattered DM flux, sky-integrated and computed for fixed values of the model parameters: $m_\chi = 0.010$ GeV, $m_\phi = 1$ GeV and $g_{\chi\phi}g_{u\phi} = g_{\chi\phi}g_{d\phi} = 0.1$ for the scalar mediator case, while $m_\chi = 0.010$ GeV, $m_a = 1$ GeV and $g_{\chi a}g_{ua} = g_{\chi a}g_{da} = 0.1$ for the pseudoscalar mediator case.
As can be seen from this plot, the flux of upscattered DM in the pseudoscalar case peaks at higher energies compared to the scalar case. This is a very interesting feature for its detection in IceCube, since, as shown later, the effective area of the experiment is larger at energies of tens of GeV and above.
With respect to the DM fluxes presented in Ref. [6], these fluxes results slightly varied, especially for the scalar mediator case; this difference is due to an updating of the CRs fluxes.

Furthermore, in Figure 5.6, we present this flux compared with the DM Halo one.
From the comparison plot, we see that the intensity of the upscattered fluxes is much smaller than the Halo one (even of $15$ orders of magnitude), but as expected, they're in the higher-energy region; this is an essential condition to probe these DM components using neutrino experiments.

Finally, we present a set of plots to illustrate the dependence of the upscattered DM flux on the parameters of the model. Since the dependence on the couplings is purely multiplicative, we do not provide a dedicated plot for it. On the other hand, the dependence on the DM mass and on the mediator mass is more intricate.
For the scalar mediator case, the dependence on the DM mass is shown in Figure 5.7, while the dependence on the mediator mass is presented in Figure 5.8. For the pseudoscalar mediator case, the DM mass dependence is shown in Figure 5.9, and the mediator mass dependence in Figure 5.10.

From these plots, we can see that varying the DM mass increases the flux and shifts the peak to progressively lower energies as the mass increases. On the other hand, changing the mediator mass leaves the shape of the flux practically unchanged, although the flux is strongly suppressed as the mediator mass increases.

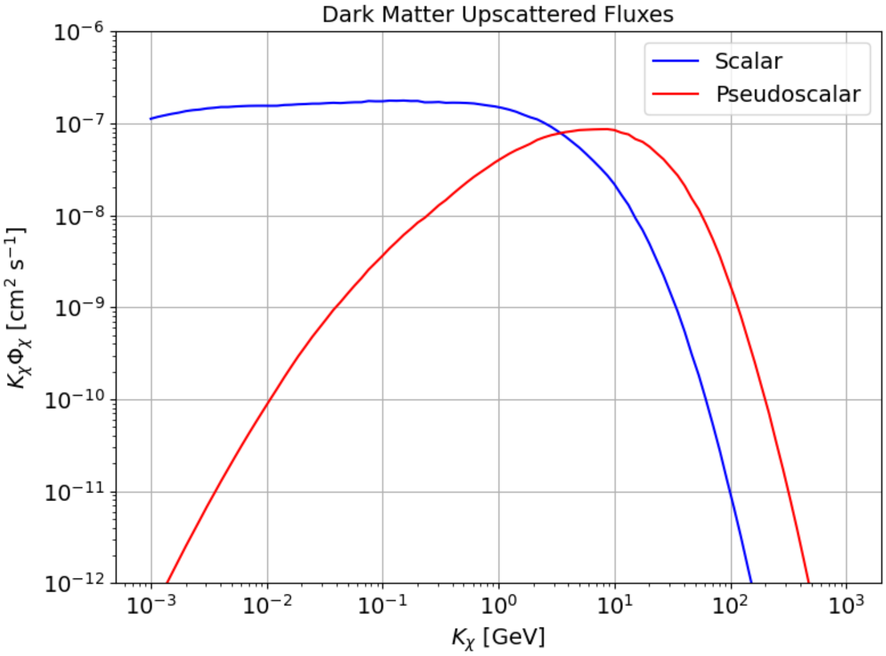


**Figure 5.5.** Upscattered DM fluxes at Earth, computed for the following parameters' values: $m_\chi = 10$ MeV, $m_\phi = m_a = 1$ GeV and $g_{\chi\phi}g_{u\phi} = g_{\chi a}g_{ua} = 0.1$. Results for the scalar and pseudoscalar mediator scenarios are shown in blue and red, respectively.
These fluxes results slightly varied in respect to the ones reported in [6], especially for the scalar case; this is due to the updating of the CRs fluxes.

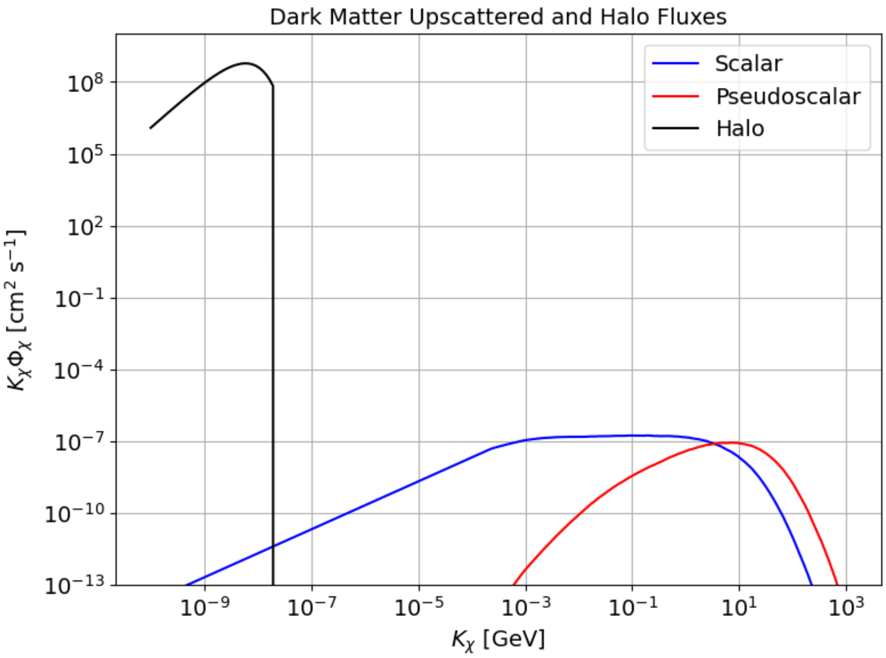


**Figure 5.6.** Dark Matter fluxes at Earth, for the following parameters' values: $m_\chi = 10$ MeV, $m_\phi = m_a = 1$ GeV and $g_{\chi\phi}g_{u\phi} = g_{\chi a}g_{ua} = 0.1$. The Halo is also shown as a comparison (in black). We immediately see that the DM component upscattered by CRs has a lower flux but at higher Kinetic Energies $K_\chi$, as expected.

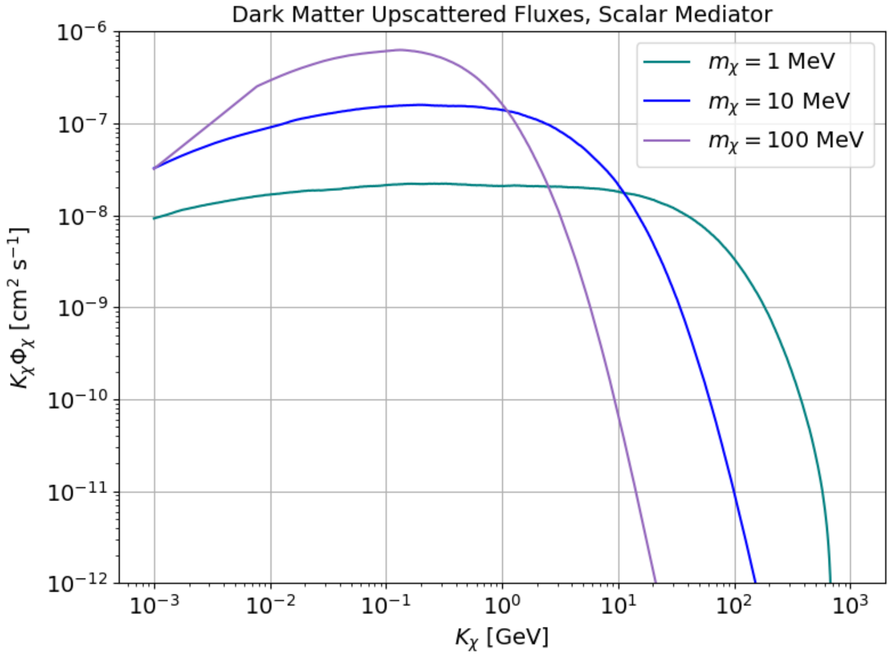


**Figure 5.7.** DM upscattered flux for the scalar mediator case, computed for different DM masses: $m_\chi = 0.001$ GeV in teal, $m_\chi = 0.010$ GeV in blue and $m_\chi = 0.100$ GeV in violet. Here the mediator mass and the coupling are fixed respectively at $m_\phi = 1$ GeV and $g_{u\phi} g_{\chi\phi} = 0.1$ .

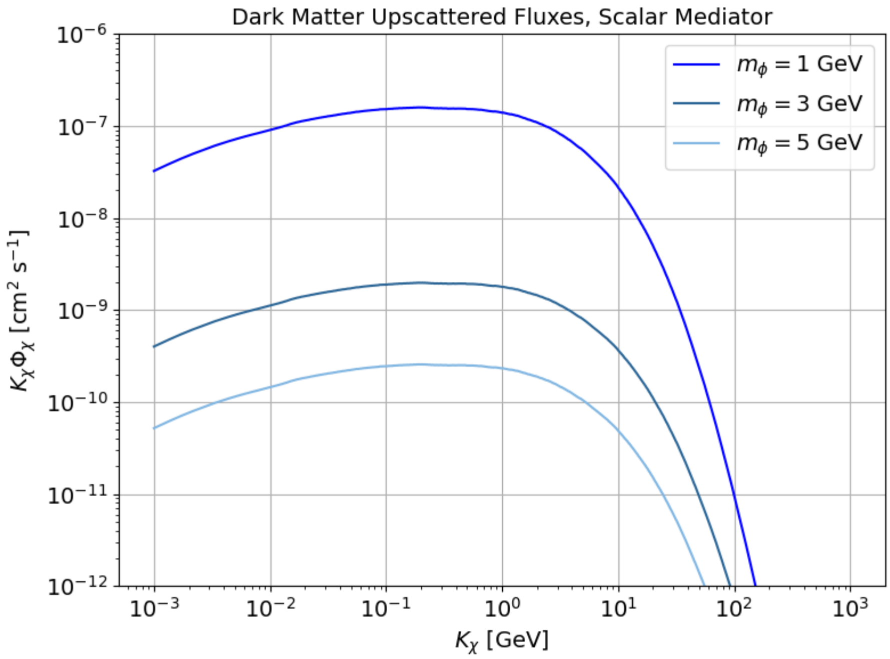


**Figure 5.8.** DM upscattered flux for the scalar mediator case, computed for different mediator masses: $m_\phi = 1$ GeV in blue, $m_\phi = 3$ GeV in petrol blue and $m_\phi = 5$ GeV in light blue. Here the DM mass and the coupling are fixed respectively at $m_\chi = 1$ GeV and $g_{u\phi} g_{\chi\phi} = 0.1$ .

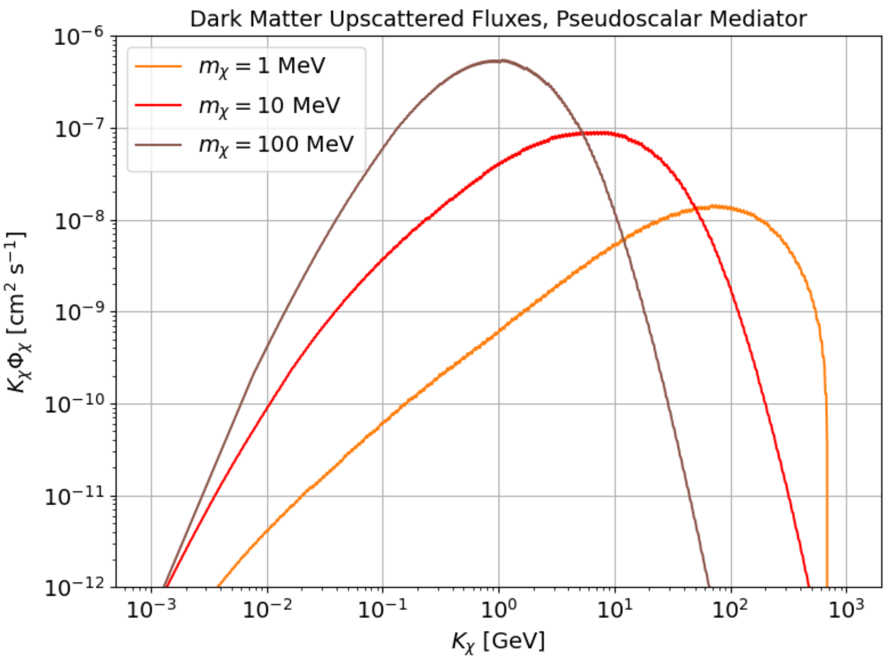


**Figure 5.9.** DM upscattered flux for the pseudoscalar mediator case, computed for different DM masses: $m_\chi = 0.001$ GeV in orange, $m_\chi = 0.010$ GeV in red and $m_\chi = 0.100$ GeV in brown. Here the mediator mass and the coupling are fixed respectively at $m_a = 1$ GeV and $g_{ua}g_{\chi a} = 0.1$ .

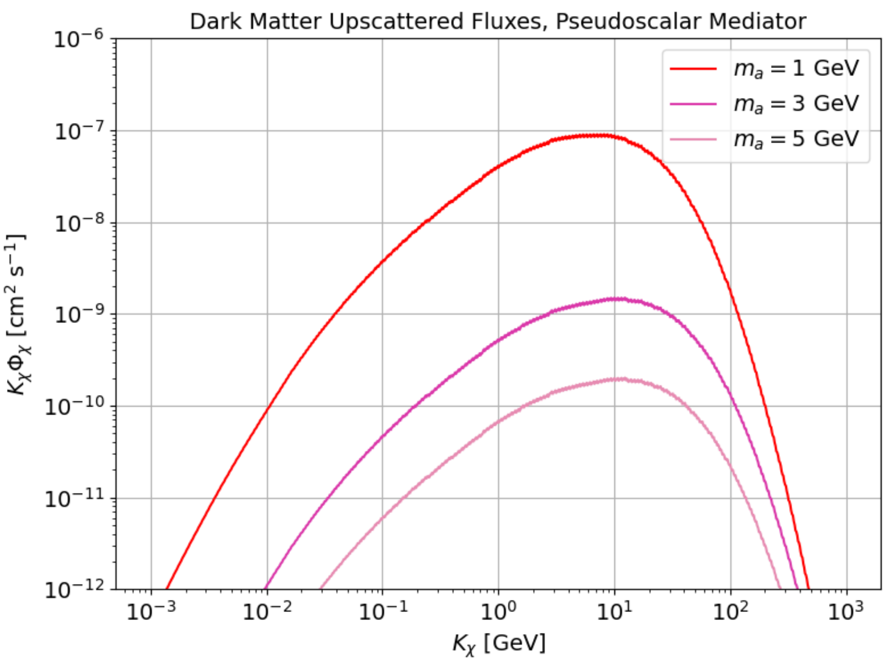


**Figure 5.10.** DM upscattered flux for the pseudoscalar mediator case, computed for different mediator masses: $m_a = 1$ GeV in red, $m_a = 3$ GeV in magenta and $m_a = 5$ GeV in pink. Here the DM mass and the coupling are fixed respectively at $m_\chi = 1$ GeV and $g_{ua}g_{\chi a} = 0.1$ .

### 5.2.2 Events at IceCube Detector

Once the DM particle interacts with the CRs and has been accelerated, then it can reach one of the existing detectors on Earth and interact with a target particle; if the target's recoil energy is higher than the threshold, then this interaction can be detected.
Considering water Cherenkov neutrino detectors, as IceCube, which is mainly composed of water, we assume that our target is composed only of protons and Oxygen nuclei. Given that the transferred momenta in the DM-target nuclei interactions are quite high, we have to consider that we can resolve the inner structure of Oxygen nuclei, and therefore we consider the DM scattering with protons, given by both Oxygen and Hydrogen nuclei.

The goal of this Section is to compute the DM event rates at the neutrino detectors, neglecting, as a first approximation, the Earth and Ice attenuation.
The number of expected DM events at the detector defined in Ref. [6] is experiment-independent and can be a good approximation; moreover, we can delve into a more accurate analysis considering public IceCube data. We can start from the previous knowledge about neutrino-proton interaction in the detectors. Determining the needed correction factors, we can study the DM interactions in the detector.

To be sensitive to an energy range of $E_\chi > 500$ MeV, we consider a combination of *ELOWEN* and *GRECO*, the two event selections already described in Section 4.3.
In general, the number of expected neutrino events in the detector [126] is given by

$$N_\nu = t \int dE A^\nu_{\text{eff}}(E)\Phi^\nu(E)\,, \tag{5.25}$$

where $t$ is the acquisition time, $A^\nu_{\text{eff}}$ is the effective area, and $\Phi^\nu(E)$ is the neutrino flux. The effective area is generically defined as

$$A^\nu_{\text{eff}} = \sigma_{\nu p} \cdot N_T \cdot \epsilon, \tag{5.26}$$

where $\sigma_{\nu p}$ is the cross-section for the neutrino-proton interactions, $N_T$ is the number of target particles of the detector, and $\epsilon$ is the detector efficiency, such that $\epsilon \leq 1$.

If now we consider the DM interactions with the target protons, the number of expected events is given by

$$\boxed{N_{\text{DM}} = t \int dE A^{\text{DM}}_{\text{eff}}(E)\Phi^{\text{DM}}(E)} \tag{5.27}$$

where $A^{\text{DM}}_{\text{eff}}$ is the DM effective area, and $\Phi^{\text{DM}}$ is the DM Flux computed in the previous section. At this stage, we consider the sky-integrated DM flux; moreover, in the following, also the directionality of the signal is considered.

## DM Effective Area definition

Similarly to the neutrino case, the DM effective area can be defined as

$$A_{\text{eff}}^{\text{DM}} = \sigma_{\text{DM}p} \cdot N_T \cdot \epsilon \tag{5.28}$$

in first approximation, we assume that this effective area differs from the neutrino one only due to the cross-section. This is a simple prescription to get an estimate in this thesis, and a more refined derivation of the DM effective area would be needed for future studies

Therefore, the DM Effective Area can be obtained by a rescaling of $A_{\text{eff}}^{\nu}$. This implies that, to obtain $A_{\text{eff}}^{\text{DM}}$, the only missing point is the ***cross-section corrective factor***:

$$F(K) \equiv \frac{\sigma_{\text{DM}p}(K)}{\sigma_{\nu p}(K)}; \tag{5.29}$$

this factor is energy-dependent because of the energy dependence of the cross-sections.

To obtain the corrective factor, we use as input the DM cross-section parametrized by the model and the neutrino cross-section, both as a function of the kinetic energy. To better parameterize the energy dependence of $A_{\text{eff}}^{\nu}$, we consider two different samples: *ELOWEN* for smaller energies and *GRECO* for higher ones.

Since *ELOWEN* and *GRECO* Neutral Current effective areas are not published, we assume that Neutral Current and Total effective areas have the same shape; in this way, we can consider the total all-flavor effective area. These effective areas are shown in Figure 5.11.

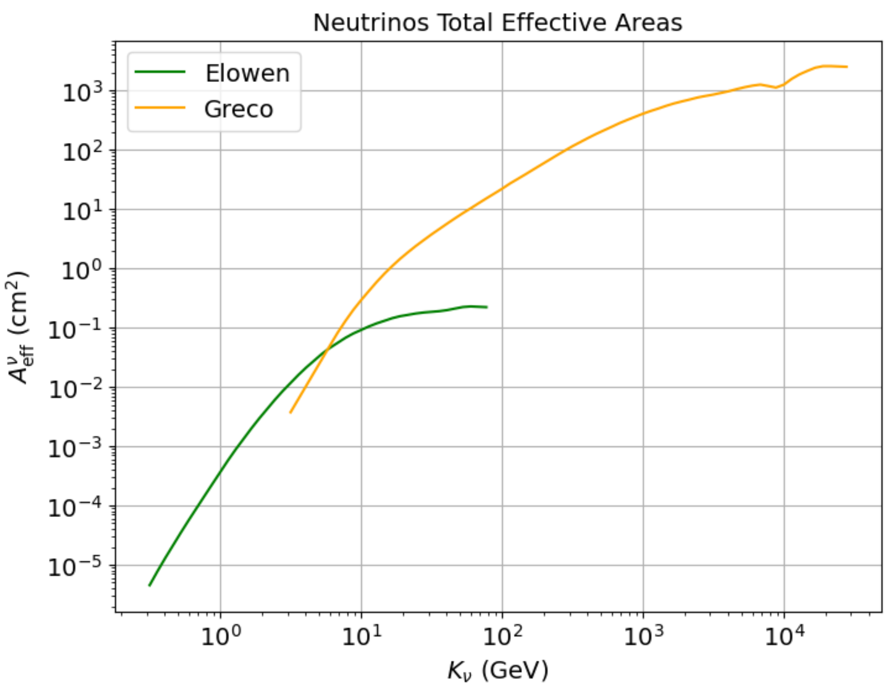


**Figure 5.11.** Neutrino's total and all-flavor effective area for *ELOWEN* event selection (in green, credits: [126]) and *GRECO* event selection (in orange, credits: [122])

Regarding the neutrino cross-section, we have considered the ones well known in the literature; in particular, we have used the ones provided in [89].
To obtain the correct rescaling of the neutrino effective area, the rescaling must be performed considering the cross-section of the appropriate kind of interaction.
Since the expected DM interaction in our detector is of neutral current type, we should use the NC neutrino effective area, rescaled by a factor dependent on the NC neutrino cross-sections. However, since the only publicly available data are the total effective areas for the *ELOWEN* and *GRECO* selection criteria, we will rescale them using the total cross-sections, assuming that the energy dependence of the effective areas and cross-sections is the same for the NC and total cases.
Hence, we consider the total neutrino-nucleon cross-section to rescale both *ELOWEN* and *GRECO* effective area; this total neutrino cross-section is shown in Figure 5.12.
Once these corrective factors are defined, the derivation of the DM effective areas is straightforward. In Figure 5.13, we show the DM effective areas for both the scalar and pseudoscalar cases, and for comparison, we also include the neutrino effective areas.

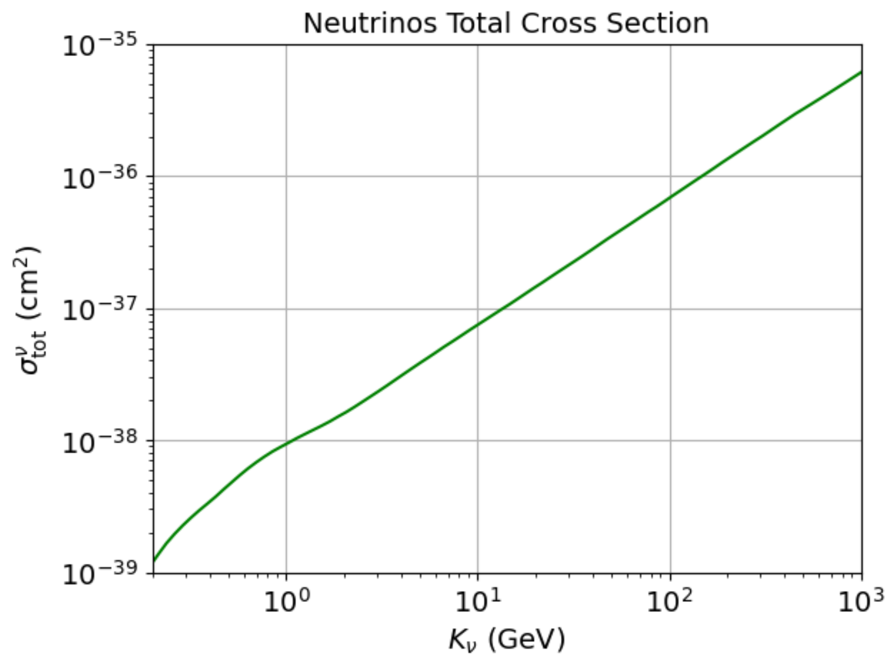


**Figure 5.12.** Neutrino-nucleon cross-section as a function of the neutrino kinetic energy. This plot is obtained by adapting Figure 9 from [89].

## Number of Expected Dark Matter Events at IceCube

Once we have obtained the DM Effective Area, from Equation (5.27) we can obtain the number of expected DM events at IceCube. Depending on their values, we need to consider how to proceed: if this number is higher than the background rate, we can already obtain sensitivities; otherwise, we need to perform a more precise analysis, for instance, by reducing the background rate. In Figure 5.14, the sky-integrated number of events for both scalar and pseudoscalar mediator case in shown; we fix the parameters as $m_\chi = 0.010$ GeV, $m_\phi = m_a = 1$ GeV, and $g_{u\phi}g_{\chi\phi} = g_{\chi a}g_{ua} = 0.1$.

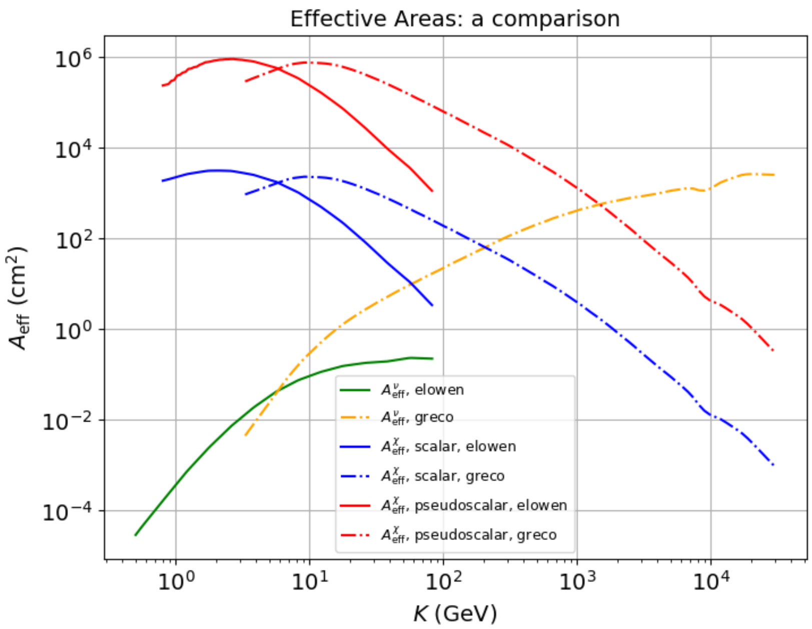


**Figure 5.13.** This plot presents the following effective areas: in blue, the DM effective area for the scalar case, solid line for the one derived from *ELOWEN* and dash-dotted line for the one from *GRECO*; in red, the DM effective area for the pseudoscalar case, solid line for *ELOWEN* and dash-dotted line for *GRECO*. Finally, the neutrino effective areas are also shown: in solid green for *ELOWEN* and in dash-dotted orange for *GRECO*. The DM effective areas have been obtained for $m_\chi = 0.01$ GeV, $m_\phi = m_a = 1$ GeV and $g_{u\phi} g_{\chi\phi} = g_{ua} g_{\chi a} = 0.1$ .

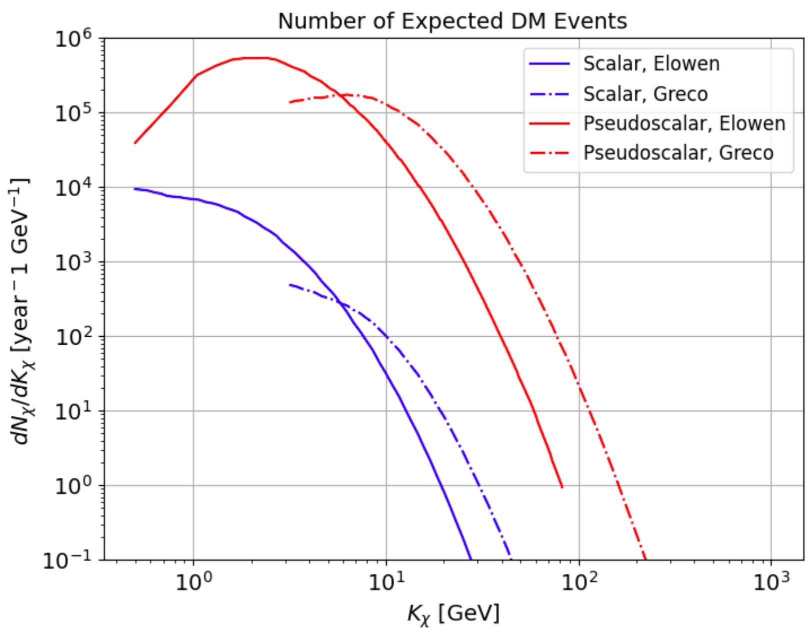


**Figure 5.14.** Sky-integrated number of DM expected events at IceCube. In blue, the scalar mediator case is shown, with a continuum line for the number of events obtained from *ELOWEN* event selection and with a dashed-dotted line for the ones obtained with *GRECO*. Similarly, for the pseudoscalar mediator case, these results are shown in red. These events have been obtained for $m_\chi = 0.01$ GeV, $m_\phi = m_a = 1$ GeV and $g_{u\phi} g_{\chi\phi} = g_{ua} g_{\chi a} = 0.1$ .

The difference in the effective areas between the scalar and pseudoscalar cases, as shown in Figure 5.13, is due to the difference in the differential cross-sections for the DM-SM interactions mediated via a scalar or a pseudoscalar particle.
Furthermore, the difference in the expected number of events between the scalar and pseudoscalar cases, as shown in Figure 5.14, is also due to the scalar DM flux peaking at lower energies compared to the pseudoscalar DM flux.

To gain a general understanding of what we expect, we report in the following tables the number of expected DM events, sky-integrated, for both *ELOWEN* and *GRECO* event selections. We report these values for some values of the DM and mediator masses and of the couplings.

## Dark Matter Mass Dependence

In the following two tables, we present, for scalar and pseudoscalar mediators respectively, the number of expected events at IceCube in 1 year of detection, depending on the Dark Matter mass (different rows) and on the mediator-quark coupling[2] (different columns). We present the results for the scalar case with $m_\phi = 1$ GeV, and for the pseudoscalar case with $m_a = 1$ GeV, respectively in Table 5.1 and in Table 5.2. Here we report the sky-integrated number of expected events computed using *ELOWEN* and *GRECO* event selection, respectively $N_e$ and $N_g$.

| | $g_{u\phi} = 0.1$ | $g_{u\phi} = 0.01$ | $g_{u\phi} = 0.003$ |
|---|---|---|---|
| $m_{\text{DM}} = 1$ MeV | $N_e = 3.19 \times 10^1$<br>$N_g = 1.61 \times 10^1$ | $N_e = 3.19 \times 10^{-3}$<br>$N_g = 1.61 \times 10^{-3}$ | $N_e = 2.58 \times 10^{-5}$<br>$N_g = 1.30 \times 10^{-5}$ |
| $m_{\text{DM}} = 10$ MeV | $N_e = 1.45 \times 10^4$<br>$N_g = 1.42 \times 10^3$ | $N_e = 1.45 \times 10^0$<br>$N_g = 1.42 \times 10^{-1}$ | $N_e = 1.18 \times 10^{-2}$<br>$N_g = 1.15 \times 10^{-3}$ |
| $m_{\text{DM}} = 100$ MeV | $N_e = 9.15 \times 10^5$<br>$N_g = 1.41 \times 10^3$ | $N_e = 9.15 \times 10^1$<br>$N_g = 1.41 \times 10^{-1}$ | $N_e = 7.41 \times 10^{-1}$<br>$N_g = 1.14 \times 10^{-3}$ |

**Table 5.1.** Number of events at the detector in 1 year, scalar mediator with $m_\phi = 1$ GeV.

| | $g_{ua} = 0.1$ | $g_{ua} = 0.01$ | $g_{ua} = 0.003$ |
|---|---|---|---|
| $m_{\text{DM}} = 1$ MeV | $N_e = 7.70 \times 10^4$<br>$N_g = 1.98 \times 10^5$ | $N_e = 7.70 \times 10^0$<br>$N_g = 1.98 \times 10^1$ | $N_e = 6.23 \times 10^{-2}$<br>$N_g = 1.60 \times 10^{-1}$ |
| $m_{\text{DM}} = 10$ MeV | $N_e = 2.40 \times 10^6$<br>$N_g = 1.75 \times 10^6$ | $N_e = 2.40 \times 10^2$<br>$N_g = 1.75 \times 10^2$ | $N_e = 1.94 \times 10^0$<br>$N_g = 1.42 \times 10^0$ |
| $m_{\text{DM}} = 100$ MeV | $N_e = 8.86 \times 10^6$<br>$N_g = 4.09 \times 10^5$ | $N_e = 8.86 \times 10^2$<br>$N_g = 4.09 \times 10^1$ | $N_e = 7.18 \times 10^0$<br>$N_g = 3.31 \times 10^{-1}$ |

**Table 5.2.** Number of events at the detector in 1 year, pseudoscalar mediator with $m_a = 1$ GeV.

From these tables, we can infer a general behaviour:

[2] We're working in the isoscalar coupling assumption, so $g_{u\phi} = g_{d\phi}$ and $g_{ua} = g_{da}$.

- increasing the DM mass, the number of expected events slowly increases, even if there are some exceptions. Regarding the expected events from *GRECO* effective area, between $m_\chi = 10$ MeV and $m_\chi = 100$ MeV we have a decrease. This is due to the fact that the flux's peak is shifting at lower energies, where *GRECO* effective area is cut;
- decreasing the couplings, the number of expected events has a fast decrease;
- the number of expected events for the pseudoscalar mediator is larger than the one expected with a scalar mediator, even by some orders of magnitude.

## Mediator Mass Dependence

As before, in the following two tables we present the number of expected events at IceCube in 1 year of detection, depending on the mediator mass (different rows) and on the mediator-quark coupling (different columns). We present the results, with $m_\chi = 10$ MeV, for the scalar case and for the pseudoscalar case respectively in Table 5.1 and in Table 5.2.

| | $g_{u\phi} = 0.1$ | $g_{u\phi} = 0.01$ | $g_{u\phi} = 0.003$ |
|---|---|---|---|
| $m_\phi = 1$ GeV | $N_e = 1.45 \times 10^4$<br>$N_g = 1.42 \times 10^3$ | $N_e = 1.45 \times 10^0$<br>$N_g = 1.42 \times 10^{-1}$ | $N_e = 1.18 \times 10^{-2}$<br>$N_g = 1.15 \times 10^{-3}$ |
| $m_\phi = 3$ GeV | $N_e = 2.38 \times 10^0$<br>$N_g = 3.01 \times 10^{-1}$ | $N_e = 2.38 \times 10^{-4}$<br>$N_g = 3.01 \times 10^{-5}$ | $N_e = 1.93 \times 10^{-6}$<br>$N_g = 2.44 \times 10^{-7}$ |
| $m_\phi = 5$ GeV | $N_e = 4.03 \times 10^{-2}$<br>$N_g = 5.57 \times 10^{-3}$ | $N_e = 4.01 \times 10^{-6}$<br>$N_g = 5.57 \times 10^{-7}$ | $N_e = 3.26 \times 10^{-8}$<br>$N_g = 4.51 \times 10^{-9}$ |

**Table 5.3.** Number of events at the detector in 1 year, with $m_{\text{DM}} = 10$ MeV, scalar mediator.

| | $g_{ua} = 0.1$ | $g_{ua} = 0.01$ | $g_{ua} = 0.003$ |
|---|---|---|---|
| $m_a = 1$ GeV | $N_e = 2.40 \times 10^6$<br>$N_g = 1.75 \times 10^6$ | $N_e = 2.40 \times 10^2$<br>$N_g = 1.75 \times 10^2$ | $N_e = 1.94 \times 10^0$<br>$N_g = 1.42 \times 10^0$ |
| $m_a = 3$ GeV | $N_e = 2.10 \times 10^3$<br>$N_g = 2.47 \times 10^3$ | $N_e = 2.10 \times 10^{-1}$<br>$N_g = 2.47 \times 10^{-1}$ | $N_e = 1.70 \times 10^{-3}$<br>$N_g = 2.00 \times 10^{-3}$ |
| $m_a = 5$ GeV | $N_e = 4.91 \times 10^1$<br>$N_g = 6.58 \times 10^1$ | $N_e = 4.91 \times 10^{-3}$<br>$N_g = 6.58 \times 10^{-3}$ | $N_e = 3.97 \times 10^{-5}$<br>$N_g = 5.33 \times 10^{-5}$ |

**Table 5.4.** Number of events at the detector in 1 year, with $m_{\text{DM}} = 10$ MeV, pseudoscalar mediator.

From these tables, we can infer a general behaviour:

- increasing the mediator mass, the number of expected events decreases;
- decreasing the couplings, the number of expected events has a fast decrease;
- the number of expected events for the pseudoscalar mediator is larger than the one expected with a scalar mediator, as in the previous tables.

## Preliminary Considerations on the Number of Expected Events

The number of expected events obtained in the previous paragraphs, must be confronted with the IceCube background, in order to infer if is possible to get some sensitivity limits with pubblic effective areas.
For *ELOWEN* selection criteria, the background is constant [103] at

$$\boxed{N_{\text{bkg}}^{\text{ELOWEN}} \sim 0.021\text{Hz} \sim 6.6 \times 10^5 \text{ year }^{-1}} \tag{5.30}$$

while for *GRECO* selction criteria, it depends on the sky-direction, and the all-sky integrated value [123] is

$$\boxed{N_{\text{bkg}}^{\text{GRECO}} \sim 0.0046 \text{ Hz} \sim 1.5 \times 10^5 \text{ year }^{-1}} \tag{5.31}$$

From the number of expected events computed before, we believe that the spin-dependent interactions, mediated by a pseudoscalar mediator, is the most promising field of investigation, since the sky-integrated number of events are comparable with the background at least for large couplings.

## Number of Expected Events: Dependence on the Sky-Direction

An interesting aspect of our DM signal, which can be considered to improve the analysis, is the directionality: given the shape of the DM density profile (NFW profile), we expect a signal peaked in the Galactic Center.
This aspect can be considered only if we can reconstruct the direction of the expected events in IceCube; since the public *ELOWEN* effective area is the sky-integrated one, we lose the direction information of the signal.
On the contrary, using *GRECO* event selection, we have direction discrimination; therefore we can select only a specific sky region. Since the signal is peaked in the galactic center, we select the region of sky with $\delta \in (-90°, -5°)$.

At the beginning of this chapter, we have considered the *sky-integrated DM flux* as $\Phi_\chi$; hence, the number of expected events is sky-averaged and is given by Equation (5.27):

$$N_\chi = t \cdot \int dK_\chi \Phi_\chi(K_\chi) A_{\text{eff}}^{DM}(K_\chi). \tag{5.32}$$

To consider also the information of the directionality of the signal, we can also consider the number of events as a function of the sky's direction; the differential DM flux is given by

$$\frac{d\Phi_\chi}{d\Omega} = \frac{J(b,l)}{m_\chi} \sum_A \int dK_A \frac{d\Phi_A}{d\Omega} \frac{d\sigma}{dK_\chi}. \tag{5.33}$$

Then the differential number of events in galactic coordinates is given by

$$\frac{dN}{d\Omega}(l,b) = t \int dK_\chi \frac{d\Phi_\chi}{d\Omega}(l,b) A_{\text{eff}}^{DM}(K_\chi). \tag{5.34}$$

This expression, integrated in the whole sky, returns the sky-integrated number of events analyzed previously; hence in *ELOWEN*, where we do not have direction-reconstruction [126], the number of expected events is simply

$$N^{\text{ELOWEN}} = \int_{-\pi}^{\pi} dl \int_{-\pi/2}^{\pi/2} d\sin b \frac{dN}{d\Omega}(l,b). \tag{5.35}$$

Regarding *GRECO* event selection, we can select only a region of sky in declination; given the public effective areas [122], we choose to use $A_{\text{eff}}^{\nu,\, GRECO}$ with $\delta \in [-90°, -5°]$, such that

$$A_{\text{eff}}^{\nu,\, GRECO} = \begin{cases} A_{\text{eff}} & \text{if } -90° \leq \delta \leq -5° \\ 0 & \text{if } -5° < \delta \leq 90° \end{cases} \tag{5.36}$$

In this way, we can obtain the number of events for a specific region of sky $\delta \in [-90°, -5°]$, where we assume to have the majority of the DM flux, given that $\delta_{\text{GC}} \sim -29°$.

Therefore, the total number of events for *GRECO* event selection becomes

$$N^{\text{GRECO}}(\alpha,\delta) = \int_{-\pi}^{\pi} d\alpha \int_{-90°}^{-5°} d\sin\delta \frac{dN}{d\Omega}(\alpha,\delta); \tag{5.37}$$

this number will be converted in $N^{\text{GRECO}}(l,b)$, in order to get the plot in galactic coordinates.

The number of DM events expected at IceCube without any selection cut, for the benchmark parameters $m_\chi = 0.01$ GeV, $m_a = 1$ GeV and $g_{ua}g_{\chi a} = 0.1$, are shown, both in equatorial and galactic coordinates, in Figures 5.15 and 5.16. After applying a cut on the equatorial coordinates, the expected number of events is shown, both in equatorial and galactic coordinates, in Figures 5.17 and 5.18; as can be seen, there is a loss of events, but it occurs in the region where the intensity is lowest and therefore has little impact on the sky-integrated result.

These plots are reproduced for the pseudoscalar mediator case, but they can easily be derived also for the scalar case. The behavior in galactic and equatorial coordinates remains the same, since the dependence on these coordinates is encoded solely in the $J$-factor, which is common to both scenarios. The difference lies in the intensity: as previously discussed, the number of expected events in the scalar mediator case is lower respect to the one of the pseudoscalar case, for the same values of coupling, DM and mediator masses.

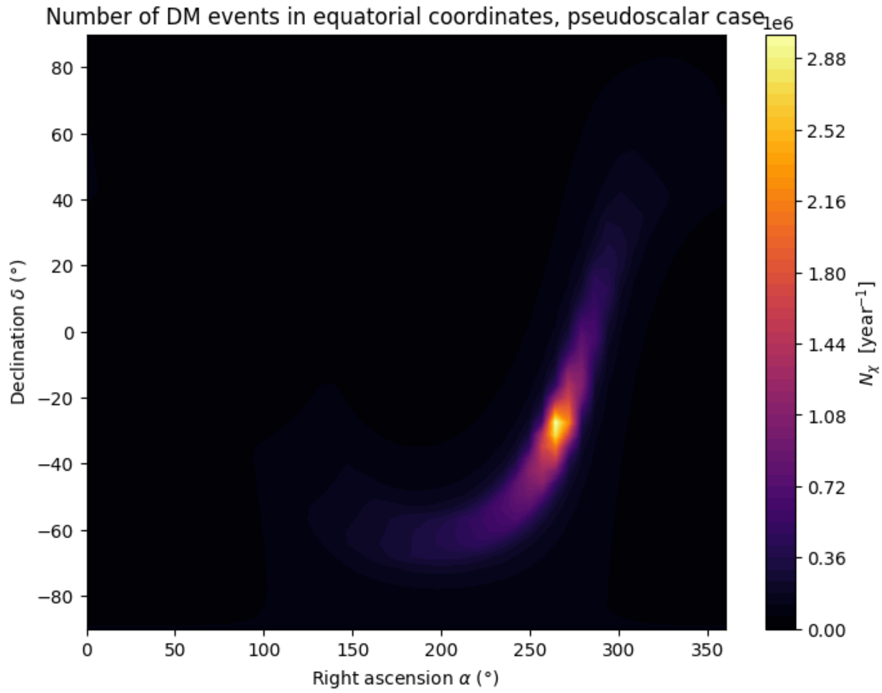


**Figure 5.15.** Expected number of DM events as a function of equatorial coordinates, for $m_\chi = 0.01$ GeV, $m_a = 1$ GeV and coupling $g_{ua}g_{\chi a} = 0.1$, before the cut in declination. This plot has to be compared with Figure 5.17 to see the effects of the cut.

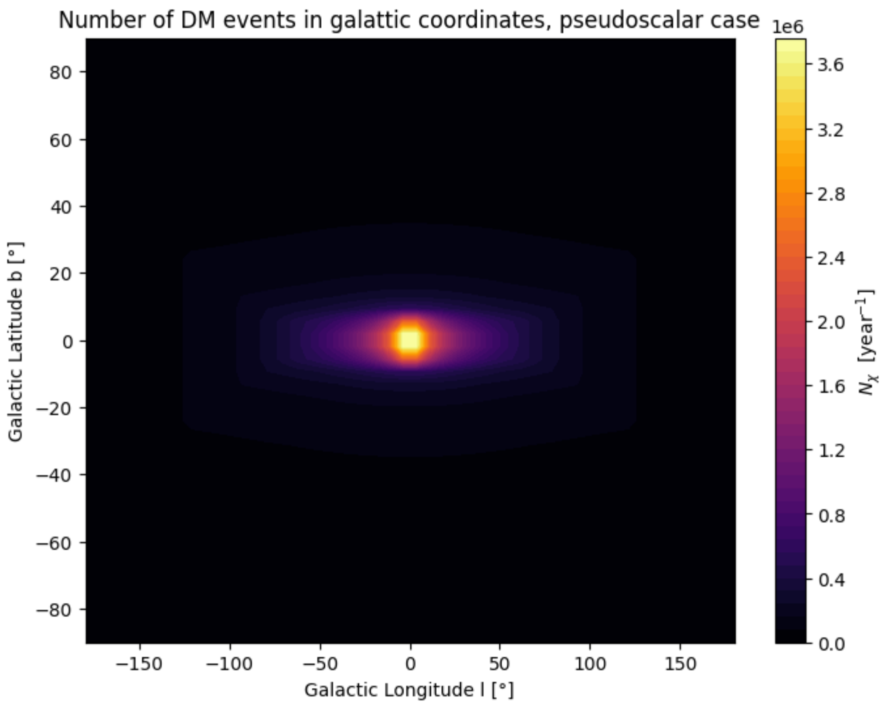


**Figure 5.16.** Expected number of DM events as a function of galactic coordinates, for $m_\chi = 0.01$ GeV, $m_a = 1$ GeV and coupling $g_{ua}g_{\chi a} = 0.1$, before the cut in declination. This plot has to be compared with Figure 5.18 to see the effects of the cut.

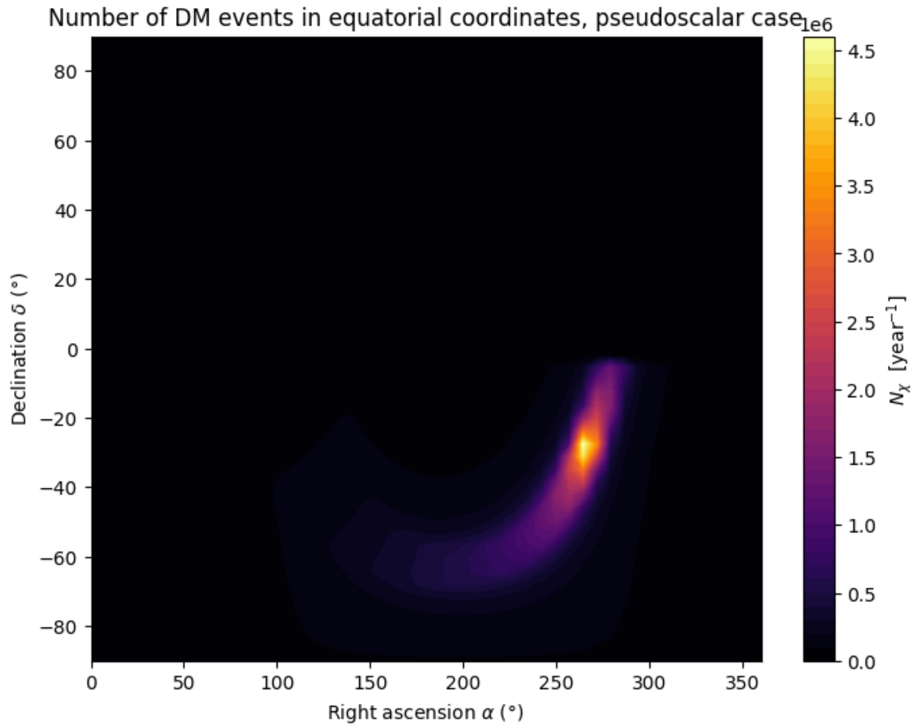


**Figure 5.17.** Expected number of DM events as a function of equatorial coordinates, for $m_\chi = 0.01$ GeV, $m_a = 1$ GeV and coupling $g_{ua}g_{\chi a} = 0.1$, after the cut in declination.

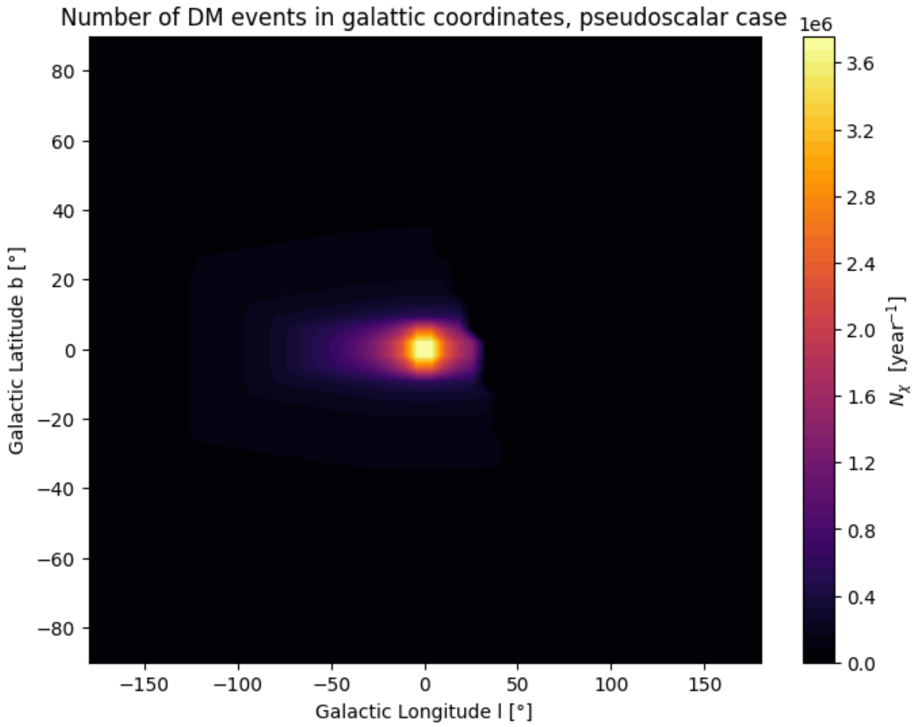


**Figure 5.18.** Expected number of DM events as a function of galactic coordinates, for $m_\chi = 0.01$ GeV, $m_a = 1$ GeV and coupling $g_{ua}g_{\chi a} = 0.1$, after the cut in declination, which translates in a cut in both galactic latitude and longitude.

### 5.2.3 Earth and Ice Attenuation

In the previous section, we computed the number of expected events at IceCube without considering any attenuation of the flux. This is a simplified assumption, in which we consider IceCube as being located on the Earth's surface and that the flux, coming from all directions, does not travel through any amount of matter before reaching the detector. However, this assumption is generally not valid, for two reasons.
First, IceCube is located deep inside the Antarctic ice, at a depth between $1450$ m and $2450$ m; therefore, a particle coming exactly downgoing with respect to the detector must travel through this amount of ice.
Second, considering the various incoming directions of the DM flux, depending on the sky direction, these particles may have to travel through a given amount of Earth's rock or Antarctic ice before reaching the detector.

For these reasons, we need to consider in our analysis the attenuation of the flux due to the distance travelled by the particles through rock or ice.
This attenuation, at the microscopic level, is due to the fact that DM particles, while travelling through these materials, can interact with nucleons before reaching the detector. As a result, their kinetic energy can be reduced, and the particles could even be stopped within the material.
This effect gives an attenuation of the DM flux at the level of the detector. To modelize this flux attenuation, we consider the following approximations [6]: at each scattering

- we impose that the energy loss is equal to its average value (for simplicity),
- we neglect the change of direction of the DM speed.

Finally, what encodes this attenuation is the DM kinetic energy $\bar{K}_\chi$ at the depth $z$, which is smaller with respect to the non-attenuated kinetic energy $K_\chi$, and is given by the following differential equation [6]:

$$\frac{d\bar{K}_\chi(z)}{dz} = \sum_T n_T \int dK_T K_T \frac{d\sigma}{dK_T}, \tag{5.38}$$

where $n_T$ is the number density of a target particle inside the crossed material.

This implies that the DM kinetic energy has a dependence from the depth $z$ as

$$\bar{K}_\chi(z) = K_\chi - n_p z \int dK_T K_T \frac{d\sigma}{dK_T} - n_n z \int dK_T K_T \frac{d\sigma}{dK_T}, \tag{5.39}$$

and on the Earth's surface we have $\bar{K}_\chi(z=0) = K_\chi$. Concerning the target particles, since the typical energy of DM events is above the nuclear energy scale, we can neglect their nuclear structure. This implies that the target particles are protons and neutrons, that we assume in equal quantity; regarding the mass density of the crossed material, for the Earth rocks we have $\rho_{p+n}^{\text{Earth}} = 2.7$ g/cm$^3$, [127] and for the Antarctic Ice $\rho_{p+n}^{\text{Ice}} = 0.92$ g/cm$^3$; in general, to modelize the distributions of rocks and ice around IceCube is quite complex.

Therefore, the next step to implement Earth attenuation in our analysis is to compute the dependence of the traveled distance as a function of $(l, b)$; this is needed to obtain the dependence of the attenuated kinetic energy from the galactic coordinates $\bar{K}_\chi(l, b)$. This depth $z$ traveled inside the matter depends on the incoming direction of the DM particle; calculating this dependence is in general complex, but knowing the exact position of the detector, we can obtain the distance travelled as a function of the zenith angle $z(\theta)$. Then, using a change of coordinates from local coordinates (azimuth, zenith) to galactic ones $(l, b)$ we can obtain the final formulation for $z(l, b)$. This derivation is computed in Appendix D; we obtain that the effective path travelled from a DM particle inside the Earth is

$$z(\theta) = \sqrt{R^2 - (R-d)^2 \sin^2\theta} - (R-d)\cos\theta, \tag{5.40}$$

where $d$ is the vertical depth of the detector and $\theta$ is the zenith angle of the incoming particle.
Then, transforming from IceCube's local reference frame to galactic reference frame, the dependence of the attenuation from the galactic coordinates is obtained. This calculation is performed using the Python package Astropy (The Astropy Project), which provides tools and functionalities for astronomy and astrophysics.

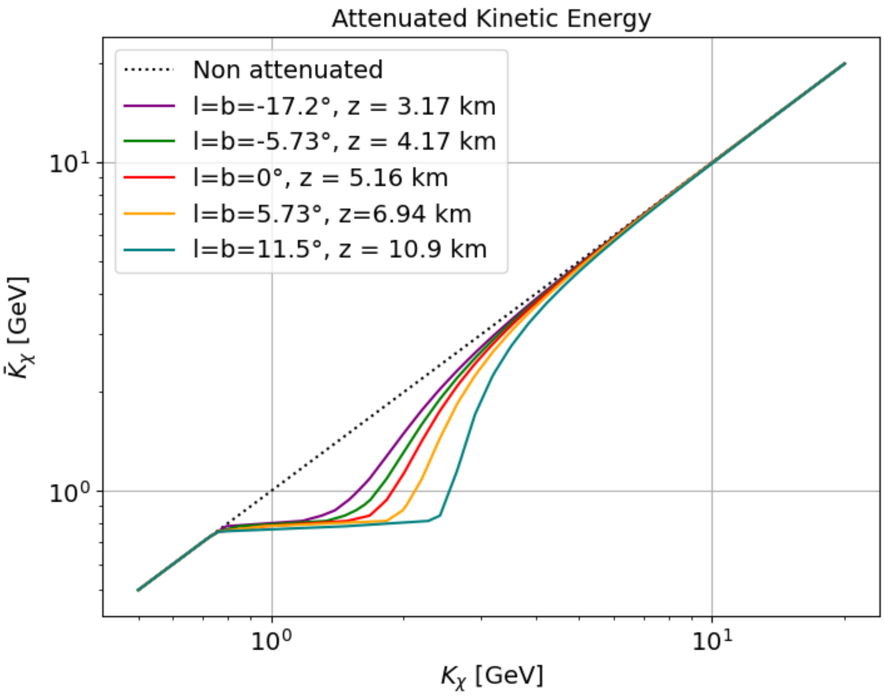


**Figure 5.19.** Attenuated DM kinetic energy as a function of the non attenuated ones, for several values of the galactic coordinates; the non attenuated behavior is shown as a comparison. In red, the kinetic energy's attenuation for particles coming from the Galactic Center is shown. This plot is computed for the pseudoscalar case, with fixed parameters $m_\chi = 0.01$ GeV, $m_a = 1$ GeV and $g_{ua} g_{\chi a} = 0.1$.

Considering the expression in Equation (5.39), we can obtain the attenuated kinetic energy as a function of the non attenuated one. Figure 5.19 shows how this energy

is attenuated, for some values of the galactic coordinates. This plot is computed for the pseudoscalar case, with benchmark parameters $m_\chi = 0.01$ GeV, $m_a = 1$ GeV and $g_{ua}g_{\chi a} = 0.1$.
Once obtained the dependence from the incoming direction, the derivation of the number of events as a function of the galactic coordinates is straightforward:

$$\frac{d\bar{N}}{d\Omega}(l,b) = t \int d\bar{K}_\chi \frac{d\bar{\Phi}_\chi}{d\Omega}(l,b) A_{\text{eff}}^{DM}(\bar{K}_\chi). \tag{5.41}$$

In Figure 5.20, this number of attenuated events is shown, for the scalar case and incoming DM direction of $(l,b) = (0°, 0°)$; as benchmark parameters we have chosen $m_\phi = 1$ GeV, $m_\chi = 0.10$ GeV and $g_{u\phi}g_{\chi\phi} = 0.1$. Similarly for the pseudoscalar mediator, we have chosen the attenuated number of events, for a DM particle coming from the Galactic Center, with parameters $m_a = 1$ GeV, $m_\chi = 2.0$ GeV and $g_{ua}g_{\chi a} = 0.1$.
Only to give an idea of the importance of the attenuation of the expected number of events, the integrated values in the DM kinetic energy are shown in Tables 5.5 and 5.6.

| | *ELOWEN* | *GRECO* |
|---|---|---|
| Non Attenuated | $2.65 \times 10^7$ | $2.07 \times 10^4$ |
| Attenuated | $1.17 \times 10^7$ | $1.23 \times 10^4$ |

**Table 5.5.** Number of attenuated and non-attenuated expected DM events for both *ELOWEN* and *GRECO* event selection. These results are shown for the scalar case and for fixed parameters $m_\phi = 1$ GeV, $m_\chi = 0.10$ GeV and $g_{u\phi}g_{\chi\phi} = 0.1$

| | *ELOWEN* | *GRECO* |
|---|---|---|
| Non Attenuated | $4.97 \times 10^4$ | $7.60 \times 10^0$ |
| Attenuated | $2.23 \times 10^3$ | $7.56 \times 10^{-3}$ |

**Table 5.6.** Number of attenuated and non-attenuated expected DM events for both *ELOWEN* and *GRECO* event selection. These results are shown for the pseudoscalar case and for fixed parameters $m_a = 1$ GeV, $m_\chi = 2.0$ GeV and $g_{ua}g_{\chi a} = 0.1$.

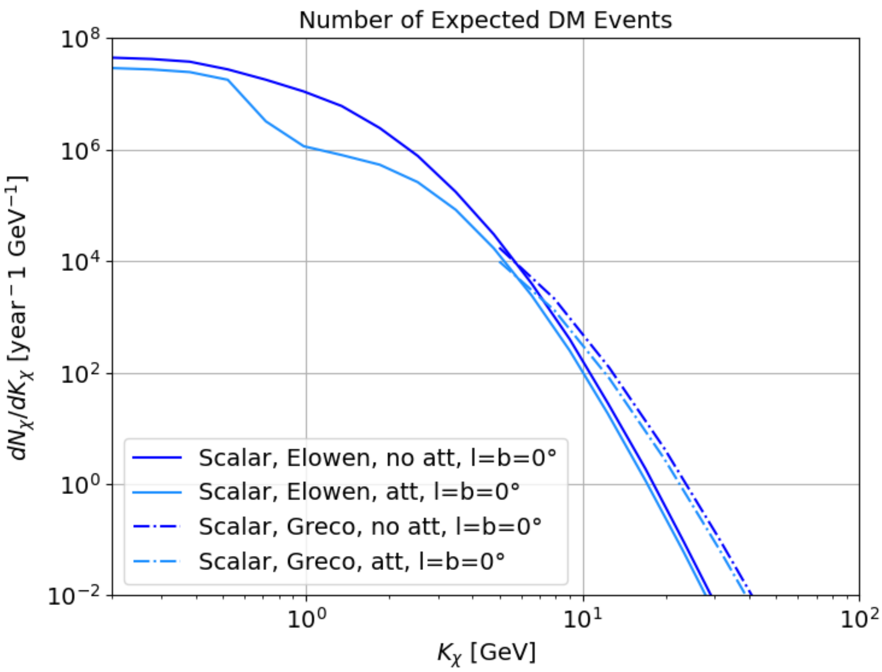


**Figure 5.20.** Number of expected DM events for the scalar mediator case, for *ELOWEN* and *GRECO* event selection. Both the non-attenuated and attenuated signal is shown, assuming that the DM particles are coming from the Galactic Center, for fixed parameters $m_\phi = 1$ GeV, $m_\chi = 0.10$ GeV and $g_{u\phi}g_{\chi\phi} = 0.1$.

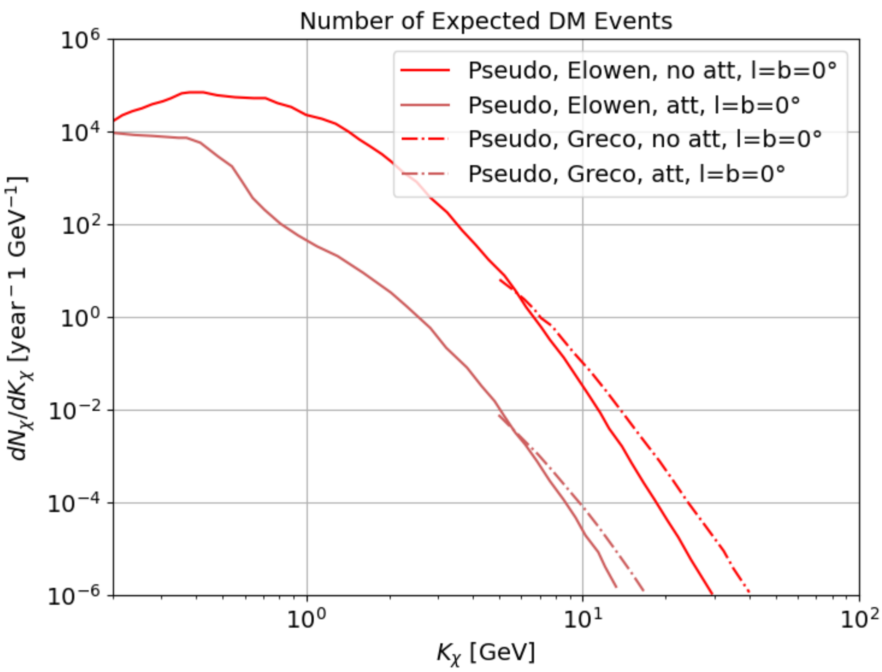


**Figure 5.21.** Number of expected DM events for the scalar mediator case, for *ELOWEN* and *GRECO* event selection. Both the non-attenuated and attenuated signal is shown, assuming that the DM particles are coming from the Galactic Center, for fixed parameters $m_a = 1$ GeV, $m_\chi = 2.0$ GeV and $g_{ua}g_{\chi a} = 0.1$.

## 5.3 Test Statistic definition

To discriminate between the signal hypothesis (backgorund + DM events) and the background-only hypothesis, a Test Statistic is defined. Given the number of expected events from the two event selections, we can perform a **binned likelihood analysis** of the number of events as a function of $(m_\chi, g_{u\phi}g_{\chi\phi})$ for the scalar mediator case or of $(m_\chi, g_{ua}g_{\chi a})$ for the pseudoscalar mediator case.

The Likelihood function measures how much the measured data, which are fixed, are compatible with a theoretical model, described by the variable parameter(s) $\vec{\theta}$ [128]:

$$\mathcal{L}(\theta) = P(\text{data}|\vec{\theta}) \tag{5.42}$$

In other words, $\mathcal{L}(\vec{\theta})$ is the probability of observed data as a function of the varying model parameter(s) $P(\text{data}|\vec{\theta})$, which differs from the usual definition of the probability, where the data vary while the parameter(s) $\vec{\theta}$ is fixed.

A Poisson distribution is chosen for the probability density function of the expected DM signal, as it is commonly used to model the expected number of rare and independent events in a fixed observation window, which is the case for possible DM events in detectors like IceCube. This distribution is parametrized as [128]:

$$\text{Poisson}(k;\lambda) = \frac{\lambda^k}{k!}\text{e}^{-\lambda}\,, \tag{5.43}$$

which models the probability of observing $k$ independent events in a fixed interval, given an expected number of events $\lambda$.

Regarding *ELOWEN* event selection, from which we obtain a sky-integrated signal, the Likelihood can be defined as[3]

$$\mathcal{L}(N^{\text{ELOWEN}}|B^{\text{ELOWEN}}, m_\chi, g) = \text{Poisson}(N^{\text{ELOWEN}}, B^{\text{ELOWEN}} + S^{\text{ELOWEN}}(m_\chi, g)); \tag{5.44}$$

similarly we can define the likelihood for *GRECO*, but in this second case we can consider the direction dependence of the signal. Therefore, we perform a binned analysis considering $N \times N$ bins in the $(l, b)$ parameter space. In this way, we get $N^2$ values for each $(m_\chi, g)$ couple, due to the direction dependence of the number of events.

To simplify the analysis, we consider *ELOWEN* and *GRECO* as independent samples; this is a reasonable assumption given the vastly different selection criteria. Defyning a common index between *ELOWEN* and *GRECO* contributions, $i = 1, ..., N^2 + 1$, the final form of the Likelihood is

$$\boxed{\mathcal{L}(\{N_i\}|\{B_i\}, m_\chi, g) = \prod_{i=1}^{N^2+1} \text{Poisson}(N_i, B_i + S_i(m_\chi, g))} \tag{5.45}$$

[3]In the following paragraphs, we refer to $g_{u\phi}g_{\chi\phi} = g_{ua}g_{\phi a}$ as $g$.

Finally, using the **frequentist approach**, we consider the minus log-Likelihood test statistic [128]

$$\begin{aligned}\text{TS}(m_\chi, g) &= 2\ln\frac{\mathcal{L}(N_j|\hat{m_j}, \hat{g}_j, \hat{B}_j)}{\mathcal{L}(N_j|m_\chi, g=0, B_\text{e})} \\ &= 2\ln\mathcal{L}(N_j|\hat{m_j}, \hat{g}_j, \hat{B}_j) - 2\ln\mathcal{L}(N_j|m_\chi, g=0, B_\text{e}),\end{aligned} \tag{5.46}$$

where $\hat{m_j}, \hat{g}_j, \hat{B}_j$ are the parameters that maximize Likelihood, while $\mathcal{L}(N_j|m_\chi, g = 0, B_\text{e})$ corresponds to the background only hypothesis, since in our model $g = 0$ means absence of signal.

Notice that, in general, $\hat{B}_j \neq B_\text{e}$ because the likelihood must be maximized in both cases. While background estimates are typically performed for all selections, in our analysis, we leave the *ELOWEN* background as a free parameter, since its signal region covers the full sky, and keep the *GRECO* background fixed. This choice is due to a simple consideration:

- ***ELOWEN* background**: is integrated in all-sky and we don't have information about the direction (in principle, we could have an excess from the galactic center that we are not able to see), hence it must be considered as a parameter in the maximization of the likelihood. Therefore $B_\text{e}$ is left free, the only condition that we have on it is $B_\text{e} \in [0, B_\text{e}^\text{nominal}]$, where $B_\text{e}^\text{nominal} = 0.021$ Hz.

- ***GRECO* background**: the event rate in *GRECO* does not show significant anisotropies in the sky coordinates, therefore it is safe to assume that the contribution of a galactic signal does not affect the average rates used as background.

### 5.3.1 Signal definition

Once the test statistic is defined, we must specify the signal and background models. In the case of the *GRECO* analysis, we adopt a $9 \times 9$ binning scheme in galactic coordinates. The signal is defined as follows:

- for the *ELOWEN* event selection, a single all-sky integrated value is considered;

- while for the *GRECO* event selection, a two-dimensional histogram with $81$ bins is considered.

Therefore, to get the value of the Test Statistic for each $(m_\chi, g)$ pair, the first step is to define the signal. What we obtain for *ELOWEN* is the number of events integrated in the full sky, defined as $S^\text{ELOWEN}$; for *GRECO*, we get a $2D$-histogram in the $(l, b)$ plane, with $N^2$ bins. This implies that for *GRECO* we get $N^2$-values for the number of events, that we define $\{S_i^\text{GRECO}\}_{i=1,...,N^2}$.
Combining *ELOWEN* and *GRECO* event selections, we obtain $N + 1$ values for the expected signal; in our analysis, we have chosen $N = 9$ (hence $i = 1, ..., 82$).
This binning choice is due to two reasons: first, an odd number of bins has been chosen to have the Galactic Center in the middle of a bin. Secondly, we have chosen a large enough bin size to not be sensitive to possible smearing of the signal due to *GRECO*

angular resolution, which in the energy range of our interest is approximately $30°$ [122].

In conclusion, for each $(m_\chi, g)$ pair, we get 82 signal values:

$$\begin{aligned} S^{\text{ELOWEN}}(m_\chi, g) &= \int A^{\text{DM}}_{\text{eff, ELOWEN}}(E_\chi, m_\chi, g) \cdot \Phi_\chi(E_\chi, m_\chi, g) dE_\chi, \\ S_i^{\text{GRECO}}(m_\chi, g, l, b) &= \int A^{\text{DM}}_{\text{eff, ELOWEN}}(E_\chi, m_\chi, g) \cdot \frac{d\Phi_\chi}{d\Omega}(E_\chi, m_\chi, g, l, b) dE_\chi. \end{aligned} \tag{5.47}$$

In Figure 5.24 we represent the histogram of number of expected events for *GRECO* event selection, for the benchmark parameters $m_\chi = 0.01$ GeV, $m_a = 1$ GeV and $g_{ua} g_{\chi a} = 0.1$. This histogram is plotted in the $(l, \sin b)$ plane since the differential in the solid angle is $d\Omega = \cos(b) dl db = dl d(\sin b)$.

### 5.3.2 Background definition

Now, the only missing point to obtain the Test Statistic is the background rate.
Considering *ELOWEN* selection criteria, the background is considered as constant in the sky-direction, and it's given by $B_{\text{e}} \sim 0.021$ Hz.
Regarding *GRECO* event selection, the background rate is a function of the zenith angle [123]; in Figure 5.22 we report the background rate distribution as a function of the zenith.

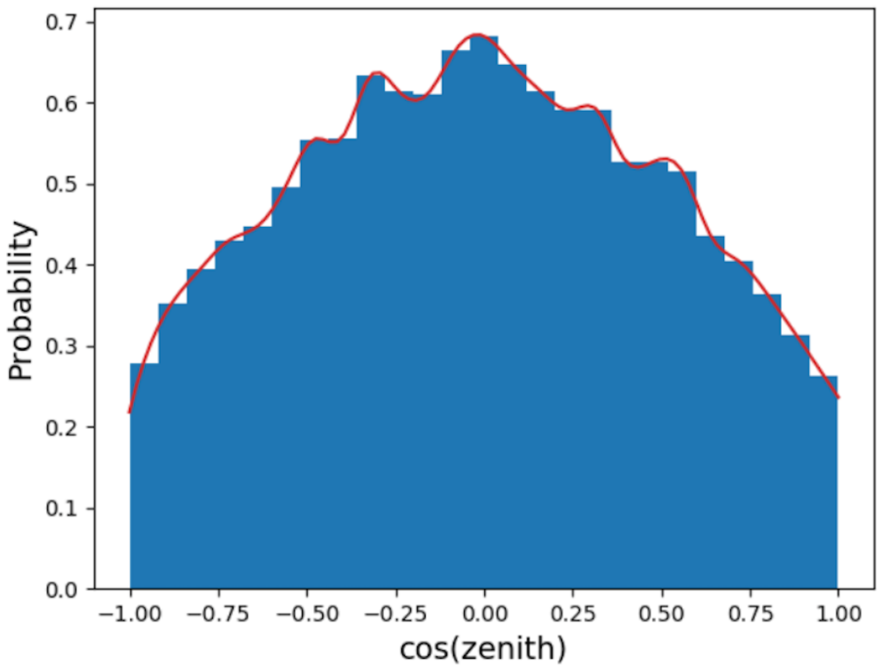


**Figure 5.22.** Background event distribution as a function of cos(zenith), derived from data, with a spline used for the background PDF in red. Both the histogram and the background fit are taken from [123].

This background must be normalized at the total background rate $4.6$ mHz $= 1.5 \times 10^5$ year$^{-1}$ [123]; to get the *GRECO* background distribution in the galactic coordinates, we have to consider the dependence of the zenith angle from the galactic coordinates $\theta(l, b)$. In this way, we can obtain the *GRECO* background distribution in the galactic coordinates; this is shown in Figure 5.23. As we can see, the maximum of the background is the yellow-band, which in the IceCube reference frame represents the horizon ($\cos\theta = 0 \rightarrow \theta = 90°$), while the minimum of the background is in correspondence of the two poles ($\cos\theta = \pm 1 \rightarrow \theta = 0°, 180°$), namely strictly down-going or up-going events.

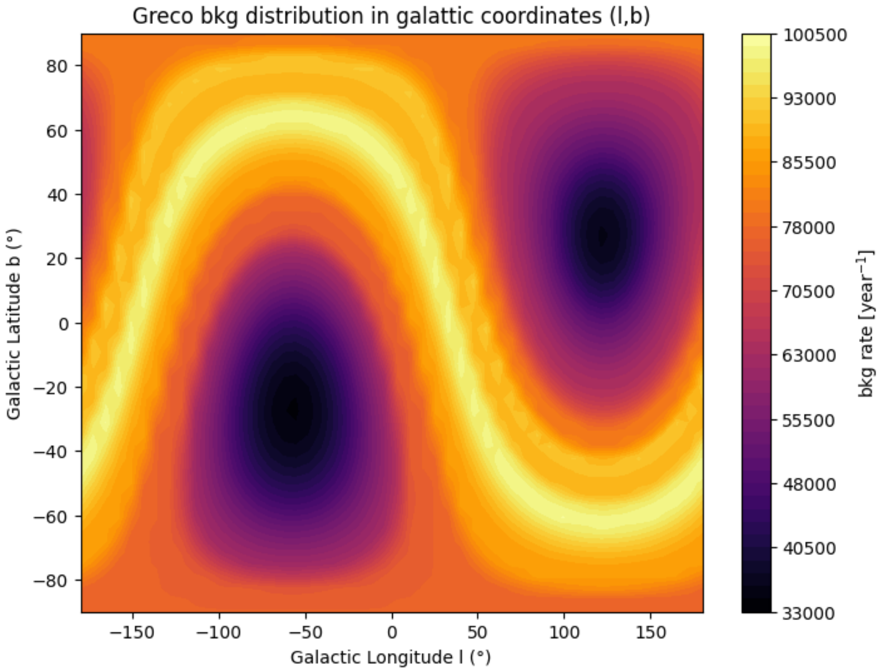


**Figure 5.23.** *GRECO* background rate as a function of galactic coordinates. I have produced this background distribution in the galactic coordinates starting from Figure 5.22.

Finally, in Figure 5.25 the histogram obtained from this background is shown; this is the background which is compared with the signal histogram of Figure 5.24 in the TS definition.

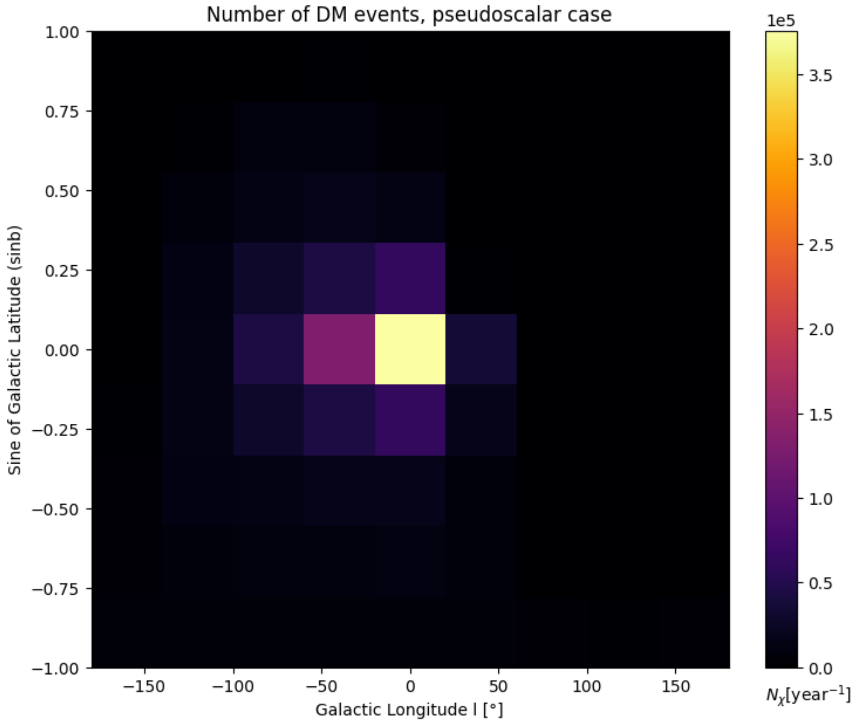


**Figure 5.24.** Two-dimensional histogram of the expected number of dark matter events in galactic coordinates, corresponding to the *GRECO* event selection and computed for the pseudoscalar-mediated interaction with parameters $m_\chi = 0.01$ GeV, $m_a = 1$ GeV and $g_{ua}g_{\chi a} = 0.1$.

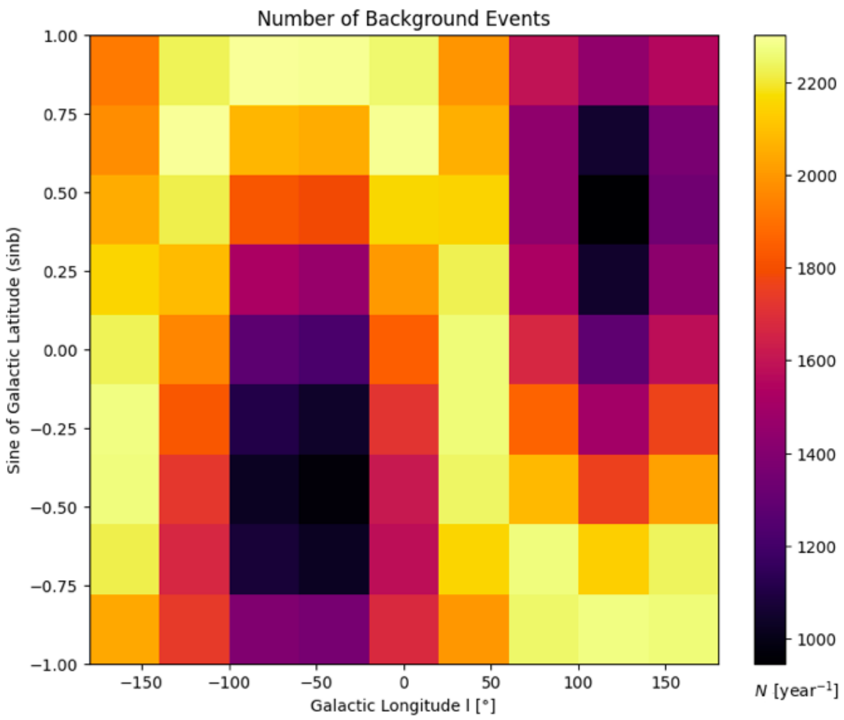


**Figure 5.25.** Two-dimensional histogram of the number of background events in galactic coordinates, corresponding to the *GRECO* event selection.

### 5.3.3 Likelihood maximization and TS Distributions

Finally, to get the Test Statistic value, we should maximize the likelihood or minimize the minus log-likelihood. We choose this second option, since in this way we can use the Python function *scipy.optimize.minimize* to minimize minus log-likelihood.
To perform this minimization, we consider a four-steps procedure, as described in the following:

- first we evaluate the likelihood for a given mass $m_1$, hence we get $\mathcal{L}(N_j|m_1, g, B_\text{e}) = f_1(g, B_\text{e})$;
- secondly, we get $x_1$, the minimum of the minus log-Likelihood for a given mass $m_1$;
- then we repeat steps 1 and 2 for all the $50$ values of the DM mass;
- finally we get $x_\text{max}$ , the minimum of $x_i$ for $i = 1, ..., 50$. This is the maximum of the Likelihood in the three parameters $(m_\chi, g, B_\text{e})$.

Then, to get the TS denominator, we simply compute $\mathcal{L}(N_j|g = 0, B_\text{e})$ where $B_\text{e} = \min\{N_\text{e}, B_\text{e}^\text{nominal}\}$.

This procedure returns us the value of the TS for a given ***pseudo-experiment***, in which $N_i$ is randomly sampled from a Poissonian distribution, $N_i \sim$ Poissonian$(Bi + Si)$, for a given $(m_\chi, g)$ pair. Then, for each pair, we have to define the TS distribution; hence we perform a given number of pseudo-experiments, we get the TS for each of them and finally we record in an histogram the number of occurrence for which the test statistic gets a given value. What changes in the different pseudo-experiments is $N_i$, since is given by the Poissonian, which changes in all of them. We consider, for a first analysis, a thousand pseudo-experiments. In this way, we get the TS distribution for a given $(m_\chi, g)$ pair.

Finally, to define the sensitivity in the $(m_\chi, g)$ plane, we need to obtain the TS distributions for several $(m_\chi, g)$ pairs and to confront them with the background TS distribution. To get the background TS distribution, the only thing that changes respect to the signal TS distributions is $N_i \sim$ Poissonian$(B_i)$.

In this way, we get the *background TS distribution* and one *signal TS distribution* for each $(m_\chi, g)$ pair. In the Figure 5.26, we have reported a draft of what we expect regarding the TS distributions: in black the background TS distribution, in green the signal TS distribution for a given pair $(m_1, g_1)$ and in blue for $(m_2, g_2)$ with $g_2 > g_1$; if the coupling increases, we expect that the distribution shifts to the right.

Finally, to improve our sensitivity, we can also consider that IceCube has recorded more than 13 years of data; therefore, if we define the *livetime* $\tau$ as the time in which the detector has been able to collected data, we can repeat the previous analysis considering $N_i \sim$ Poissonian$(\tau \cdot (Bi + Si))$.

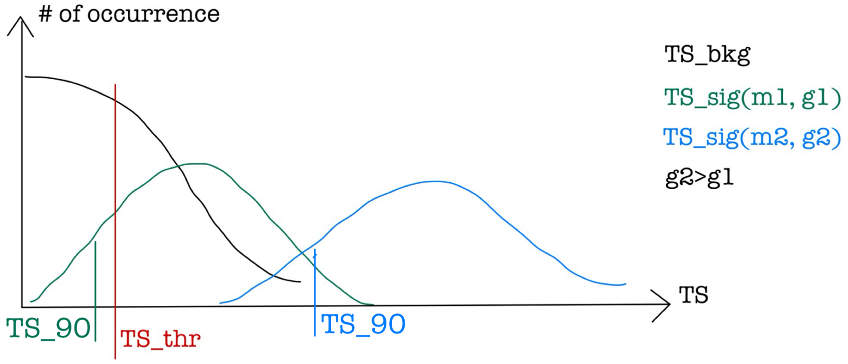


**Figure 5.26.** Draft of the expected background (in black) and signal (in green and blue) TS distributions.

### 5.3.4 Sensitivity in the $(m_\chi, g)$ plane

Finally, to obtain the sensitivity plots, we have to confront the signal TS distributions with the median of the background one $\text{TS}_{\text{thr}} = \text{median}(P_{\text{bkg}})$.

To perform this comparison, we consider, for each $(m_\chi, g)$ pair of the parameter space, $\text{TS}_{90}$, defined as the TS value for which the $90\%$ of the distribution lies above it.
Then, if $\text{TS}_{90}$ is above $\text{TS}_{\text{thr}}$, this pair of parameters $(m_\chi, g)$ is considered in the contour, since the signal TS distribution is well separated from the background one (as the blue distribution in Figure 5.26). On the other side, if $\text{TS}_{90}$ is below $\text{TS}_{\text{thr}}$, this pair of parameters $(m_\chi, g)$ is not considered in the contour, since the signal TS distribution is superimposed to the background one and therefore we cannot discriminate between them (as the green distribution in Figure 5.26). To conclude, we can easily obtain the $90\%$ contour plot by repeating this procedure for all the $(m_\chi, g)$ pairs of the parameters' plane.

## 5.4 Analysis' Results

The analysis's goal is to obtain the sensitivity of IceCube to CR-upscattered sub-GeV DM, as a function of the DM parameters $(m_\chi, g)$.
The starting point of this analysis is the computation of the number of expected DM events at IceCube, as a function of the DM mass and of the coupling. This computation has been introduced in Section 5.2.2.
An example of the number of expected DM events at IceCube, for the scalar case with a mediator mass of $3$ GeV and the *ELOWEN* event selection is shown in Figure 5.27.

As shown in this figure, the interpolator we designed to reproduce the expected number of events exhibits some fluctuations. These are likely due to the choice of using a numerical integration method in order to optimize performance.
In an attempt to understand the origin of these fluctuations, I also implemented the

analytical integration of the differential event rate[4].
From the comparison between the two integration methods, I found that the fluctuations observed in the figure correspond to underestimations of the signal. The analytical integration yields higher values, confirming that the numerical method tends to suppress the signal. Therefore, this bias does not lead to the inclusion of points in IceCube's sensitivity contour that should be excluded. On the contrary, it may cause the exclusion of points that, with a more accurate analysis, would lie within the sensitivity region.

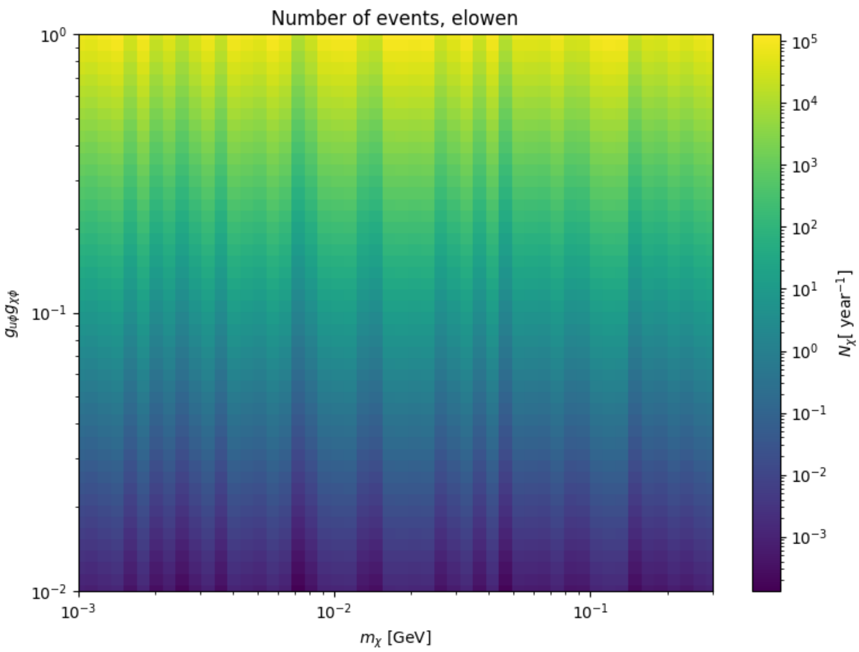


**Figure 5.27.** Number of expected DM events at IceCube, as a function of the DM mass and of the coupling; these results have been obtained considering *ELOWEN* event selection, for the scalar mediator with $m_\phi$=3 GeV.

### 5.4.1 Considerations about the Test Statistic Distributions

In Section 5.3.3, we have defined how to derive the Test Statistic distribution. The signal TS distributions have to be compared with the background TS distribution, which is represented in Figure 5.28.
From this distribution, we can derive the median of the background TS$_{\text{thr}}$ $= 0.27$, which can be considered as a reference limit to compare between background-only and signal hypotheses.

In the following, we present some plots to show how this TS distribution behaves as a function of the parameters of the model.
Only as an example, we consider a DM-SM interaction, mediated by a scalar particle with mass $m_\phi = 1$ GeV; furthermore, similar results are also obtained for the

[4] This code is extremely slow and thus not feasible for scanning the entire parameter space. However, it provides a useful benchmark for selected $(m_\chi, g)$ values.

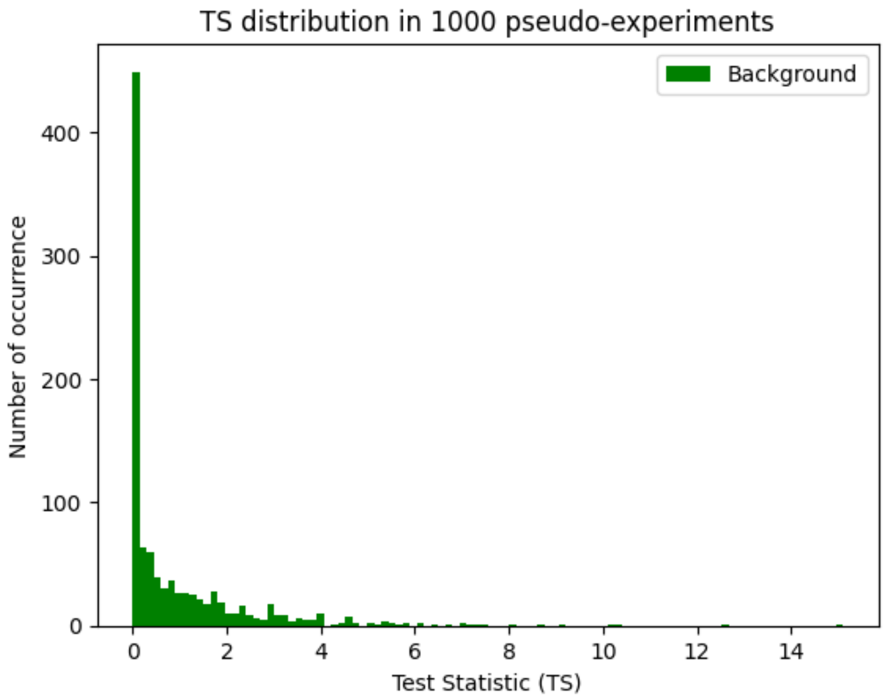


**Figure 5.28.** Test Statistic distribution for the background-only hypothesis.

pseudoscalar case, for different values of the mediator's mass. The TS distribution, of course, depends both on the DM mass and on the coupling, as shown respectively in Figures 5.29 and 5.30.
In these plots, the background TS distribution is shown as a comparison; to improve the readability of the plot, the background distribution is cut, even if the number of occurrences in the first bin is, for this distribution $449$. This cut will be applied in all the following plots.

As one can see, in Figure 5.29, the TS distribution has changed, both in shape and median value, for different DM masses. The behaviour of the TS distribution is non-monotonic with respect to the DM mass. This could be due to underfluctuations in the signal interpolator, which are evident in the Figure 5.27; therefore, an improved definition of the interpolator is needed to perform a more accurate analysis and to better understand the behavior of TS distributions for different DM masses.
On the other side, in Figure 5.30, is evident that, at the increase of the coupling, the TS distribution is shifted to higher values.

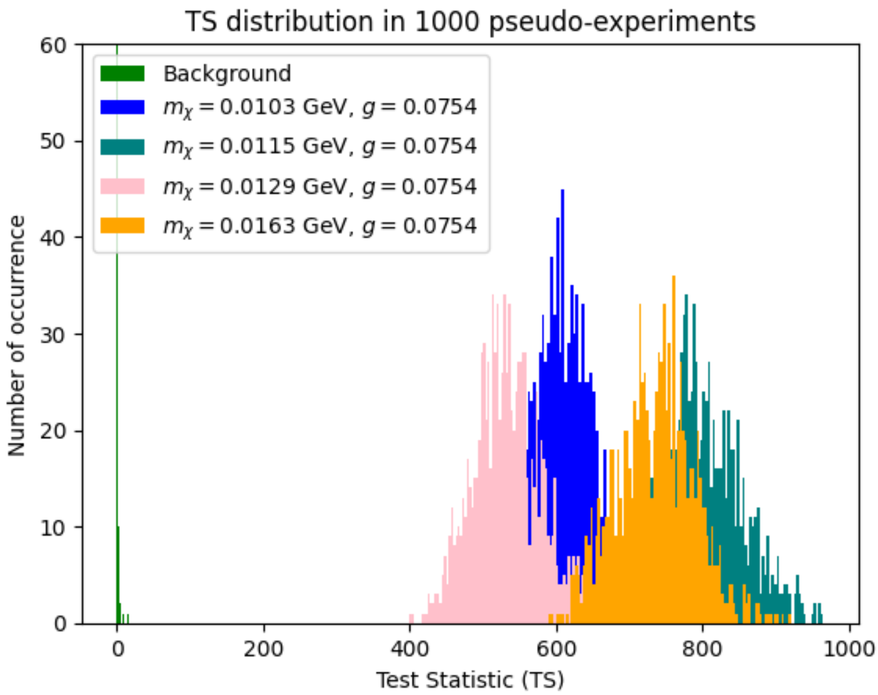


**Figure 5.29.** Test Statistic distribution for $m_\phi = 1$ GeV, coupling $g_{u\phi}g_{\chi\phi} = 0.0754$ and several values of the DM mass.

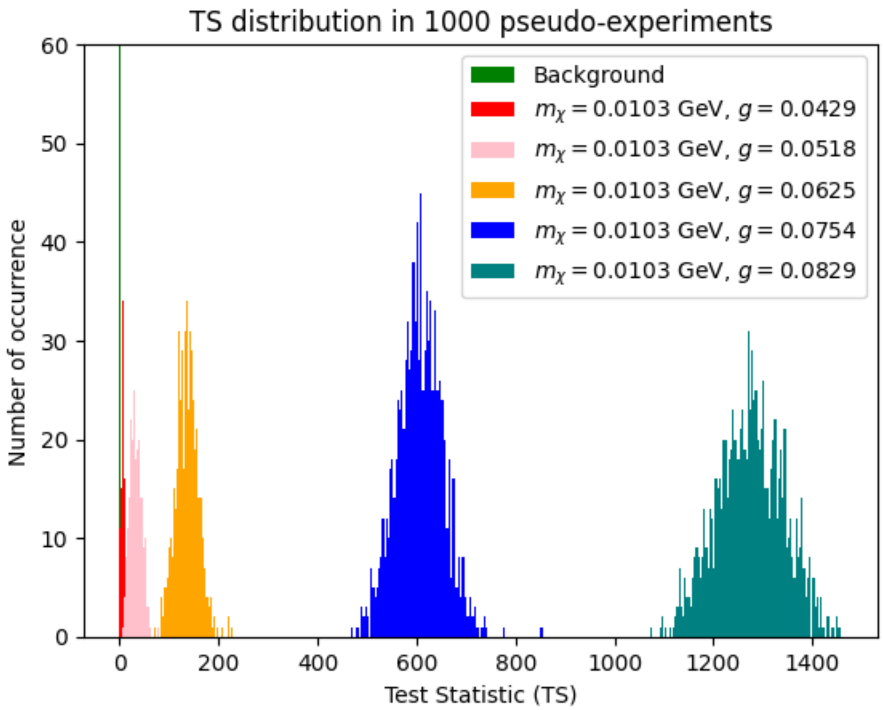


**Figure 5.30.** Test Statistic distribution for $m_\phi = 1$ GeV, DM mass $m_\chi = 0.0103$ GeV and several values of the DM-SM coupling.

### 5.4.2 Consideration about the Livetime

All the previous results have been obtained considering a livetime of $13$ years. A larger livetime, in any case, provides an improvement in the analysis, since the discriminating power between signal and background is increased.
An example of this effect is shown in Figure 5.31, where the same TS distribution is obtained for 1 year and 13 years of livetime; in this figure, we have fixed parameters as $m_\phi = 1$ GeV, $m_\chi = 0.01$ GeV and $g_{u\phi}g_{\chi\phi} = 0.05$.

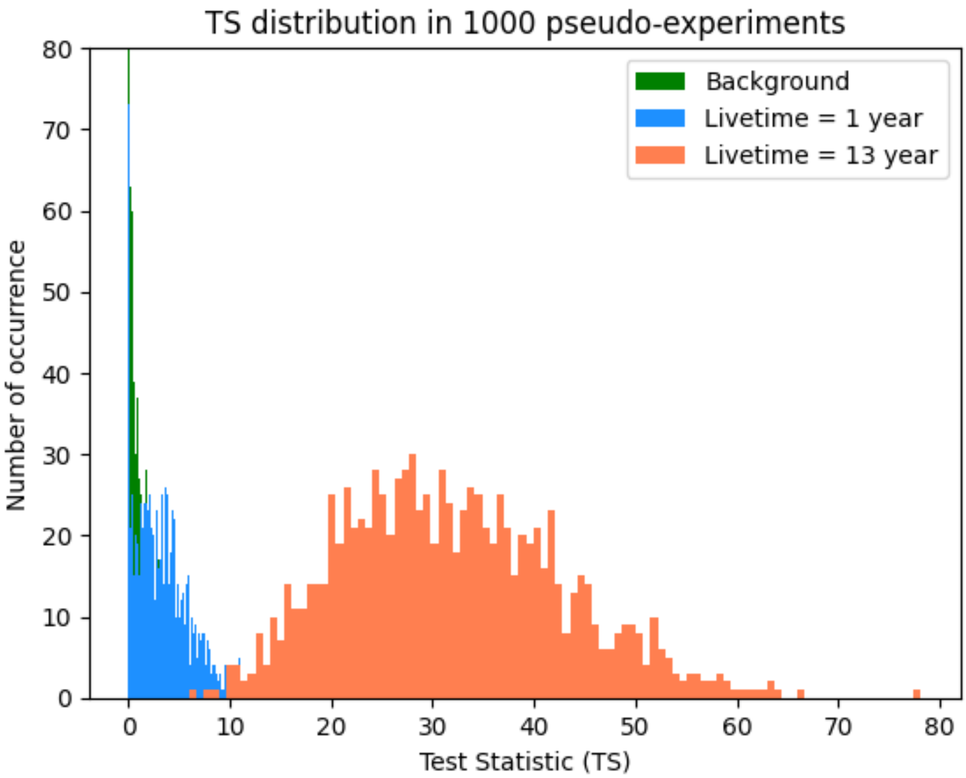


**Figure 5.31.** Test Statistic distribution for the scalar mediator case, with $m_\phi = 1$ GeV, $m_\chi = 0.0103$ GeV, $g_{u\phi}g_{\chi\phi} = 0.0518$. These two distributions are produced for two different livetimes: in purple 1 year and in teal 13 years; as expected, the distribution is shifted to the right at the increase of the livetime, increasing our discrimination power.

### 5.4.3 Consideration about Ice Attenuation

As introduced in Section 5.2.3, while DM particles travel before reaching the detector, they cross a given amount of matter and therefore the flux is attenuated. In Figures 5.20 and 5.21, the effects of this attenuation on the number of expected events is shown.
Regarding the computation of the TS distribution, we have chosen, only for the attenuated flux, to consider only the component coming from the galactic center, since the NFW distribution is strongly peaked in it[5].

[5]This approximation was introduced to improve the code's efficiency. Nevertheless, I also implemented the full analytical computation of the attenuated number of events, which converges to the

The distance travelled by particles coming from this direction is approximately $z = 5.16$ km and this path is all inside Antarctic ice; therefore, the attenuation of the DM flux coming from the Galactic Center is only due to ice.

### 5.4.4 Sensitivity Plots

The final goal of my analysis is to obtain the sensitivities for direct searches of Dark Matter using IceCube Neutrino Telescope.
To obtain them, I have considered the Test Statistic distributions for signal and background-only hypotheses, which enables us to discriminate between them.

As previously mentioned, the attenuation effect due to the Antarctic ice was approximated by considering only the DM flux coming from the Galactic center. First, I produced the contour plot for the non-attenuated analysis. Then, I reproduced the TS distribution for the attenuated signal at selected pairs in the parameter space, to identify which points included in the non-attenuated contour are excluded in the attenuated one.

In the following, these contour plots are presented; for all the graphs shown, the following elements are included:

- **IceCube sensitivity** (green line): this is the contour plot obtained by the analysis described in this work, neglecting Earth and ice attenuation;
- **Attenuation-selected points** (green dots): also these points have been obtained in my work, by considering ice attenuation under the simplifying approximations described before. These are the points which are included in the contour also considering the attenuation of the flux;
- **Attenuation-excluded points** (orange dots): as the ones of before, they are obtained considering flux attenuation, but in this case these parameters' pairs are excluded by the contour;
- **Other limits** (pink, gray, brown): these limits are shown as a comparison, in order to compare our results with the other known in literature; they have been obtained by [6];
- **Super-Kamiokande sensitivity** (light-blue): as a comparison, I show also the sensitivity limit obtained in Ref. [6] for Super-Kamiokande Neutrino Telescope.

In Figures 5.32 and 5.33, we show the contour plots for the scalar mediator case, for two values of the mediator mass: $m_\phi = 1$ GeV and $m_\phi = 3$ GeV.
Finally, in Figures 5.34 and 5.35, we show the contour plots for the pseudoscalar mediator case, for two values of the mediator mass: $m_a = 1$ GeV and $m_a = 3$ GeV.

approximate result in the direction of the Galactic Center.

As shown in these plots, the study of the attenuated flux, although approximate and limited to a subset of the parameter space, provides valuable insights into IceCube's sensitivity. In particular, the excluded orange points indicate that, for higher values of the DM–SM coupling, the sensitivity is entirely lost. This occurs because, with stronger couplings, DM particles are more likely to interact with the medium in which they travel before reaching the detector, causing them to be either stopped or significantly slowed down, and making them undetectable.
This effect is most evident in Figure 5.34, where the overall behavior is consistent with the results of Ref. [6].

As a final result of the analysis, we can now compare IceCube sensitivities with other existing constraints. In the scalar case, for both $m_\phi = 1$ GeV and $m_\phi = 3$ GeV, we are not able to probe regions allowed by other constraints. Therefore, IceCube's sensitivity remains lower compared to other types of searches.
On the contrary, for the pseudoscalar case, for both $m_a = 1$ GeV and $m_a = 3$ GeV, IceCube's sensitivity lies, even if slightly, within a region allowed by all existing constraints. This is very encouraging, especially considering that the analysis has been conservative. It can be significantly improved by taking into account key aspects, such as the dependence of the effective area on the sky direction. Additionally, we can relax some of the approximations made regarding the attenuated flux, which was underestimated in this work.
To conclude, the results obtained for the pseudoscalar mediator motivate a more refined analysis with the IceCube Collaboration.

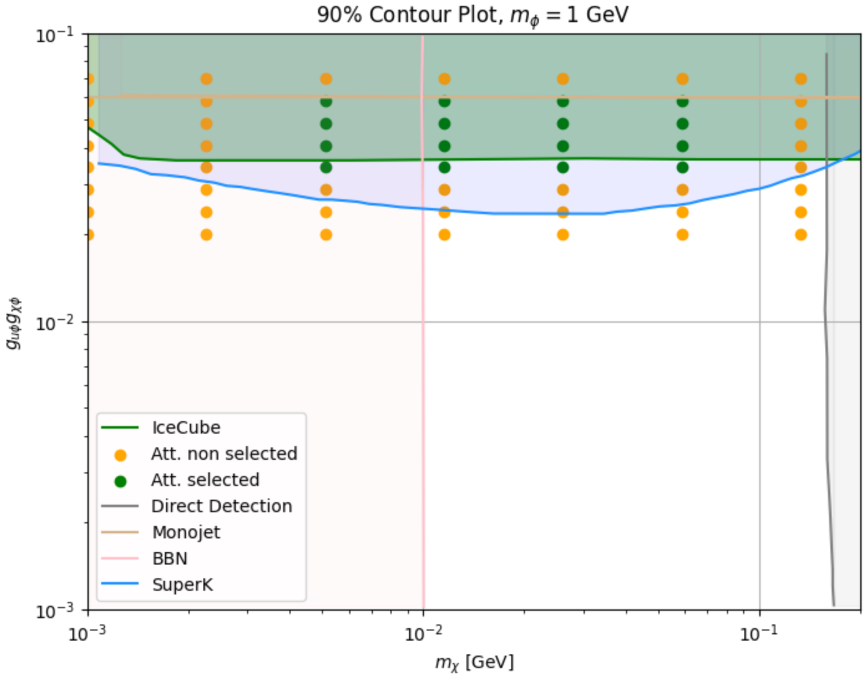


**Figure 5.32.** $90\%$ Contour plot in the plane of couplings vs DM mass, for the scalar mediator of mass $m_\phi = 1$ GeV. With the green line we represent the IceCube's sensitivity neglecting Earth and Ice attenuation; finally, with green dots, we represent the points of the parameter space which survive the selection also in the assumption of attenuated DM flux.

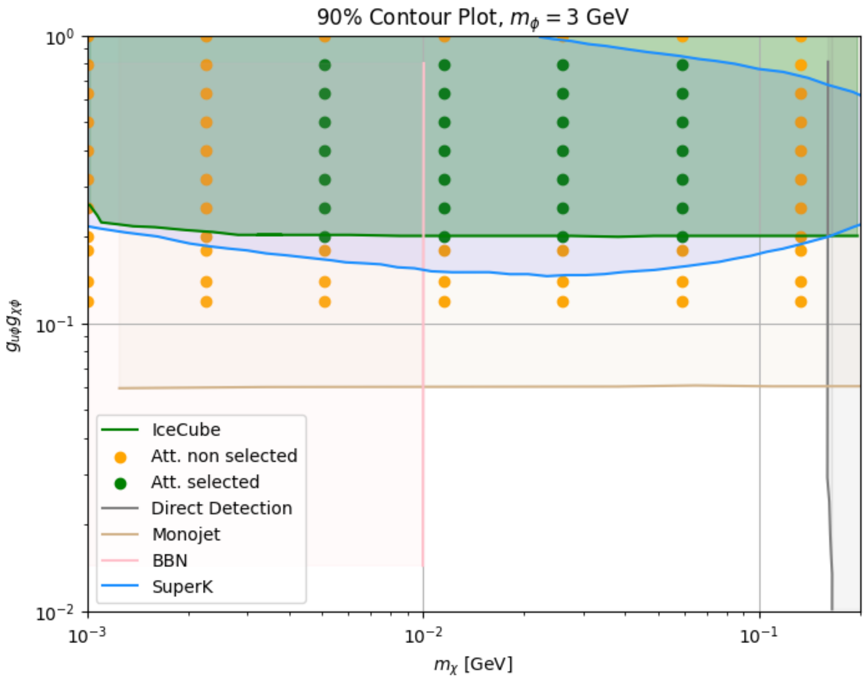


**Figure 5.33.** $90\%$ Contour plot in the plane of couplings vs DM mass, for the scalar mediator of mass $m_\phi = 3$ GeV. With the green line we represent the IceCube's sensitivity neglecting Earth and Ice attenuation; finally, with green dots, we represent the points of the parameter space which survive the selection also in the assumption of attenuated DM flux.

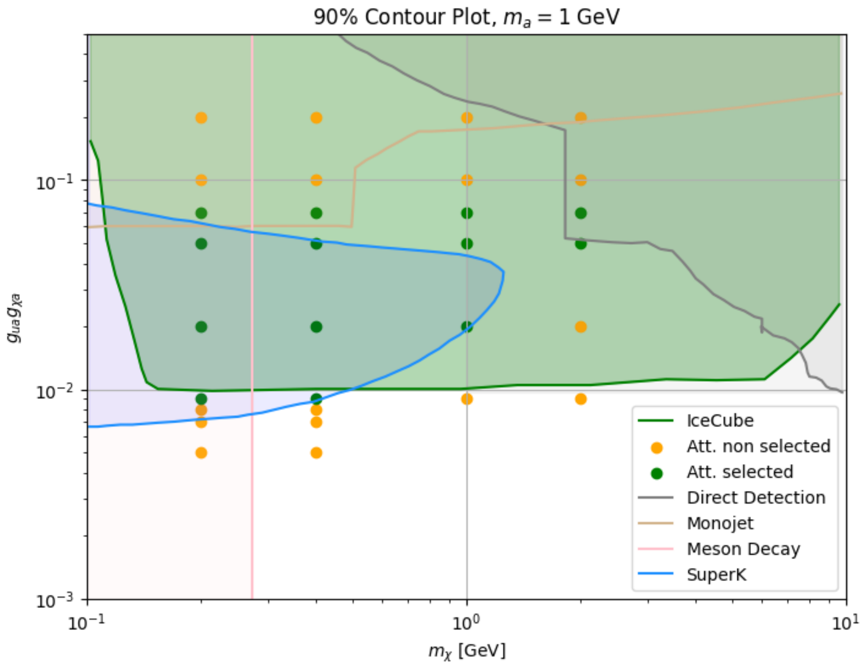


**Figure 5.34.** $90\%$ Contour plot in the plane of couplings vs DM mass, for the pseudoscalar mediator of mass $m_a = 1$ GeV. With the green line we represent the IceCube's sensitivity neglecting Earth and Ice attenuation; finally, with green dots, we represent the points of the parameter space which survive the selection also in the assumption of attenuated DM flux.

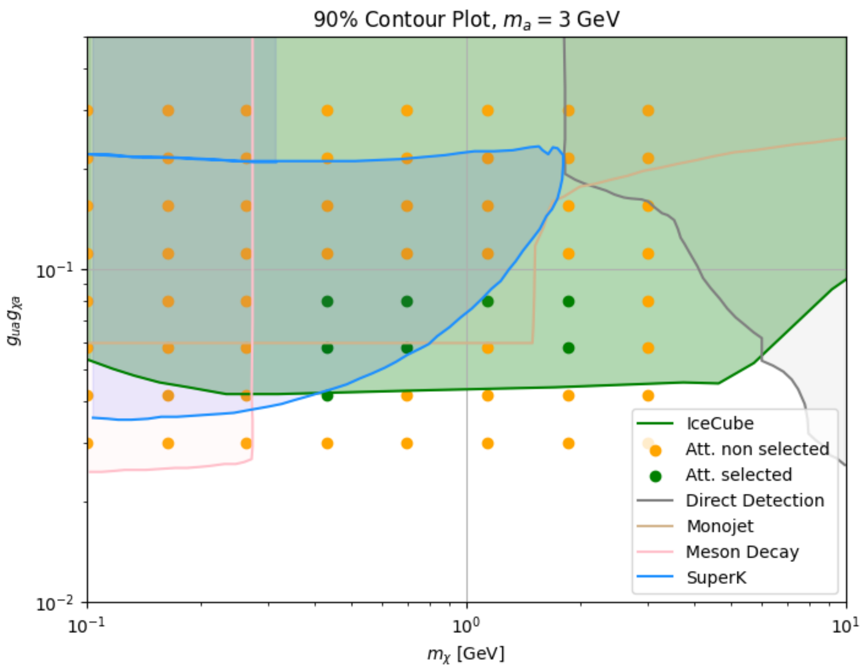


**Figure 5.35.** $90\%$ Contour plot in the plane of couplings vs DM mass, for the pseudoscalar mediator of mass $m_a = 3$ GeV. With the green line we represent the IceCube's sensitivity neglecting Earth and Ice attenuation; finally, with green dots, we represent the points of the parameter space which survive the selection also in the assumption of attenuated DM flux.

# CHAPTER 6

# Conclusions and Outlook

In this study, we have performed the first exploratory determination of IceCube's sensitivity to direct detection of sub-GeV DM, a topic that is attracting increasing interest in the community.
This analysis focuses on a specific DM candidate: light and hadrophilic. The study relies on the CR-upscattered flux of sub-GeV DM, which is inevitably produced once one assumes that DM couples to hadrons, the same assumption underlying all direct detection experiments such as XENONnT and similar.
This candidate is gaining increasing attention, but due to kinematic constraints, it is difficult to probe with direct detection experiments. For this reason, we performed a sensitivity study of the IceCube detector, a neutrino telescope sensitive to energies in the GeV range, where upscattered DM fluxes are expected to peak. Moreover, IceCube is currently the largest neutrino telescope, which enhances the chances of observing rare events such as DM interactions within the detector.

Before summarizing the main results of this thesis, we briefly outline its main topics. Chapter 1 introduces the main motivations at the basis of this study. In Chapter 2 we have summarized the current status of our knowledge about DM, starting from its observational evidence, continuing with its main properties, mass distributions and candidates. Furthermore, a particular focus is given on the sub-GeV DM candidate, which are the ones used in this study. Next, in Chapter 3, a review of the neutrino detection through Cherenkov radiation is presented. Since the neutrino telescope used in this analysis is IceCube, in Chapter 4 the main features of this experiment are discussed, with a focus on the aspects relevant for our study: noise and backgrounds, *ELOWEN* and *GRECO* event selections, the ones used in this study. Lastly, in Chapter 5, we have described the analysis procedure implemented to obtain the new IceCube sensitivities to sub-GeV Dark Matter.

Regarding the analysis method, the starting point is the DM upscattered flux, which has been derived as described in Ref. [6], with small variations in the results due to the update of the CRs spectra (see section 5.2.1). Unlike the flux computation, the calculation of the expected number of DM events at IceCube was performed using a new methodology. Starting from the known response of the detector to neutrinos, we obtained the DM effective area, which allowed us to compute the number of expected

DM events in the IceCube detector (see Section 5.2.2). This value depends on a set of three parameters: the DM mass, the mediator mass, and the coupling between SM and DM particles.
By performing an analysis based on the definition of a test statistic (see Section 5.3), we have been able to distinguish between the background-only and signal hypotheses and draw, for several values of the parameters, the corresponding contour plot (see Section 5.3.4).
As shown in the final contour plots (Figures 5.32, 5.33, 5.34, 5.35), the results are close to those obtained for Super-Kamiokande, which gives encouraging prospects for continuing this study with a more detailed analysis.

We finally outline several aspects that could be explored to improve the analysis in future work:

- **Better determination of the number of expected events**: as shown in Figure 5.27, the signal interpolator used for the analysis produces some under-fluctuations, which give rise to a lower number of expected events. Therefore, an analysis performed using an interpolator which has not these fluctuations, such as the analytical code used to test some notable values of the parameters space, would be able to improve our sensitivity.

- **Noise reduction**: as widely presented in other studies, as in Ref. [100], the noise in IceCube detector is made by several components. Since the expected DM signal follows a Poisson distribution, as it consists of rare and independent events occurring with a low probability over a fixed observation period, depending on the shape of the noise distribution we can remove some noise components;

- **Directionality of the signal**: as introduced in Chapter 5 and well visible, for instance, in Figure 5.4, the studied DM flux is expected to be peaked at the Galactic Center. Using *GRECO* event selection, this directionality information has been partially considered, since we have cut a region of sky in which we do not expect signal (for declination greater than $-5$); furthermore, thanks to the different behavior in the galactic coordinates between signal and background (as visible in Figures 5.23 and 5.18), we have been able to perform a binned likelihood analysis, which has increase our discrimination power. Nevertheless, a significant improvement to our analysis could come from the use of direction-dependent effective areas for neutrinos. Since our DM signal is strongly peaked towards the Galactic Center, this could lead to a substantial enhancement in the sensitivity of the analysis;

- **Discriminate between different kinds of interactions**: in the definition of the DM effective area, we have considered the public neutrino effective areas, which are the total ones; hence, we have considered both charged-current and neutral-current interactions inside the detector. Moreover, our DM candidate is a neutral particle, both respecting electromagnetic and weak interactions; therefore, we expect only a Neutral Current signal induced in the detector by a DM particle. Thus, another step in the analysis's improvement is to discriminate between these two kinds of events, selecting only the Neutral Current neutrino effective area.

- **Implement Earth and Ice Attenuation more specifically**: as introduced in Section 5.4.3, the attenuated flux considered in this work is only the one coming from the Galactic Center. This approximation has been chosen as a first estimation of the attenuated signal; moreover, a deeper study including the attenuated flux from a wider sky-direction would increase the expected signal and therefore improve our sensitivity.

# Acknowledgement

At the end of this thesis, I would like to thank the people who have supported and accompanied me throughout this journey. First and foremost, I would like to express my sincere gratitude to my supervisor, Professor Filippo Sala, for giving me the opportunity to work with him and to embark on such an exciting and stimulating project.
I would also like to warmly thank Professor Gwenhaël de Wasseige for welcoming me with great enthusiasm and genuine kindness into the Astro-CP3 group, making me feel part of it from the very beginning.
I am truly grateful to both of you for everything you have taught me, for the care you have taken in guiding me, and for the time you have dedicated to me; it has been incredibly valuable.

I would also like to thank the colleagues of the Astro-CP3 group, who have proven to be much more than just colleagues. A special thanks goes to Jonathan Mauro and Mathieu Lamoureux, who played a key role in the development of my analysis, always willing to share their time and offer valuable advice.
I am also grateful for meeting my office mates and the larger CP3 group. Thanks to you, I have learned so much and I was truly surprised by your generosity and willingness to help. I am also thankful for the evenings spent playing board games, our lunch and coffee breaks, which made me feel at home. Thanks to you and your example, I had a taste of what it means to do research, and it truly feels like one of the most beautiful things in the world.

I would also like to thank those who have been by my side since before this project began and have always supported me.
To my parents and my family, who have always encouraged my passion for learning and have shown genuine interest in what I do, thank you.
To my friends, for the thoughtless moments we've shared, for letting me share so many joys with you, and for supporting me through the tougher times, thank you.
To Giuseppe, who, more than anyone else, has experienced both the highs and lows of this journey. Thank you for always choosing to stand by me, whether it was to celebrate a success or to forget a bad day.

Finally, I would like to thank the One who instilled in me this deep passion for studying the Universe He created. I cannot help but recognize how fortunate I am and how many opportunities I have been given.

# Appendices

# Appendix A

# Derivation of useful Kinematical Quantities

In this Appendix we derive the Mandelstam variables $s$ and $t$ for a two-body collision between a CRs particle $A$ and a DM particle $\chi$ (assumed at rest, since compared to CRs velocities, DM can be considered at rest). The definition of these quantities will be the same also in the study of the DM interaction inside the detector, but in this second case we have that the DM particle is in motion and the detector target particles (that we assume only protons) are initially at rest.

The initial four-momenta are denoted by:

$$\begin{aligned} &p_A = (E_A, \vec{p}_A), \quad m_A^2 = E_A^2 - |\vec{p}_A|^2, \\ &p_\chi = (m_\chi, \vec{0}), \end{aligned} \tag{A.1}$$

where $m_A$ and $m_\chi$ are the masses of the CRs and DM particles, respectively.

## Mandelstam variable $s$

The Mandelstam variable $s$ is defined as the square of the total four-momentum in the initial state:

$$s = (p_A + p_\chi)^2 = (E_A + m_\chi)^2 - |\vec{p}_A|^2, \tag{A.2}$$

given that for a generic four-momentum $q^\mu$, its square is $q_\mu q^\mu = E^2 - |\vec{q}|^2$.
Considering the CRs four-momentum definition, $|\vec{p}_A|^2 = E_A^2 - m_A^2$, the expression for $s$ becomes:

$$\begin{aligned} s &= (E_A + m_\chi)^2 - (E_A^2 - m_A^2) \\ &= E_A^2 + 2E_A m_\chi + m_\chi^2 - E_A^2 + m_A^2 \end{aligned} \tag{A.3}$$

$$\boxed{s = m_A^2 + m_\chi^2 + 2m_\chi E_A}$$

## Mandelstam variable $t$

The Mandelstam variable $t$ is defined as the square of the four-momentum transfer:

$$t = (p_A - p'_A)^2 = (p'_\chi - p_\chi)^2 \tag{A.4}$$

where $p_\chi = (m_\chi,\, \vec{0})$ is the DM four-momentum before the collision and $p'_\chi = (E_\chi,\, \vec{p}'_\chi)$ is the one after the collision, with $E_\chi$ final DM kinetic energy and $\vec{p}'_\chi$ final DM three-momentum. Now we can derive it as

$$\begin{aligned} t &= (p'_\chi - p_\chi)^2 \\ &= p'_\chi \cdot p'_\chi + p_\chi \cdot p_\chi - 2\, p'_\chi \cdot p_\chi . \end{aligned} \tag{A.5}$$

Since the particles are on-shell, their four-momenta satisfy:

$$\begin{aligned} &p'_\chi \cdot p'_\chi = E'^2_\chi - |\vec{p}'_\chi|^2 = m^2_\chi, \\ &p'_\chi \cdot p_\chi = E'_\chi\, m_\chi . \end{aligned} \tag{A.6}$$

Now, substituting in $t$ we get

$$t = m^2_\chi + m^2_\chi - 2m_\chi E'_\chi = -2m_\chi(E'_\chi - m_\chi); \tag{A.7}$$

in our assumption of $\chi$ initially at rest, the kinetic energy transferred to $\chi$ is given by $K_\chi = E'_\chi - m_\chi$, with $E'_\chi$ being the energy of $\chi$ after the collision. So we obtain the final expression for $t$:

$$\boxed{t = -2m_\chi K_\chi} \tag{A.8}$$

# Appendix B

# Non-Relativistic Limits

In this Appendix, we derive the non-relativistic limits of the products between the spinor wavefunctions, needed to derive the non-relativistic Lagrangian.

## Scalar Mediator case

We have now to consider $\bar{\chi}\chi$; considering the spinor wavefunctions $u$, we can compute the product $\bar{u}u$ in the NR limit for $\vec{p} \to 0$, where $\vec{p}$ is the transferred momentum.

Recalling the Dirac equation

$$(i\partial\!\!\!/ - m)\psi = 0 \tag{B.1}$$

and since spinors satisfy also Klein-Gordon equation $(\Box + m^2)\psi = 0$, they've plane-wave solutions:

$$\psi_s(x) = \int \frac{d^3p}{(2\pi)^3} u_s(p) e^{ipx}\,. \tag{B.2}$$

We obtain the spinor solution using the Dirac equation in the Weyl basis (so a four-component spinor is seen as two two-component spinors):

$$\begin{pmatrix} -m & p\cdot\sigma \\ -p\cdot\sigma & -m \end{pmatrix} u_s(p) = 0\,, \tag{B.3}$$

where $s$ is the spin index.
Considering the 4momentum $p^\mu$, the solutions are

$$u_s(p) = \begin{pmatrix} \sqrt{p^\mu \sigma_\mu}\xi_s \\ \sqrt{p^\mu \bar{\sigma}_\mu}\xi_s \end{pmatrix} = ... = \frac{1}{\sqrt{4m}} \begin{pmatrix} (2m - \vec{p}\cdot\vec{\sigma})\xi_s \\ (2m + \vec{p}\cdot\vec{\sigma})\xi_s \end{pmatrix} + \mathcal{O}(\vec{p}^2)\,, \tag{B.4}$$

where $\xi_s$ are two-components Weyl spinors and we have defined $\sigma^\mu = (\mathbb{1}, \vec{\sigma})$ and $\bar{\sigma}^\mu = (\mathbb{1}, -\vec{\sigma})$. Then, considering the NR approximation of the 4-momentum, $p^\mu = (\sqrt{m^2 + \vec{p}^2}, \vec{p}) \approx (m, \vec{p}) + \mathcal{O}(\vec{p}^2)$, we can compute at the first-order approximation of $\bar{u}u$:

$$
\begin{aligned}
\bar{u}_s(p)u_{s'}(p) &= \begin{pmatrix} \sqrt{p^\mu\sigma_\mu}\xi_s \\ \sqrt{p^\mu\bar{\sigma}_\mu}\xi_s \end{pmatrix}^\dagger \begin{pmatrix} 0 & \mathbb{1} \\ \mathbb{1} & 0 \end{pmatrix} \begin{pmatrix} \sqrt{p^\mu\sigma_\mu}\xi^s \\ \sqrt{p^\mu\bar{\sigma}_\mu}\xi^s \end{pmatrix} \\
&= \begin{pmatrix} \sqrt{p^\mu\bar{\sigma}_\mu}\xi^{r\dagger} & \sqrt{p^\mu\sigma_\mu}\xi^{r\dagger} \end{pmatrix} \begin{pmatrix} \sqrt{p^\mu\sigma_\mu}\xi^s \\ \sqrt{p^\mu\bar{\sigma}_\mu}\xi^s \end{pmatrix} \\
&= \big(p^\mu\bar{\sigma}_\mu + p^\mu\sigma_\mu\big)\xi^{r\dagger}\xi^s \\
&= \big(m - \vec{p}\cdot\vec{\sigma} + m + \vec{p}\cdot\vec{\sigma}\big)\delta_{rs} \\
&= 2m\delta_{rs}
\end{aligned} \tag{B.5}
$$

Using this result and considering $|\chi\rangle$ as a Dirac spinor, we can obtain the scalar operator $\bar{\chi}\chi$ as

$$
\boxed{\bar{\chi}\chi = 2m_\chi} \tag{B.6}
$$

# Pseudoscalar Mediator case

Considering the Dirac fermions as before, we can compute the previous product considering a gamma 5

$$
\begin{aligned}
\bar{u}_r\gamma_5 u_s &= u^{r\dagger}\gamma^0\gamma_5 u^s \\
&= \begin{pmatrix} \sqrt{p^\mu\sigma_\mu}\xi^{r\dagger} & \sqrt{p^\mu\bar{\sigma}_\mu}\xi^{r\dagger} \end{pmatrix} \begin{pmatrix} 0 & \mathbb{1} \\ \mathbb{1} & 0 \end{pmatrix} \begin{pmatrix} -\mathbb{1} & 0 \\ 0 & \mathbb{1} \end{pmatrix} \begin{pmatrix} \sqrt{p^\mu\sigma_\mu}\xi^r \\ \sqrt{p^\mu\bar{\sigma}_\mu}\xi^s \end{pmatrix} \\
&= \begin{pmatrix} \sqrt{p^\mu\bar{\sigma}_\mu}\xi^{r\dagger} & \sqrt{p^\mu\sigma_\mu}\xi^{r\dagger} \end{pmatrix} \begin{pmatrix} -\mathbb{1} & 0 \\ 0 & \mathbb{1} \end{pmatrix} \begin{pmatrix} \sqrt{p^\mu\sigma_\mu}\xi^r \\ \sqrt{p^\mu\bar{\sigma}_\mu}\xi^s \end{pmatrix} \\
&= \begin{pmatrix} -\sqrt{p^\mu\bar{\sigma}_\mu}\xi^{r\dagger} & \sqrt{p^\mu\sigma_\mu}\xi^{r\dagger} \end{pmatrix} \begin{pmatrix} \sqrt{p^\mu\sigma_\mu}\xi^r \\ \sqrt{p^\mu\bar{\sigma}_\mu}\xi^s \end{pmatrix} \\
&= \Bigg( - \sqrt{p^\mu\bar{\sigma}_\mu}\sqrt{p^\mu\sigma_\mu} + \sqrt{p^\mu\sigma_\mu}\sqrt{p^\mu\bar{\sigma}_\mu}\Bigg)\xi^{r\dagger}\xi^s = 0
\end{aligned} \tag{B.7}
$$

This is zero at the lowest order, but if now we expand at the first order considering the NR limit we have

$$
u_s(\vec{p}) \sim \begin{pmatrix} \xi^s \\ \frac{\vec{\sigma}\cdot\vec{p}}{2m}\xi^s \end{pmatrix}; \qquad \bar{u}_s(\vec{p}) = \begin{pmatrix} \xi^{s\dagger} & \frac{\vec{\sigma}\cdot\vec{p}}{2m}\xi^{s\dagger} \end{pmatrix} \tag{B.8}
$$

where $\xi$ is a two-components Weyl spinor representing the NR spin state. Finally we get

$$
\begin{aligned}
\bar{u}_r(\vec{p_1})\gamma_5 u_s(\vec{p_2}) &= \begin{pmatrix} \xi^{r\dagger} & \frac{\sigma\cdot\vec{p}_1}{2m}\xi^{r\dagger} \end{pmatrix} \begin{pmatrix} -\mathbb{1} & 0 \\ 0 & \mathbb{1} \end{pmatrix} \begin{pmatrix} \xi^s \\ \frac{\vec{\sigma}\cdot\vec{p}}{2m}\xi^s \end{pmatrix} \\
&= \begin{pmatrix} -\xi^{r\dagger} & \frac{\sigma\cdot\vec{p}_1}{2m}\xi^{r\dagger} \end{pmatrix} \begin{pmatrix} \xi^s \\ \frac{\vec{\sigma}\cdot\vec{p}}{2m}\xi^s \end{pmatrix} \\
&= \delta^{rs}\Bigg( - \frac{\vec{\sigma}\cdot\vec{p}_1}{2m} + \frac{\vec{\sigma}\cdot\vec{p}_2}{2m}\Bigg) = \frac{\vec{\sigma}\cdot\vec{p}}{2m}
\end{aligned} \tag{B.9}
$$

Using this result, we can obtain the pseudoscalar operators $\langle N| \frac{\vec{\sigma}\cdot\vec{p}}{2m} |N\rangle$ and $\langle\chi| \frac{\vec{\sigma}\cdot\vec{p}}{2m_\chi} |\chi\rangle$ as

$$\boxed{\bar{u}_r(\vec{p_1})\gamma_5 u_s(\vec{p_2}) = \frac{\vec{\sigma}\cdot\vec{p}}{2m}}$$

where we have defined the transferred momentum $\vec{p} = \vec{p}_2 - \vec{p}_1$.

# Appendix C

# Determination of the Differential cross-section

In this paragraph, we derive the differential cross-section for DM-SM interactions. To remain general and obtain a formula valid for both DM-CRs upscattering and DM scattering in the detector, we consider as the initial state a particle 1 at rest, with mass $m_1$, and a particle 2 in motion, with mass $m_2$. This situation is schematized in Figure C.1. The 4-momenta of these particles are, respectively:

$$\begin{aligned} p_1 &= (m_1, \vec{0})\,, \\ p_2 &= (E_2, \vec{p}_2), \quad m_2^2 = E_2^2 - |\vec{p}_2|^2\,. \end{aligned} \tag{C.1}$$

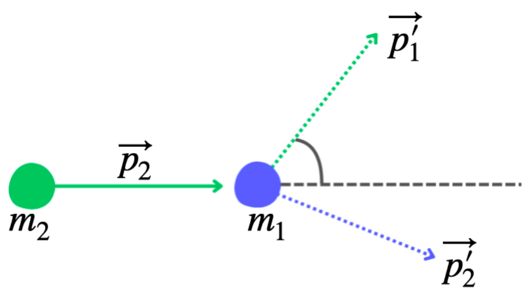


**Figure C.1.** Diagram of a two-to-two scattering process involving a particle initially at rest and an incoming particle.

The derivations obtained below apply both to DM-CRs interactions, where the initial state consists of a DM particle at rest ($m_1 = m_\chi$) and a cosmic ray in motion ($m_2 = m_A$), and to DM-N interactions, where $N$ is a proton in the detector. In the latter case, the proton is at rest ($m_1 = m_p$) and the DM particle is in motion ($m_2 = m_\chi$). Then, to derive the differential cross-section of DM with the nucleus A, we treat the nucleus A as made by point-like nucleons and we introduce the form factors to consider the finite size effect of the nucleus.

From Quantum Field Theory [2] we know that, for a two-to-two scattering, the general expression for the cross-section[1] is

$$\left(\frac{d\sigma}{d\Omega}\right)_{\text{CM}} = \frac{1}{64\pi^2 E_{\text{CM}}^2} \frac{|\vec{p_f}|}{|\vec{p_i}|} |\mathcal{M}|^2 \Theta(E_{\text{CM}} - m_1 - m_2)\,, \tag{C.2}$$

where $E_{\text{CM}}^2 = s$ is the square of the center-of-mass energy; additionally, since for an elastic scattering momentum and kinetic energy are conserved, we have that $|\vec{p_f}| = |\vec{p_i}|$.
To derive the differential cross-section respect to the final kinetic energy $K_f$, we can consider that, in the center of mass frame,

$$K_f = K_{\text{max}} \frac{1+\cos\theta}{2}\,, \qquad \text{with} \qquad K_{\text{max}} = \frac{4m_1 m_2}{(m_1+m_2)^2} \cdot K_2 \tag{C.3}$$

where $\theta$ is the scattering angle [99]. Considering that the differential of the solid angle is defined as $d\Omega = d\psi d\cos\theta = 2\pi d\cos\theta$, we can derive that

$$\frac{dK_f}{d\Omega} = \frac{K_{\text{max}}}{4\pi}\,. \tag{C.4}$$

To conclude, we can derive the differential cross-section respect to the final kinetic energy, since plugging Eq. C.4 into Eq. C.2 we derive

$$\boxed{\frac{d\sigma}{dK_f} = \frac{1}{K_{\text{max}}} \frac{1}{16\pi s} |\mathcal{M}|^2 \Theta(K_{\text{max}} - K_f)} \tag{C.5}$$

From this equation, we can now obtain the final form of this differential cross-section, deriving the square of the matrix element both in the scalar and pseudoscalar mediator cases.

## Scalar Mediator case

The Feynman diagram of the $\chi N \to \chi N$ scattering, mediated by a scalar particle, is represented in Figure C.2.

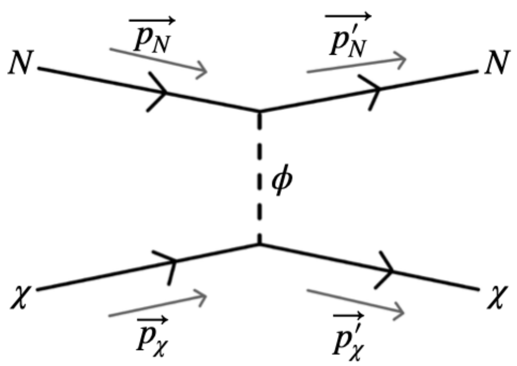


**Figure C.2.** Feynman diagram of the $\chi N \to \chi N$ scattering, mediated by a scalar particle.

[1]This formula corresponds to Equation (5.32) in Ref. [2].

The scattering amplitude for this process is given by:

$$\begin{aligned}\mathcal{M} &= \bar{u}(p'_\chi)(-ig_{\chi\phi})u(p_\chi)\frac{i}{t-m_\phi^2}\bar{u}(p'_N)(-ig_{N\phi})u(p_N) \\ &= \frac{-ig_{\chi\phi}g_{N\phi}}{t-m_\phi^2}\left[\bar{u}(p'_\chi)u(p_\chi)\right]\left[\bar{u}(p'_N)u(p_N)\right]\end{aligned} \tag{C.6}$$

where

- $\bar{u}(p'_\chi)$ and $\bar{u}(p'_N)$ are the Dirac spinors for the outgoing fermion and nucleon, respectively;
- $u(p_\chi)$ and $u(p_N)$ are the Dirac spinors for the incoming fermion and nucleon, respectively;
- $t$ is the Mandelstam variable $t = (p_\chi - p'_\chi)^2$;
- $m_\phi$ is the mass of the scalar mediator.

Now we have to consider the square of this matrix element, averaging over initial spins and summing over final spins (in order to take into account the initial and final spin states):

$$|\mathcal{M}|^2 = \frac{1}{4}\sum_{\text{spins}}\left\{\frac{g_{\chi\phi}^2 g_{N\phi}^2}{(t-m_\phi^2)^2}\left|\bar{u}(p'_\chi)u(p_\chi)\right|^2\left|\bar{u}(p'_N)u(p_N)\right|^2\right\} \tag{C.7}$$

The squared spinor contractions can be expressed for each fermion and nucleon, using the properties of Dirac spinors [129], as

$$\begin{aligned}\sum_{\text{spins}}|\bar{u}(p')u(p)|^2 &= \mathrm{Tr}\left[(\not{p}+m)(\not{p}'+m)\right] \\ &= 4(p\cdot p' + m^2)\end{aligned} \tag{C.8}$$

with $\not{p} = \gamma^\mu p_\mu$, where $\gamma^\mu$ is the *gamma matrix* of the Dirac theory. For an elastic scattering the $t$ variable is expressed as

$$t = (p-p')^2 = 2m^2 - 2p\cdot p' \rightarrow p\cdot p' = m^2 - \frac{t}{2} \tag{C.9}$$

Substituting all in the matrix element expression we get

$$\begin{aligned}|\mathcal{M}|^2 &= \frac{1}{4}\frac{g_{\chi\phi}^2 g_{N\phi}^2}{(t-m_\phi^2)^2}[4(m_\chi^2 - \frac{t}{2} + m_\chi^2)][4(m_N^2 - \frac{t}{2} + m_N^2)] \\ &= 4\frac{g_{\chi\phi}^2 g_{N\phi}^2}{(t-m_\phi^2)^2}(2m_\chi^2 - \frac{t}{2})(2m_N^2 - \frac{t}{2}) \\ &= \frac{g_{\chi\phi}^2 g_{N\phi}^2}{(t-m_\phi^2)^2}(4m_\chi^2 - t)(4m_N^2 - t)\end{aligned} \tag{C.10}$$

Now we can substitute the square of the matrix element in the expression of the differential cross-section of Equation (C.5):

$$\frac{d\sigma_\phi}{dK_f} = \frac{1}{K_{\text{max}}}\frac{1}{16\pi s}\frac{g_{\chi\phi}^2 g_{N\phi}^2}{(t-m_\phi^2)^2}(4m_\chi^2 - t)(4m_N^2 - t)\Theta(K_{\text{max}} - K_f) \tag{C.11}$$

Finally, to consider the finite size of the nucleons, we have to consider a multiplicative term of $n_A^2 F_A^2(-t)$, where $n_A$ is the number of nucleons inside the considered nuclei and $F_A(-t)$ is the form factor.

The final form for the differential cross-section in terms of the kinetic energy is

$$\boxed{\frac{d\sigma_\phi}{dK_f} = \frac{1}{K_{\text{max}}}\frac{g_{\chi\phi}^2 g_{N\phi}^2}{16\pi s}\frac{(4m_\chi^2 - t)(4m_A^2 - t)}{(t-m_\phi^2)^2} n_A^2 F_A^2(-t)\Theta(K_{\text{max}} - K_f)} \tag{C.12}$$

## Pseudoscalar Mediator case

The scattering amplitude for the process $\chi N \to \chi N$, mediated by a pseudoscalar particle, is:

$$\mathcal{M} = -\frac{g_{\chi a} g_{Na}}{t - m_a^2}[\bar{u}(p'_\chi)\gamma^5 u(p_\chi)][\bar{u}(p'_N)\gamma^5 u(p_N)]. \tag{C.13}$$

Similarly as the scalar case, the square of the matrix element averaging over initial spins and summing over final spins is

$$|\mathcal{M}|^2 = \frac{1}{4}\sum_{\text{spins}}\left\{\frac{g_{\chi a}^2 g_{Na}^2}{(t-m_a^2)^2}\left|\bar{u}(p'_\chi)\gamma^5 u(p_\chi)\right|^2\left|\bar{u}(p'_N)\gamma^5 u(p_N)\right|^2\right\}. \tag{C.14}$$

Due to the presence of the $\gamma^5$ matrix, the spin contraction becomes [129]:

$$\sum_{\text{spins}} |\bar{u}(p')\,\gamma^5\,u(p)|^2 = 2t\,. \tag{C.15}$$

Therefore, the final form for the differential cross-section in terms of the kinetic energy is

$$\boxed{\frac{d\sigma_a}{dK_f} = \frac{1}{K_{max}}\frac{g_{\chi a}^2 g_{Na}^2}{16\pi s}\frac{t^2}{(m_a^2 - t)^2} F_a^2(-t)\Theta(K_{\text{max}} - K_f)} \tag{C.16}$$

# Appendix D

# Dependence of the Effective Path on the Zenith Angle

In this Appendix, we describe how we can derive the traveled distance of an incoming particle inside a Earth or Antarctic Ice, before to reaching the detector.

We consider an incoming DM particle, with zenith angle $\theta$ and a detector at the depth $d$ respect to Earth's surface; this situation is represented in Figure D.1.

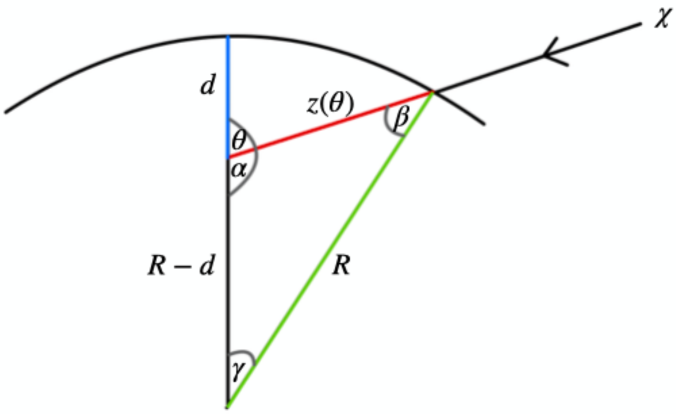


**Figure D.1.** Graphical representation of the geometry of the distance traveled by the DM inside the Earth before reaching the detector; the Earth's radius is indicated as $R$.

To study the Earth and Ice attenuation of the flux, we have to derive the dependence of the traveled distance $z$ on the angle $\theta$.
Considering the triangle with sides $R$, $R-d$, and $z$, it immediately follows that $\alpha + \beta + \gamma = 180°$ and $\alpha = 180° - \theta$; then, recalling the *Law of Sines*

$$\frac{z}{\sin\gamma} = \frac{R-d}{\sin\beta} = \frac{R}{\sin\alpha}, \tag{D.1}$$

we can easily get a 2-equations system

$$\begin{cases} \frac{R-d}{\sin\beta} = \frac{R}{\sin\alpha} \\ \frac{z}{\sin\gamma} = \frac{R}{\sin\alpha}. \end{cases} \tag{D.2}$$

Using that $\sin\alpha = \sin(180° - \theta) = \sin\theta$ and that $\sin\gamma = \sin(180° - \alpha - \beta) = \sin(\theta - \beta)$, the previous system becomes

$$\begin{cases} \sin\beta = \frac{R-d}{R}\sin\theta \\ z = R\frac{\sin(\theta-\beta)}{\sin\theta}. \end{cases} \tag{D.3}$$

Finally, considering that $\sin(\theta - \beta) = \sin\theta\cos\beta - \sin\beta\cos\theta$, $\cos\beta = \sqrt{1 - \sin^2\beta}$, and substituting $\sin\beta$ into the second equation, we get the final form for $z(\theta)$:

$$\begin{aligned} z &= R\left[\sqrt{1-\sin^2\beta} - \frac{\cos\theta}{\sin\theta}\sin\beta\right] \\ &= R\left[\sqrt{1 - \frac{(R-d)^2}{R^2}\sin^2\theta} - \frac{R-d}{R}\cos\theta\right] \end{aligned} \tag{D.4}$$

$$\hookrightarrow \boxed{z(\theta) = \sqrt{R^2 - (R-d)^2\sin^2\theta} - (R-d)\cos\theta}$$

This expression is in agreement with the expected limits $z(\theta \to 0°) = d$, and $z(\theta \to 180°) = 2R - d$.

# Appendix E

# J-factor in Galactic and Equatorial Coordinates

In this Appendix, we briefly describe the coordinate systems used to determine the position of celestial bodies relative to a given reference frame. Specifically, we discuss the galactic coordinate system, centered in the center of the Sun, and the equatorial coordinate system, centered in the center of the Earth.

## Galactic Coordinate system

The Galactic Coordinate system is a spherical coordinate system where each object is identified by a galactic latitude $b$, and a galactic longitude $l$. The galactic latitude measures the angular distance of an object to the galactic plane, while the galactic longitude is measured concerning the primary direction from the Sun to the center of the galaxy in the galactic plane.

In this coordinate frame, the Sun and the Galactic center share the same direction $(l_0, b_0) = (0°, 0°)$; however, the distance between the two is different, since the Sun is approximately $8.5$ kpc away from the Galactic center.

Given that the DN profile follows the Navarro-Frenk-White profile, which is centered at the galactic center, it follows that, in the $(l, b)$ coordinate plane, the J-factor exhibits a higher value in the central regions of the reference frame, as shown in Figure E.1.

## Equatorial Coordinate System

To define the position of celestial objects with respect to the center of the Earth, the Equatorial Coordinate system is used; this frame is usually implemented in spherical coordinates, where the two angular variables are the declination and the right ascension. The declination $\delta$ measures the angular distance of an astronomical object from the celestial equator, while the right ascension $\alpha$ measures the angular distance of an object along the celestial equator. As for the terrestrial longitude, $\alpha$ is usually measured in sidereal hours, minutes, and seconds, even if in the following we use degrees.

In this frame, the J-factor exhibits a higher value in correspondence with the origin of the Galactic Coordinate system, which corresponds to $(\alpha_0, \delta_0) = (266.4°, -28.9°)$, as shown in the Figure E.2.

## Transformations between the two coordinate frames

In the following, we present the transformations between the Galactic and Equatorial systems.
To perform these transformations, as reported in [130], the coordinates of the North Galactic pole are useful; the $J2000.0$[1] equatorial coordinates of the north Galactic pole are

$$\alpha_{\text{NGP}} = 192.86°, \qquad \delta_{\text{NGP}} = 27.13°, \tag{E.1}$$

while the $J2000.0$ galactic coordinates of the north celestial pole are

$$l_{\text{NCP}} = 123.93°, \qquad b_{\text{NCP}} = 27.13°. \tag{E.2}$$

These transformations involve methods of spherical trigonometry, here we report only the transformation's laws.
From equatorial $(\alpha, \delta)$ to galactic coordinates $(b, l)$, the transformation's law is:

$$\begin{cases} \sin b = \sin \delta_{\text{NGP}} \sin \delta + \cos \delta_{\text{NGP}} \cos \delta \cos(\alpha - \alpha_{\text{NGP}}) \\ \cos b \sin(l_{\text{NCP}} - l) = \cos \delta \sin(\alpha - \alpha_{\text{NGP}}) \\ \cos b \cos(l_{\text{NCP}} - l) = \cos \delta_{\text{NGP}} \sin \delta - \sin \delta_{\text{NGP}} \cos \delta \cos(\alpha - \alpha_{\text{NGP}}) \end{cases} \tag{E.3}$$

Finally, from galactic $(b, l)$ to equatorial coordinates $(\alpha, \delta)$, the transformation law is:

$$\begin{cases} \sin \delta = \sin \delta_{\text{NGP}} \sin b + \cos \delta_{\text{NGP}} \cos b \cos(l_{\text{NCP}} - l) \\ \cos \delta \sin(\alpha - \alpha_{\text{NGP}}) = \cos b \sin(l_{\text{NCP}} - l) \\ \cos \delta \cos(\alpha - \alpha_{\text{NGP}}) = \cos \delta_{\text{NGP}} \sin b - \sin \delta_{\text{NGP}} \cos b \cos(l_{\text{NCP}} - l) \end{cases} \tag{E.4}$$

[1] This is the standard astronomical reference time, which is the Julian Date corresponding to January 1, 2000, at 12:00 TT (Terrestrial Time).

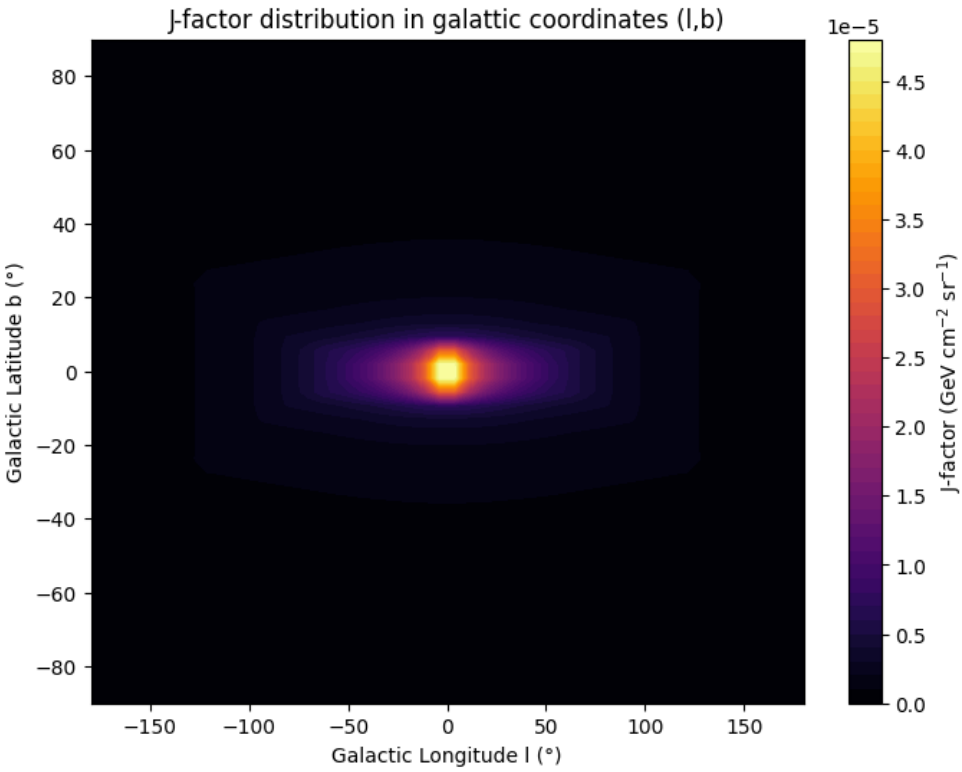


**Figure E.1.** J-factor distribution in the galactic coordinates.

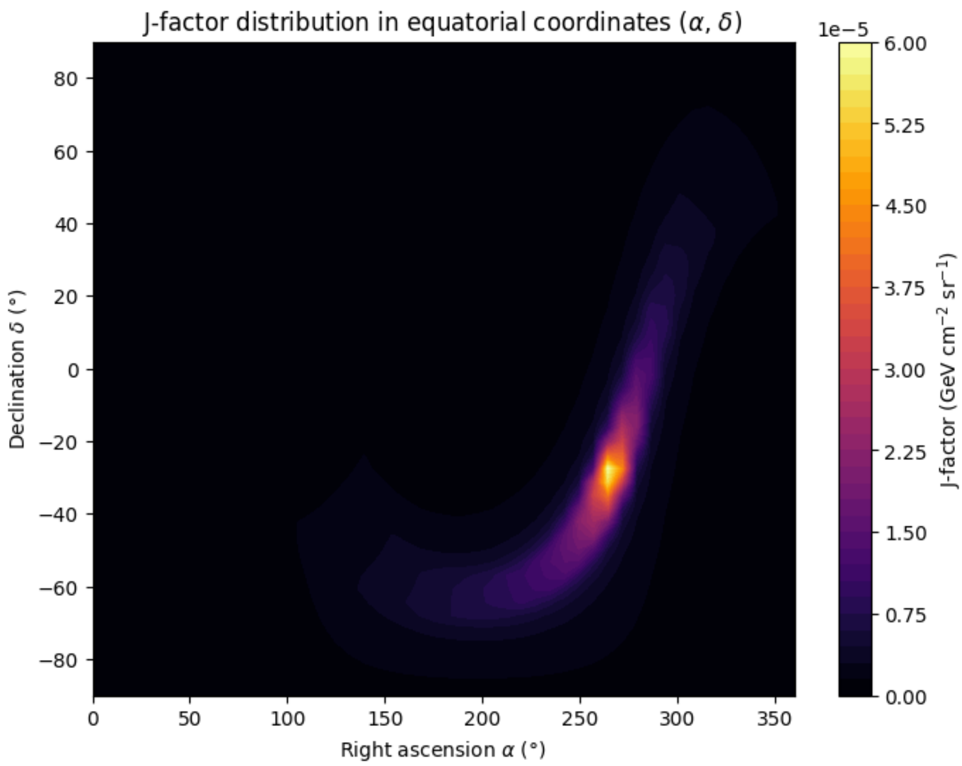


**Figure E.2.** J-factor distribution in the equatorial coordinates.

# Bibliography


[1] The Plank Collaboration. "Planck 2015 results. XIII. Cosmological parameters". In: *AA 594, A13* (2016). arXiv: 1502.01589v3.

[2] Matthew D. Schwartz. *Quantum Field Theory and the Standard Model*. Harvard University, Massachusetts, 2013. ISBN: 9781107034730.

[3] Cliff Burgess and Guy Moore. *The Standard Model, A Primer*. Cambridge University Press, 2006.

[4] Yohei Ema, Filippo Sala, and Ryosuke Sato. "Light Dark Matter at Neutrino Experiments". In: *Phys. Rev. Lett. 122, 181802* (2019). arXiv: 1811.00520v3.

[5] Torsten Bringmann and Maxim Pospelov. "Novel Direct Detection Constraints on Light Dark Matter". In: *Phys. Rev. Lett. 122, 171801* (2019). arXiv: 1810.10543v2.

[6] Yohei Ema, Filippo Sala, and Ryosuke Sato. "Neutrino experiments probe hadrophilic light dark matter". In: *SciPost Phys. 10, 072* (2021). arXiv: 2011.01939v2.

[7] Gianfranco Bertone and Dan Hooper. "A History of Dark Matter". In: *Rev. Mod. Phys. 90, 45002* (2016). arXiv: 1605.04909v2.

[8] Marco Cirelli, Alessandro Strumia, and Jure Zupan. "Dark Matter". In: (2024). arXiv: 2406.01705v2.

[9] Vera Rubin Yoshiaki Sofue. "Rotation Curves of Spiral Galaxies". In: *Ann.Rev. Astron.Astrophys. 39 (2001) 137-174* (2000). arXiv: astro-ph/0010594v3.

[10] Vera Rubin and W. Kent Ford. "Rotation of the Andromeda Nebula from a Spectroscopic Survey of Emission Regions". In: (1970).

[11] M. S. Roberts and A. H Rots. "Comparison of Rotation Curves of Different Galaxy Types". In: *Astronomy and Astrophysics, Vol. 26, p. 483-485* (1973).

[12] Risa H. Wechsler and Jeremy L. Tinker. "The Connection Between Galaxies and Their Dark Matter Halos". In: (2018). arXiv: 1804.03097v1.

[13] A. Burkert. "The Structure of Dark Matter Halos in Dwarf Galaxies". In: (1995). arXiv: astro-ph/9504041v1.

[14] Kateryna Kvasova, Evan N. Kirby, and Rachael L. Beaton. "Kinematics and metallicity of the dwarf spheroidal galaxy Andromeda XVIII". In: (2024). arXiv: 2404.11804v4.

[15] Kohei Hayashi, Elisa G. M. Ferreira, and Hei Yin Jowett Chan. "Narrowing the Mass Range of Fuzzy Dark Matter with Ultra-faint Dwarfs". In: (2021). arXiv: 2102.05300v2.

[16] Marceau Limousin, Benjamin Beauchesne, and Eric Jullo. “Dark Matter in Galaxy Clusters: a Parametric Strong Lensing Approach”. In: (2022). arXiv: 2202.02992v2.

[17] Heinz Andernach (translator) and Fritz Zwicky (author). “English and Spanish Translation of Zwicky’s (1933) The Redshift of Extragalactic Nebulae”. In: (1933). arXiv: 1711.01693v1.

[18] Debasish Majumdar. *Dark Matter: an Introduction*. CRC Press, 2014.

[19] Sinclair Smith. “The Mass of the Virgo Cluster”. In: *Astrophysical Journal, vol. 83, p.23* (1936).

[20] Matthias Bartelmann. “Gravitational Lensing”. In: (2010). arXiv: 1010.3829v1.

[21] Andrew Robertson, Richard Massey, and Vincent Eke. “What does the Bullet Cluster tell us about self-interacting dark matter?” In: (2017). arXiv: 1605.04307v2.

[22] Douglas Clowe, Marusa Bradac, and Anthony H. Gonzalez et al. “A direct empirical proof of the existence of dark matter”. In: *ApJ 648 L109* (2006). arXiv: astro-ph/0608407v1.

[23] David Harvey, Richard Massey, and Thomas Kitching et al. “The non-gravitational interactions of dark matter in colliding galaxy clusters”. In: *Science, Vol. 347 no. 6229 pp. 1462-1465* (2015). arXiv: 1503.07675v2.

[24] Pratika Dayal and Andrea Ferrara. “Early galaxy formation and its large-scale effects”. In: *Proc. IAU 15 (2019) 43-43* (2018). arXiv: 1809.09136v2.

[25] Mark Vogelsberger, Shy Genel, and Volker Springel et al. “Introducing the Illustris Project: simulating the coevolution of dark and visible matter in the Universe”. In: (2014). arXiv: 1405.2921v2.

[26] Subhajit Ghosh, Daven Wei Ren Ho, and Yuhsin Tsai. “Dark Matter-Radiation Scattering Enhances CMB Phase Shift through Dark Matter-loading”. In: *JCAP01 (2025) 058* (2025). arXiv: 2405.08064v2.

[27] The Plank Collaboration. “Planck 2018 results. VI. Cosmological parameters”. In: *AA 641, A6* (2018). arXiv: 1807.06209v4.

[28] Michael Kopp Stéphane Ilić, Constantinos Skordis, and Daniel B. Thomas. “Dark Matter properties through cosmic history”. In: *Phys. Rev. D 104, 043520* (2021). arXiv: 2004.09572v2.

[29] Lars Bergström. “Dark Matter Evidence, Particle Physics Candidates and Detection Methods”. In: (2012). arXiv: 1205.4882v3.

[30] Gianfranco Bertone, Dan Hooper, and Joseph Silk. “Particle Dark Matter: Evidence, Candidates and Constraints”. In: (2004). arXiv: hep-ph/0404175v2.

[31] David Merritt, Alister W. Graham, and Ben Moore et al. “Empirical Models for Dark Matter Halos. I. Nonparametric Construction of Density Profiles and Comparison with Parametric Models”. In: *Astron.J., v.132, p.2685-2700* (2006). arXiv: astro-ph/0509417v2.

[32] V. Avila-Reese et al. “Density profiles of dark matter haloes: diversity and dependence on environment”. In: *Mon.Not.Roy. Astron.Soc. 309 (1999) 507* (1999). arXiv: astro-ph/9906260v2.

[33] Julio F. Navarro, Carlos S. Frenk, and Simon D.M. White. "The Structure of Cold Dark Matter Halos". In: *Astrophys.J.462:563-575,1996* (1995). arXiv: astro-ph/9508025v1.

[34] Patrick G. Staudt and James S. Bullock et al. "Sliding into DM: Determining the local dark matter density and speed distribution using only the local circular speed of the Galaxy". In: *JCAP 08 (2024) 022* (2024). arXiv: 2403.04122v3.

[35] Jaan Einasto. "On the Construction of a Composite Model for the Galaxy and on the Determination of the System of Galactic Parameters". In: (1965).

[36] K. G. Begeman, A. H. Broeils, and R. H. Sanders. "Extended rotation curves of spiral galaxies: dark haloes and modified dynamics". In: (1991). DOI: https://doi.org/10.1093/mnras/249.3.523.

[37] Carlos Pérez de los Heros. "Status, Challenges and Directions in Indirect Dark Matter Searches". In: *Symmetry 2020, 12(10), 1648* (2020). arXiv: 2008.11561v2.

[38] Tim Zimmermann, James Alvey, and David J. E. Marsh et al. "Dwarf galaxies imply dark matter is heavier than 2.2×1021eV". In: *Phys. Rev. Lett. 134, 151001* (2025). arXiv: 2405.20374v3.

[39] Anne M. Green. "Primordial black holes as a dark matter candidate - a brief overview". In: (2024).

[40] Bernard Carr, Florian Kuhnel, and Marit Sandstad. "Primordial Black Holes as Dark Matter". In: *Phys. Rev. D 94, 083504 (2016)* (2017). arXiv: 1607.06077v4.

[41] Daniel J. H. Chung, Edward W. Kolb, and Antonio Riotto. "Superheavy dark matter". In: *Phys. Rev. D 59, 023501* (1998). arXiv: hep-ph/9802238v2.

[42] Edward W. Kolb, Daniel J. H. Chung, and Antonio Riotto. "WIMPZILLAS!" In: (1998). arXiv: hep-ph/9810361v1.

[43] Jonathan L. Feng. "The WIMP Paradigm: Theme and Variations". In: *SciPost Phys. Lect. Notes 71* (2023). arXiv: 2212.02479v2.

[44] Jodi Cooley. "Dark Matter Direct Detection of Classical WIMPs". In: *SciPost Phys. Lect. Notes 55* (2022). arXiv: 2110.02359v2.

[45] Scott Dodelson and Lawrence M. Widrow. "Sterile Neutrinos as Dark Matter". In: *Phys.Rev.Lett.72:17-20,1994* (1993). arXiv: hep-ph/9303287v1.

[46] A. Boyarsky, M. Drewes, and T. Lasserre et al. "Sterile Neutrino Dark Matter". In: (2018). DOI: https://doi.org/10.1016/j.ppnp.2018.07.004.

[47] Simon Knapen Tongyan Lin and Kathryn M. Zurek. "Light dark matter: Models and constraints". In: (2017). arXiv: 1709.07882v2.

[48] Sowmiya Balan, Csaba Balázs, and Torsten Bringmann et al. "Resonant or asymmetric: The status of sub-GeV dark matter". In: *JCAP01(2025)053* (2024). arXiv: 2405.17548v2.

[49] Roberto. D. Peccei and Helen R. Quinn. "CP Conservation in the Presence of Pseudoparticles". In: (1977). DOI: https://doi.org/10.1103/PhysRevLett.38.1440.

[50] Aleksandr Chatrchyan et al. "ALP dark matter with non-periodic potentials: parametric resonance, halo formation and gravitational signatures". In: *JCAP10(2023)068* (2023). arXiv: 2305.03756v2.

[51] Hooman Davoudiasl and Christopher W. Murphy. "Fuzzy Dark Matter from Infrared Confining Dynamics". In: *Phys. Rev. Lett. 118, 141801* (2017). arXiv: 1701.01136v2.

[52] Jens C. Niemeyer. "Small-scale structure of fuzzy and axion-like dark matter". In: (2020). arXiv: 1912.07064v1.

[53] Vid Iršič, Matteo Viel, and Martin G. Haehnelt et al. "First Constraints on Fuzzy Dark Matter from Lyman-$\alpha$ Forest Data and Hydrodynamical Simulations". In: *Phys. Rev. Lett. 119, 031302* (2017). arXiv: 1703.04683v2.

[54] D. Savchenko and A. Rudakovskyi. "New mass bound on fermionic dark matter from a combined analysis of classical dSphs". In: (2019). arXiv: 1903.01862v2.

[55] Ronny Frumkin, Eric Kuflik, and Itay Lavie et Tal Silverwater. "Roadmap to Thermal Dark Matter Beyond the WIMP Unitarity Bound". In: *Phys. Rev. Lett. 130 171001* (2024). arXiv: 2207.01635v3.

[56] A. Arbey and F. Mahmoudi. "Dark matter and the early Universe: a review". In: (2021). DOI: https://doi.org/10.1016/j.ppnp.2021.103865.

[57] Graciela B. Gelmini. "Light weakly interacting massive particles". In: (2017). arXiv: 1612.09137v2.

[58] Xiaoyong Chu, Thomas Hambye, and Michel H.G. Tytgat. "The Four Basic Ways of Creating Dark Matter Through a Portal". In: (2012). arXiv: 1112.0493v2.

[59] Wan-Zhe Feng, Zi-Hui Zhang, and Kai-Yu Zhang. "Sub-GeV millicharge dark matter from the U(1)X hidden sector". In: *JCAP 05 (2024) 112* (2024). arXiv: 2312.03837v3.

[60] Kathryn M. Zurek. "Asymmetric Dark Matter: Theories, Signatures, and Constraints". In: (2013). arXiv: 1308.0338v2.

[61] Martin Bauer and Tilman Plehn. *Yet Another Introduction to Dark Matter*. Springer Nature, 2019. arXiv: 1705.01987v2.

[62] Daniel Abercrombie et al. "Dark Matter Benchmark Models for Early LHC Run-2 Searches: Report of the ATLAS/CMS Dark Matter Forum". In: *Phys. Dark Univ. 26 (2019) 100371* (2015). arXiv: 1507.00966v1.

[63] Oliver Buchmueller, Caterina Doglioni, and Lian-Tao Wang. "Search for dark matter at colliders". In: *Nature Phys 13, 2017-223* (2019). arXiv: 1912.12739v1.

[64] European Strategy for Particle Physics Preparatory Group. *Physics Briefing Book*. 2020.

[65] Rouven Essig, Jeremy Mardon, and Tomer Volansky. "Direct Detection of Sub-GeV Dark Matter". In: *Phys.Rev. D85 (2012) 076007* (2012). arXiv: 1108.5383v3.

[66] Mariano Cababie. "The SENSEI Experiment: An Ultrasensitive Search for Sub-GeV Dark Matter". In: (2022).

[67] Radomir Smida. “The search for light dark matter with DAMIC-M”. In: (2024). arXiv: 2409.20290v1.

[68] The CRESST Collaboration. “First results from the CRESST-III low-mass dark matter program”. In: *Phys. Rev. D 100, 102002* (2019). arXiv: 1904.00498v1.

[69] NEWS-G collaboration. “The NEWS-G detector at SNOLAB”. In: (2023). arXiv: 2205.15433v3.

[70] Jason Kumar. “Indirect detection of sub-GeV dark matter coupling to quarks”. In: *Phys. Rev. D 98, 116009* (2018). arXiv: 1808.02579v2.

[71] Tracy R. Slatyer. “TASI Lectures on Indirect Detection of Dark Matter”. In: (2017). arXiv: 1710.05137v1.

[72] Antonio Boveia and Caterina Doglioni. “Dark Matter Searches at Colliders”. In: (2018). arXiv: 1810.12238v1.

[73] ATLAS Collaboration. “Prospects for a search of invisible particles produced in association with single-top quarks with the ATLAS detector at the HL-LHC”. In: (2018).

[74] Alexander Friedland et al. “Probing Nonstandard Standard Model Backgrounds with LHC Monojets”. In: *Physics Letters B 714 (2012), pp. 267-275* (2012). arXiv: 1111.5331v3.

[75] Alexandre Brea Rodríguez, Veronika Chobanova, and Xabier Cid Vidal et al. “Prospects on searches for baryonic Dark Matter produced in b-hadron decays at LHCb”. In: *Eur. Phys. J. C (2021) 81:964* (2021). arXiv: 2106.12870v2.

[76] The Belle II Collaboration. “The Belle II Physics Book”. In: *Prog Theor Exp Phys* (2019). arXiv: 1808.10567v4.

[77] The LHCb Collaboration. “The LHCb Physics Programme”. In: (2001).

[78] The BaBar Collaboration. “The BABAR physics book: Physics at an asymmetric B factory”. In: (1998). DOI: https://doi.org/10.2172/979931.

[79] The NA62 Collaboration. “The Beam and detector of the NA62 experiment at CERN”. In: (2017). arXiv: 1703.08501v2.

[80] Peter Cox, Matthew J. Dolan, and Joshua Wood. “New Limits on Light Dark Matter-Nucleon Scattering”. In: (2024). arXiv: 2408.12144v1.

[81] The NA62 Collaboration. “Measurement of the very rare $K^+ \to \pi^+\bar{\nu}\nu$ decay”. In: (2021). arXiv: 2103.15389v2.

[82] The IceCube collaboration. “The IceCube Neutrino Observatory: Instrumentation and Online Systems”. In: *JINST 12 P03012* (2024). arXiv: 1612.05093v3.

[83] The KM3NeT Collaboration. “Letter of Intent for KM3NeT 2.0”. In: *Journal of Physics G: Nuclear and Particle Physics, 43 (8), 084001* (2016). arXiv: 1601.07459v2.

[84] Avrorin A.D., Avrorin A.V., and Aynutdinov V.M. et al. “Status and recent results of the BAIKAL-GVD project”. In: *Phys. Part. Nuclei 46, 211–221* (2015). DOI: https://doi.org/10.1134/S1063779615020033.

[85] The IceCube Collaboration. "Search for neutrino lines from dark matter annihilation and decay with IceCube". In: (2023). arXiv: 2303.13663v1.

[86] The KM3NeT Collaboration. "First Searches for Dark Matter with the KM3NeT Neutrino Telescopes". In: (2025). arXiv: 2411.10092v2.

[87] S. V. Demidov and O. V. Suvorova. "Indirect searches for dark matter at Baksan and Baikal". In: *Phys. Part. Nuclei 46, 222–229* (2015). DOI: https://doi.org/10.1134/S1063779615020070.

[88] Frederick Reines and Clyde L. Cowan. "The Neutrino". In: *Nature 178 (1956) 446-449* (1956).

[89] J.A. Formaggio and G.P. Zeller. "From eV to EeV: Neutrino Cross Sections Across Energy Scales". In: *Rev. Mod. Phys. 84, 1307* (2013). arXiv: 1305.7513v1.

[90] Carlo Giunti and Chung W. Kim. *Fundamentals of Neutrino Physics and Astrophysics*. Oxford University Press, 2007. DOI: https://doi.org/10.1093/acprof:oso/9780198508717.001.0001.

[91] "Scientific Background on the Nobel Prize in Physics 2015: Neutrino oscillations". In: *The Universe* 3.4 (2015), pp. 38–50.

[92] The KATRIN Collaboration. "Direct neutrino-mass measurement based on 259 days of KATRIN data". In: (2024). arXiv: 2406.13516.

[93] Helen Shao, Jahmour J. Givans, and Jo Dunkley et al. "Cosmological limits on the neutrino mass sum for beyond-CDM models". In: (2024). arXiv: 2409.02295v1.

[94] M. Sajjad Athar, A. Fatima, and S. K. Singh. "Neutrinos and their interactions with matter". In: (2022). arXiv: 2206.13792v3.

[95] J.L. Hewett, H. Weerts, and R. Brock et al. "Fundamental Physics at the Intensity Frontier". In: (2012). arXiv: 1205.2671v1.

[96] Maurizio Spurio. *Probes of Multimessenger Astrophysics*. Springer, 2018.

[97] Ethan Silver and Elena Orlando. "Testing Cosmic-Ray Propagation Scenarios with AMS-02 and Voyager Data". In: *ApJ 963 111* (2024). arXiv: 2401.06242v2.

[98] Jacco Vink. "What sources are the dominant Galactic cosmic-ray accelerators?" In: (2022). arXiv: 2212.10677v2.

[99] The Particle Data Group Collaboration. "Review of Particle Physics". In: *Phys. Rev. D 110, 030001* (2024). DOI: https://doi.org/10.1103/PhysRevD.110.030001.

[100] David Freiherr Heereman von Zuydtwyck. "HitSpooling: An Improvement for the Supernova Neutrino Detection System in IceCube". PhD thesis. Université Libre de Bruxelles, 2015.

[101] Pavel Alekseevič Čerenkov. "Visible Radiation Produced by Electrons Moving in a Medium with Velocities Exceeding that of Light". In: *Phys. Rev. 52, 378* (1937). DOI: https://doi.org/10.1103/PhysRev.52.378.

[102] John David Jackson. *Classical Electrodynamics*. John Wiley Sons, 1999.

[103] De Wasseige Gwenhaël. “Solar Flare Neutrinos in the Multi-Messenger Era: Flux, Calculations and a Search with the IceCube Neutrino observatory”. PhD thesis. Vrije Universiteit Brussel, 2018.

[104] Xianliang Wang, Lintao Li, and Jie Li et al. “Cherenkov Luminescence in Tumor Diagnosis and Treatment: A Review”. In: (2022). DOI: https://doi.org/10.3390/photonics9060390.

[105] Igor E. Tamm. *Radiation Emitted by Uniformly Moving Electrons*. Springer, 1991.

[106] A. Gallo Rosso et al. “Introduction to neutrino astronomy”. In: *Eur.Phys.J.Plus 133 (2018) no.7, 267* (2018). arXiv: 1806.06339v2.

[107] The IceCube Collaboration. “IceCube Preliminary Design Document”. In: (2001).

[108] A. Alberta, S. Alves, and M. Andre et al. “The ANTARES detector: two decades of neutrino searches in the Mediterranean Sea”. In: (2025). arXiv: 2504.09473v2.

[109] Marek Kowalski and for the IceCube Collaboration. “Neutrino astronomy with IceCube and beyond”. In: (2017). arXiv: 1705.00383v1.

[110] Sebastian Euler. “Observation of oscillations of atmospheric neutrinos with the IceCube Neutrino Observatory”. PhD thesis. Rheinisch-Westfälische Technische Hochschule Aachen, 2014.

[111] The Super-Kamiokande Collaboration. “Search for Cosmic-ray Boosted Sub-GeV Dark Matter using Recoil Protons at Super-Kamiokande”. In: *Phys. Rev. Lett. 130 (2023) 031802* (2023). arXiv: 2209.14968v4.

[112] Tyce DeYoung for the IceCube Collaboration. “Results from Seven Years of AMANDA-II”. In: *J.Phys.Conf.Ser.136:022046* (2008). arXiv: 0810.4513v1.

[113] The IceCube Collaboration. “Measurement of the cosmic ray energy spectrum with IceTop-73”. In: *Phys.Rev.D88: 042004* (2013). arXiv: 1307.3795v1.

[114] The IceCube Collaboration. “Evidence for High-Energy Extraterrestrial Neutrinos at the IceCube Detector”. In: *Science 342, 1242856* (2013). arXiv: 1311.5238v2.

[115] The IceCube Collaboration. “Measurement of atmospheric neutrino oscillation parameters using convolutional neural networks with 9.3 years of data in IceCube DeepCore”. In: (2024). arXiv: 2405.02163v1.

[116] Jan Kunnen. “A Search for Dark Matter in the Center of the Earth with the IceCube Neutrino Detector”. PhD thesis. Vrije Universiteit Brussel, 2015.

[117] Jakob van Santen. “Simulating penetrating atmospheric leptons in IceCube”. In: (2018). https://indico.kit.edu/event/426/contributions/4334/attachments/2083/2881/CORSIKA_for_IceCube.pdf.

[118] Michael James Larson. “Simulation and identification of non-poissonian noise triggers in the IceCube neutrino detector”. MA thesis. The University of Alabama, 2013.

[119] The IceCube collaboration. “Search for GeV Neutrino Emission During Intense Gamma-Ray Solar Flares with the IceCube Neutrino Observatory”. In: *Phys. Rev. D 103, 102001* (2021). arXiv: 2101.00610v2.

[120] The IceCube Collaboration. “IceCube Sensitivity for Low-Energy Neutrinos from Nearby Supernovae”. In: (2011). arXiv: 1108.0171v2.

[121] Michael James Larson. “A Search for Tau Neutrino Appearance with IceCube-DeepCore”. PhD thesis. University of Copenhagen, 2018.

[122] The IceCube Collaboration. “Search for sub-TeV Neutrino Emission from Novae with IceCube-DeepCore”. In: *ApJ 953 160* (2023). arXiv: 2212.06810v4.

[123] Mia-Louise Nielsen. “Transient Neutrino Astrophysics with IceCube-DeepCore”. MA thesis. University of Copenhagen, 2019.

[124] Eugenio Del Nobile, Marco Cirelli, and Paolo Panci. “Tools for model-independent bounds in direct dark matter searches”. In: *JCAP 1310:019* (2013). arXiv: 1307.5955v5.

[125] JiJi Fan, Matthew Reece, and Lian-Tao Wang. “Non-relativistic effective theory of dark matter direct detection”. In: *JCAP 1011:042* (2010). arXiv: 1008.1591v2.

[126] The IceCube collaboration. “Limits on Neutrino Emission from GRB 221009A from MeV to PeV using the IceCube Neutrino Observatory”. In: *ApJL 946 L26* (2024). arXiv: 2302.05459v3.

[127] Timon Emken and Chris Kouvaris. “How blind are underground and surface detectors to strongly interacting dark matter?” In: *CP3-Origins-2018-007 DNRF90* (2018). arXiv: 1802.04764v2.

[128] Glen Cowan. *Statistical Data Analysis*. Oxford University press, 1998.

[129] Michael E. Peskin and Daniel V. Schroeder. *An Introduction to quantum field theory*. Westview Press, 1995.

[130] W. Carroll and Dale A. Ostlie. *An Introduction to Modern Astrophysics (2nd ed.)* Cambridge University Press, 2017.